Disc actuators for turbulent drag reduction

Daniel J. Wise

A Thesis submitted for the degree of Doctor of Philosophy

Department of Mechanical Engineering

University of Sheffield

June 2015

CONTENTS

LIST OF FIGURES

NOMENCLATURE

$\mathcal{C}$ The coverage $\mathcal{C}$ is defined as the percentage of the channel wall which is in motion.

δ Penetration depth of disc boundary layer, refer to §3.3.6 for details. [m]

δ_e Ekman layer thickness, used to scale the wall-normal coordinate of the oscillating disc boundary layer in the limit $\gamma \gg 1$. [m]

δ_s Stokes layer thickness, this is the thickness of the oscillating-wall boundary layer. Refer to §3.3.6 for further details. [m]

$\mathcal{E}$ Drag reduction per unit actuated area, given by $\mathcal{E}=\mathcal{R}/\mathcal{C}$.

η Wall-normal coordinate of the laminar disc boundary layer (defined in §3.2).

γ Ratio between the oscillation period and the period of rotation of the disc at constant maximum disc-tip velocity.

κ Fluid friction constant, used within equation (5.3).

λ_x Wavelength of wall-forcing. This is a controlling parameter in the imposition of both the streamwise-varying wall-normal transpiration of Quadrio *et al.* (2007) and the spanwise standing-wave forcing of Viotti *et al.* (2009). [m]

$\mathcal{F}_f$ Friction torque coming from the fluid contained within the housing of the freely-rotating discs. This is approximated by the laminar von Kármán

solution. [Nm]

$\mathcal{F}_m$ Torque coming from mechanical friction of the bearing used to mount the freely-rotating discs. This frictional torque is estimated as a proportion of the total torque acting on the discs. [Nm]

$\mathcal{L}$ Characteristic lengthscale of flow control technique. [m]

$\mathcal{N}_x$ Total number of modes simulated along streamwise direction.

$\mathcal{N}_z$ Total number of modes simulated along spanwise direction.

$\mathcal{T}$ Characteristic timescale of flow control technique. [m]

$\mathcal{T}$ Total torque acting on the freely-rotating discs. This is comprised of the turbulent fluid torque, and the mechanical and fluid friction torques. [Nm]

$\mathcal{T}_t$ Turbulent torque acting on the freely-rotating discs. This is the integral of the azimuthal shear stress over the disc surface. [Nm]

$\mathcal{W}_l$ Localized laminar power spent.[W]

$\mathcal{W}_t$ Localized turbulent power spent. [W]

μ Dynamic viscosity of the fluid. [$\mathrm{kgm^{-1}s^{-1}}$]

ν Kinematic viscosity of the fluid. [$\mathrm{m^2s^{-1}}$]

Ω Disc angular velocity [$\mathrm{s^{-1}}$]

Π Streamwise pressure gradient.

$\mathcal{P}_{net}$ Net power saved. This is the difference between the power saved due to the disc forcing and the power spent, i.e. $\mathcal{P}_{net}$=$\mathcal{R}$-$\mathcal{P}_{sp,t}$. [W]

$\mathcal{P}_{sp,t}$ Power spent to enforce the discs motion, defined in §2.3.2. [W]

$\mathcal{P}_x$ Power spent to drive the fluid in the streamwise direction, defined in §2.3.2. [W]

$\mathcal{R}$ Drag reduction, defined as the percentage change of the skin-friction coefficient with respect to the stationary wall value.

$\mathcal{R}_d$ Contribution to drag reduction from attenuation of the turbulent Reynolds stresses.

$\mathcal{R}_t$ Contribution to drag reduction from additional time-averaged disc Reynolds stresses.

ρ Density of the fluid. [kgm^{-3}]

R_p Poiseuille Reynolds number, defined as $R_p{=}U_p^* h^*/\nu^*$.

$\mathcal{S}_x$ Normalized spacing between discs in the streamwise direction.

$\mathcal{S}_z$ Normalized spacing between discs in the spanwise direction.

τ Window time of disc oscillation. This is used in the ensemble average of the oscillating disc flow. [s]

τ_θ Component of wall-shear stress acting in the azimuthal direction. [Nm^{-2}]

τ_t Total shear stress, this is the sum of the viscous stresses arising from the mean flow and the Reynolds stresses. [Nm^{-2}]

τ_w Wall-shear stress. [Nm^{-2}]

θ Azimuthal coordinate.

A Maximum transpiration amplitude. This and λ_x are the free parameters for the imposition of steady streamwise-varying wall-normal transpiration.

a Ratio beween internal and external radii of annular actuators.

b Spanwise dimension of channel geometry. [m]

c Width of annular region surrounding each disc. [m]

C_θ Scaling factor of drag reduction due to angle of wall motion. This is used within §4.3 to predict the drag reduction engendered by the discs.

C_f Skin-friction coefficient, defined as $C_f{=}2\tau_w^*/\left(\rho^* U_b^{*2}\right)$.

C_w Scaling factor of drag reduction due to waveform. This is used within §4.3 to predict the drag reduction engendered by the discs.

D Disc diameter. [m]

D_0 Total diameter of disc and annular gap. [m]

E_p Strong scaling efficiency of the parallel code on p processing elements.

F Axial disc boundary-layer velocity component, used in the laminar solution to the oscillating disc flow.

F' Radial disc boundary-layer velocity component, used in the laminar solution to the oscillating disc flow.

G Azimuthal disc boundary-layer velocity component, used in the laminar solution to the oscillating disc flow.

G_e Enveloping function of disc boundary layer, refer to §3.3.6 for details.

h Channel half-height. [m]

I Moment of inertia of the freely-rotating discs, given by $I^*{=}m^* D^{*2}/8$. [kgm^2]

k Proportion of modes being forced in the homogeneous directions.

l Streamwise dimension of channel geometry. [m]

L_s Slip length for superhydrophobic surfaces, defined within §5.4. [m]

L_x Dimension of the channel in streamwise direction. [m]

L_y Dimension of the channel in wall-normal direction. [m]

L_z Dimension of the channel in spanwise direction. [m]

N Number of oscillation periods of the disc motion.

N_w Womersley number, used to determine the flow profile within the annular disc housing.

N_x Number of discs within computational domain in streamwise direction.

N_y Number of grid points in the wall-normal direction.

N_z Number of discs within computational domain in spanwise direction.

R General Reynolds number. This is defined as $R{=}U^*L^*/\nu^*$ where $L*$ and U^* are characteristic length and velocity scales of the flow.

r Radial coordinate. [m]

r_1 Radius of disc. [m]

r_2 Radius of disc and housing. [m]

R_τ Friction Reynolds number, defined as $R_\tau{=}u_\tau^* h^*/\nu^*$.

R_e Eddy Reynolds number, this is the Reynolds number based on the eddy length and velocity scales.

S_p Speed-up of the parallel code on p processing elements.

T Disc oscillation period. [s]

t Temporal coordinate. [s]

u_τ Friction velocity, defined as $u_\tau^*=\sqrt{\tau_w^*/\rho^*}$. [ms^{-1}]

u_θ Tangential velocity. [ms^{-1}]

U_b Bulk velocity, defined as $U_b=\int_0^1 u_m(y)\mathrm{d}y$. [ms^{-1}]

U_p Centreline velocity of laminar Poiseuille flow. [ms^{-1}]

u_r Radial velocity. [ms^{-1}]

u_s Effective wall-velocity for superhydrophobic surfaces, defined within §5.4. [ms^{-1}]

u_y Velocity component in the axial direction. [ms^{-1}]

W Disc tip velocity. [ms^{-1}]

W_e Envelope of the Stokes layer velocity profile, for further details refer to §3.3.6.

W_{th} Threshold wall-velocity below which Stokes-layer oscillations have little effect on the outer flow, refer to §3.3.6 for details. [ms^{-1}].

x Streamwise spatial coordinate. [m]

x_d Displacement between disc centres in the streamwise direction. [m]

y Wall-normal spatial coordinate. [m]

y_d Penetration depth of Stokes layer, refer to §3.3.6 for details. [m]

z Spanwise spatial coordinate. [m]

z_d Displacement between disc centres in the spanwise direction. [m]

$\mathbf{u}$ Velocity vector. [ms^{-1}]

$\mathbf{u}_d$ Disc flow within channel. [ms^{-1}]

$\mathbf{u}_m$ Mean flow within channel. [ms^{-1}]

$\mathbf{u}_t$ Turbulent flow within channel. [ms^{-1}]

$\mathbf{x}$ Position vector. [m]

LIST OF MY PUBLICATIONS

Wise, D. J., Alvarenga, C. & Ricco, P. 2014 Spinning out of control: Wall turbulence over rotating discs. *Physics of Fluids (1994-present)* **26** (12), 125107.

Wise, D. J. & Ricco, P. 2014 Turbulent drag reduction through oscillating discs. *J. Fluid Mech.* **746**, 536.

ACKNOWLEDGEMENTS

First and foremost I wish to thank my supervisor Dr. Pierre Ricco, it has been an honour to have been his first PhD student. Pierre has patiently guided me along this difficult path, and his joy and enthusiasm for fluid mechanics has helped motivate me even during the most arduous periods. I thank him for this, and for the excellent example he has provided for how to perform research. My thanks also go to Miss Claudia Alvarenga for her helpful discussions on the discs, and to Miss Elena Marensi for her insightful comments on a preliminary manuscript.

I have presented a part of this thesis at the 66th Annual Meeting of the APS Division of Fluid Dynamics, Pittsburgh, Pennsylvania, in November 2013. This experience was financially supported by the APS Division of Fluid Dynamics Travel Subsidy Grant, and I thank the society for its help. A further part has been presented at the European Drag Reduction and Flow Control Meeting, Cambridge, UK, in March 2015. I am grateful for the support from the Computational Physics Group of the Institute of Physics who made my attendance possible.

I am deeply indebted to my mother and father for their unwaivering support, and to my sister for her encouragement. This dream would have remained unfulfilled were it not for their patience. E finalmente, grazie e un bacio per la mia amore Elena, la cui presenza mi fa felice anche nei momenti più duri.

ABSTRACT

The change in a turbulent channel flow subjected to the motion of flush-mounted disc actuators has been studied by means of direct numerical simulations. The Reynolds number is R_τ=180, based on the friction velocity of the stationary-wall case and the half-channel height. Variations to the original disc actuators of Ricco & Hahn (2013) are investigated, with the aim of improving their performance. This includes oscillating discs, annular and half-disc actuators, and freely-rotating discs. A maximum drag reduction of 26% arises from the half-disc actuators, while the maximum net power saving of 6% results from the oscillating discs.

Through use of the Fukagata-Iwamoto-Kasagi identity it has been possible to show that the wall-friction reduction due to the disc actuators is due to two distinguished effects. One effect is linked to the direct shearing action of the near-wall oscillating-disc boundary layer on the wall turbulence, which causes the attenuation of the turbulent Reynolds stresses. The other effect is due to the additional disc-flow Reynolds stresses produced by the streamwise-elongated structures which form between discs and modulate slowly in time. The drag reduction due to turbulent Reynolds stress attenuation depends on the penetration thickness of the disc-flow boundary layer, while the contribution to drag reduction from the elongated structures scales linearly with a simple function of the maximum tip velocity and oscillation period.

Through investigation of different wall arrangements of disc actuators it is found that the layout ot the discs has a complex and unexpected effect on the flow. For low disc-tip velocities, the drag reduction scales linearly with the percentage

of the actuated area, whereas for higher disc-tip velocity the drag reduction can be larger than the prediction found through the linear scaling with actuated area. This increased drag reduction is caused by the viscous boundary layer which develops over the portions of stationary wall due to the radial flow produced by the discs. For the highest disc-tip velocity the drag reduction even increases by halving the number of discs, causing a gain in the performance of the actuators whilst reducing the complexity of their implementation.

1. INTRODUCTION

1.1 Turbulence

Incompressible flow is governed by the Navier-Stokes and continuity equations, written as

$$\frac{D\mathbf{u}^*}{Dt^*} = -\frac{1}{\rho^*}\nabla^* p^* + \nu^* \nabla^{*2}\mathbf{u}^*, \text{ and} \tag{1.1}$$

$$\nabla^* \cdot \mathbf{u}^* = 0, \tag{1.2}$$

respectively. Here and throughout $\mathbf{u}^*$ and p^* are the velocity and pressure fields; ρ^* and ν^* are the density and kinematic viscosity of the fluid; t^* is the temporal coordinate; ∇^*, ∇^{*2} and $\nabla^{*}\cdot$ are the gradient, Laplacian and divergence operators in Cartesian coordinates; and the $*$ superscript denotes a dimensional quantity. The term on the left of equation (1.1) is the convective or material derivative of the fluid particle, it represents the time rate of change of the velocity of a fluid particle as it moves along its trajectory. The terms to the right of equation (1.1) are the pressure gradient and viscous forces, respectively.

By taking characteristic length and velocity scales of a particular flow, termed L^* and U^* respectively, the variables can be made dimensionless as follows:

$$\mathbf{u} = \frac{\mathbf{u}^*}{U^*}, \quad t = \frac{t^* U^*}{L^*}, \quad \mathbf{x} = \frac{\mathbf{x}^*}{L^*}, \text{ and } p = \frac{p^*}{\rho^* U^{*2}}.$$

Equations (1.1) and (1.2) thus become

$$\frac{D\mathbf{u}}{Dt} = -\nabla p + \frac{1}{R}\nabla^2 \mathbf{u}, \text{ and} \tag{1.3}$$

$$\nabla \cdot \mathbf{u} = 0, \tag{1.4}$$

where $R{=}U^*L^*/\nu^*$ is a dimensionless parameter. The benefits of scaling the equations in this way may not be immediately apparent, however the implications are huge. The concept of dynamic similarity allows an infinite number of flows of the same geometry to be compared, so long as the value of R is constant. Although the parameters U^*, L^* and ν^* may be different for two different scenarios, as long as the ratio U^*L^*/ν^* is constant then so is the ratio between the viscous and inertial forces. The parameter R was first determined by Stokes (1851), yet the later experiments of Reynolds (1883) led to it being henceforth termed the Reynolds number.

Reynolds varied R through changes in the geometrical and fluid properties of a pipe flow, observing the effects on the characteristics of a dye path introduced at the centreline. Reynolds observed three distinct behaviours of the flow (Reynolds, 1883). For values of R below a lower critical value, *"the elements of the fluid follow one another along lines of motion which lead in the most direct manner to their destination"*. For larger R, above an upper critical value, the elements of the fluid *"eddy about in sinuous paths the most indirect possible"* (Reynolds, 1883). It was also noted that between these two critical values of R there is a regime in which the fluid motion can resemble either one of the two behaviours. Reynolds (1883) noted that this was due to the level of background disturbance within the experiments. Although in this seminal paper the word turbulence was never used, Reynolds was documenting the transition from laminar to turbulent flow.

The study of turbulence has its beginnings with Leonardo da Vinci in the 15th century who described the motion of swirling water behind an obstacle as *turbolenza* (Favaro, 1918). Within his sketch of the phenomenon - shown in figure 1.1 - he managed to capture what he observed to be two distinct motions within the fluid, one *"due to the principle current, the other to the random and reverse*

motion". This behaviour was later captured mathematically by Reynolds (1895), who proposed a time-averaging procedure to decompose the flow into its mean and fluctuating components. Such treatment is now termed *Reynolds decomposition*. Using Reynolds decomposition the instantaneous velocity field u is separated into its mean and fluctuating parts as $u=\overline{u}+u'$, where $\overline{u}$ is the time-averaged mean flow and u' is the turbulent fluctuating component (Reynolds, 1895).

Fluid flow is in fact naturally turbulent, occurring across a wide range of scales throughout the universe. From the air flow through the human respiratory system to the convection which creates magnetic fields in planetary bodies, turbulence is ubiquitous and its understanding is one of the most important challenges in physics. An often quoted definition for turbulence is that of G. I. Taylor, first attributed to him by von Kármán (1937), which reads:

> *an irregular motion which in general makes its appearance in fluids, gaseous or liquid, when they flow past solid surfaces.*

The significant feature here is the word 'irregular'; it stipulates that there cannot exist a function through which the turbulent motions can be described at each temporal and spatial location. There are of course further criteria a flow must satisfy to be considered turbulent, however Taylor's definition is a useful starting point.

The concept of an energy cascade in turbulence was first put forward by Richardson (1921). His proposition was that a turbulent flow could be considered to be comprised of motions occuring at different typical length and timescales. The term 'eddy' was used to describe these motions, and although the word lacks a precise definition it can be thought to mean a swirling movement occuring within a coherent volume in the flow. It was Richardson's belief that the largest eddies - usually determined by the largest dimension of the flow - contain most of the energy, and that through their destruction energy is transferred to smaller eddies.

Fig. 1.1: Leonardo da Vinci's portrayal of the swirling motions due to turbulence.

This process then repeats itself, causing the creation of smaller and smaller scales of motion. The lower bound of scales for this cascade is determined by the Reynolds number of the flow. By defining an eddy Reynolds number R_e based on the eddy velocity and lengthscales, it can be shown that the smallest scales of the flow exist when $R_e{=}\mathcal{O}(1)$. At this point viscosity is no longer negligible when compared to the inertial forces. The viscous forces then act to dissipate the energy from the smallest scales of motion into heat.

The simulations presented within the current work take place in the canonical channel geometry, therefore a brief desription of this flow is provided. Flow through a rectangular duct of length l^*, width b^* and height h^* is considered, as shown in figure 2.1. The channel has both length and width much larger than its height, i.e. $l^*/h^*{\gg}1$, $b^*/h^*{\gg}1$; therefore the wall-effects from the sides of the channel are not considered and the flow is statistically one-dimensional. The fluid has a mean velocity component only in the streamwise (x^*) direction. The velocity components u^*, v^*, and w^* refer to the flow in the streamwise (x^*), wall-normal (y^*) and spanwise (z^*) directions, respectively. The flow is characterized by the Reynolds number $R_p{=}U_p^*h^*/\nu^*$, where U_p^* is the mean velocity at the channel centreline (i.e. at $y^*{=}h^*$).

Given the assumptions in the previous paragraph and averaging the channel

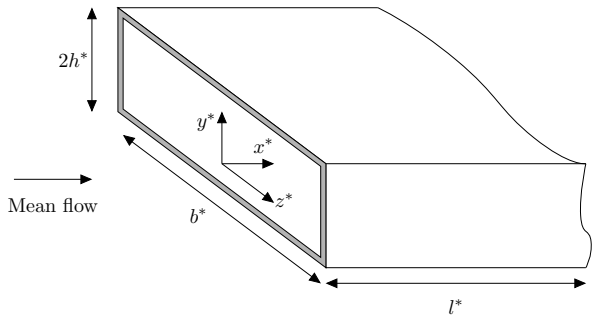

Fig. 1.2: Schematic of the canonical channel flow geometry, as defined by Pope (2000).

flow in time, the streamwise Navier-Stokes equation reduces to

$$\frac{\partial \overline{p}}{\partial x} = \frac{\partial}{\partial y}\left(\frac{1}{R_p}\frac{\partial \overline{u}}{\partial y} - \overline{u'v'}\right). \tag{1.5}$$

The term within the parentheses in equation (1.5) is the total shear stress τ_t. The total shear stress is thus the sum of the viscous stresses term arising from the mean flow, and the turbulent contribution $\overline{u'v'}$ known as the Reynolds stresses. For channel flows the Reynolds stresses are negative, and as shown by (1.5) they therefore contribute positively to the total shear stress. By reducing the magnitude of the Reynolds stresses a reduction in the total shear stress can thus be achieved.

In wall-bounded turbulent flows it is known that there are certain coherent patterns within the flow that often appear at unpredictable positions and times. Although these patterns differ in their finer detail, the recognition and understanding of the most common of these coherent patterns is the subject of intense research. A review of this subject can be found in Robinson (1991), and a summary of the structures found in his numerical simulations of wall-bounded turbulence is shown in figure 1.3. Such repeating patterns in the flow are termed *c*oherent structures and are loosely defined as spatial or temporal regions within which one or more component of the velocity field exhibits correlation with itself or with another component (Robinson, 1991). Amongst other things the identification of these structures can lead to further understanding into how they may

be detected, modified, or destroyed.

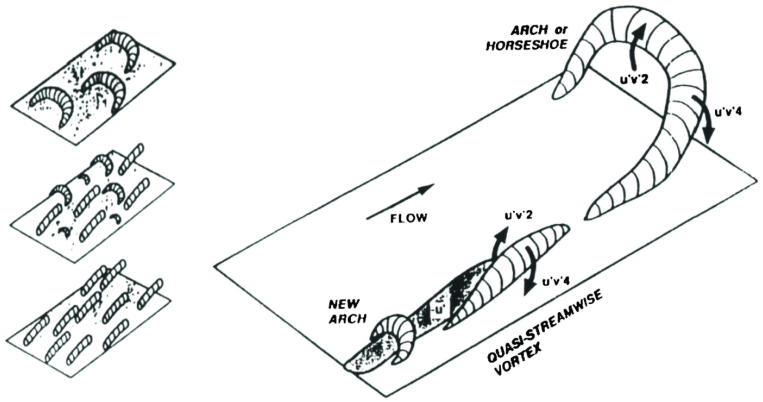

Fig. 1.3: A summary of the structures found by Robinson (1991) in his numerical simulations of wall-bounded turbulence. Left: schematic of vortical structures found in different boundary layer regions. Right: Model of the relationship between the quasi-streamwise vortices found near the wall, and the hairpin vortices found in the outer region.

1.2 Flow control

Flow control is the discipline which focuses on altering the characteristics of a flow field favourably. The beginnings of flow control are found almost 400,000 years ago with the invention of streamlined spears in the lower paleolithic era by primitive man, the evolution of fin-stabilised arrows and boomerangs following soon after. The experiments of Prandtl (1904) marked the end of the empirical development of flow control technology, diverting the subject from trial-and-error towards experimental analysis and logical design. The modern science of flow control can have its aims in delaying, suppressing or enhancing turbulence, with final goals being drag reduction, increased lift or increased mixing.

Drag is the resistance to relative motion of a fluid over a solid. The viscous effects result in a force on the surface of the solid, opposite to the direction

of motion. This force is comprised of the surface integrals of both the shear stress and pressure, labelled the skin-friction and pressure drags, respectively. Skin-friction drag and its reduction will be further expanded on in the following paragraphs. Skin-friction drag is the main contribution to energy loss in industrial applications in which wall-bounded flows occur, and its reduction is of major interest from both economic and ecological perspectives. Focussing firstly on the global airline industry, it has been calculated that the total fuel bill for commercial airlines rose from US$43 billion in 2003 to US$176 billion in 2011, with this trend expected to continue in coming years (Bisignani, 2011). If we estimate that viscous or skin-friction drag accounts for a minimum of 50% of the total drag present during the subsonic operation of a conventional aircraft (Schrauf, 2006), it can be shown that a reduction of only 10% in viscous drag equates to an industry wide saving of approximately US$8.8 billion. Another major beneficiary from the reduction of viscous drag is the oil industry. Kennedy (1993) reports the total pumping costs of 46 major US companies for calendar years 1988 and 1989 to be approximately US$376 million, equivalent to 17% of their total operational expenditure. As the majority of the cost of oil transportation in pipes is associated with overcoming the drag at the wall boundary (Keefe, 1998), any reduction in this drag results in significant savings in the operational costs of the industry.

A schematic of the way in which flow control techniques can be classified is shown in figure 1.4. The first division in methods is between those that are either active or passive. Active methods require an external energy input, while passive methods manipulate the flow field without a supply of energy. Amongst active methods there exists a further division between those techniques which operate under either closed- or open-loop control (Gad-el Hak, 2000). Closed-loop control requires sensors to measure the flow properties, thus allowing the

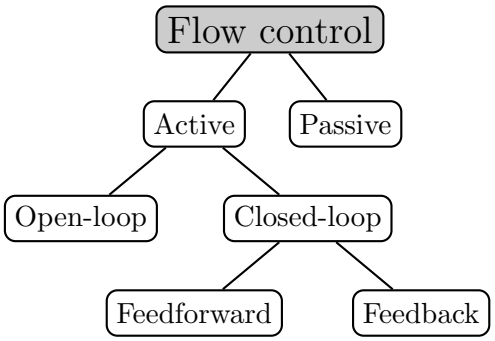

Fig. 1.4: Schematic showing the ways in which flow control techniques are classified.

control input to be adjusted according to a prescribed algorithm. Open-loop control is instead predetermined and does not respond to changes in the flow. As such it does not require sensors. Although numerical investigations of closed-loop flow control utilizing linear control theory have promised high drag reduction and significant net power savings (computed by taking into account the energetic cost of control), the experimental verification of these computational efforts poses enormous challenges. These relate to the very small spatial and temporal scales typically required to achieve such energetic performances. A short review of some of the more prominent control strategies is given in the following paragraphs.

1.2.1 Passive techniques

Shark skin is covered in placoid scales, a characteristic of cartilaginous fishes. These scales, shown in figure 1.5 (left), resemble tooth-like protrusions from the surface and are also referred to as dermal denticles. The scales were found by Bechert *et al.* (1985) to be aligned parallel to the direction of motion of the shark, and to possess constant separation between consecutive peaks (Walsh & Lindemann, 1984). The protrusions are also observed to maintain this spacing as the shark grows, with additional scales being grown. Wall-grooves aligned in the streamwise direction - otherwise known as riblets - attempt to mimic the

effects of dermal denticles. In channel flow experiments with Reynolds number R_b=3400, such grooves produce drag reductions of up to 12% (Sasamori *et al.*, 2014). The initial boundary layer experiments of Walsh (1982) found that riblets possessing a V-shape with a sharp peak and either a sharp or curved valley produced the largest value of drag reduction. Further studies have confirmed that drag reduction increases linearly with the spacing, s, between riblets up to an optimum value, dependent on the cross-sectional shape of the riblets. A region of drag increase is then observed Bechert *et al.* (1997). Due to a marked dependence on their cross-sectional shape, riblet spacing is not a suitable scaling parameter for whether drag reduction will occur. Instead García-Mayoral & Jiménez (2011) proposed another lengthscale determined by the square root of the groove cross-sectional area which accurately predicts an optimal lengthscale independent of the riblet geometry.

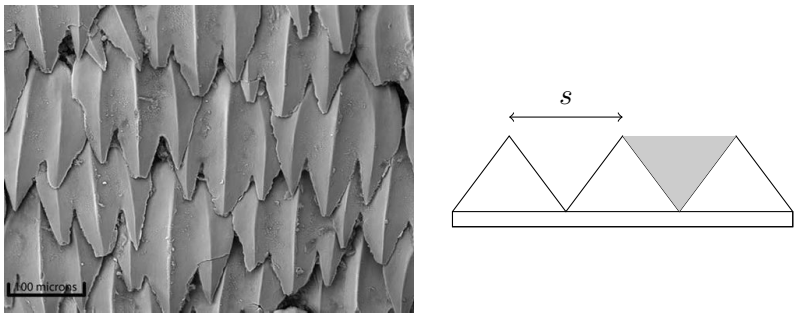

Fig. 1.5: Left: Magnification of shark skin showing the aligned protrusions. Right: Cross section of the triangular riblet geometry showing the spacing, s, between consecutive riblets. The groove cross-sectional area is indicated by the grey shading.

Bechert *et al.* (1986) showed that riblets reduce the spanwise velocity fluctuations in the near wall region, causing a reduction in the turbulent momentum transfer and also in the shear stress (Bechert *et al.*, 1986; Bechert & Bertenwerfer, 1989). This reduction in the spanwise velocity fluctuations was also observed in the direct numerical simulations (DNS) of Choi *et al.* (1993), and more recently

by Goldstein *et al.* (1995). The experimental work of Hooshmand *et al.* (1983) - on the optimum V-groove shape described by Walsh - found that the skin-friction coefficient on the riblet surface was simultaneously increased at the peaks and decreased at the troughs by values of 10% and 40% respectively. This agrees with the more recent findings of Choi *et al.* (1993) that only a certain proportion of the riblets is exposed to the high shear stresses caused by the downward flow motions induced by the streamwise vortices. The drag-increase riblet configurations expose a large part of the wetted surface to the wallward high-speed flow motions, whereas these sweeps only impinge on the riblet tips in the drag reduction cases. Concerning industrial applications, as 50% of the drag experienced by an aircraft is associated with skin-friction then a 6% overall energy saving is possible assuming the maximum experimental values are achieved. Riblets are one of the few flow control techniques to have been flight tested. By covering approximately 70% of the surface of a commercial Airbus A320, an estimated value of 2% drag reduction was achieved based on fuel usage (Szodruch, 1991). This therefore shows a deviation from the experimentally and numerically approximated values of drag reduction. As in general the experimental and numerical campaign into riblet drag reduction is focused on geometrically simple surfaces, a reduction in performance is expected when riblets are applied to more complex surfaces. Additionally surface modifications such as riblets which rely on intricacies at very small scales are susceptible to both wear and the build-up of dirt. Further details of the flight testing of riblets, including discussion on their susceptibility to maintainence and longevity issues is given in Robert (1992).

1.2.2 Active techniques

Although there exist a wide variety of active techniques for skin-friction drag reduction, it is wall-normal transpiration and in-plane wall forcing that will be

reviewed in the following pages.

Wall-normal transpiration

An active closed-loop technique for turbulence control based on the detection and suppression of near-wall turbulent structures was proposed by Choi *et al.* (1994) and investigated through DNS at Poiseuille Reyolds number, R_p=4200. Opposition control is applied in the form of a wall-normal velocity, resembling either suction or blowing. The applied velocity is equal in magnitude and opposite in direction to the detected wall-normal velocity at a predetermined displacement from the wall. Therefore when the wall-normal velocity component at the sensor location is detected to be in the direction of the wall (a sweep), a blowing boundary condition is imposed. Equivalently, when a positive wall-normal velocity is detected at the same location (an ejection), a suction boundary condition is prescribed. Skin-friction reductions of up to 25% have been numerically realized for this technique at an optimal sensory plane located at y^+=10, however either drag increase or lower values of drag reduction occur for other locations. The + superscript here denotes scaling with viscous quantities, i.e. with kinematic viscosity ν^* and friction velocity $u_\tau^*=\sqrt{\tau_w^*/\rho^*}$ where τ_w^* is the wall-shear stress. When the boundary conditions are imposed only for a detected magnitude of the velocity greater than a threshold, drag reduction is still observed (Choi *et al.*, 1994). The latter reaches 10% when the threshold value is equivalent to twice the root-mean-square value of the wall-normal turbulent fluctuations. Despite these promising values of drag reduction it must be noted that for such a technique to be applied efficiently, the entire wetted surface should be capable of actuation. This has an associated weight and complexity penalty which must be considered when comparing various drag reduction and flow control techniques. Additionally, the experimental verification of computationally simple methods poses enormous

challenges. These, in general, are associated with the very small spatial and temporal scales required to achieve the drag reductions observed through simulations. Progress is being made to mimic opposition control techniques such as this with the fabrication of novel MEMS-based flow sensors and actuators (Kasagi *et al.*, 2009). However according to the estimates of Wilkinson (1990) the current production cost of such systems for use on a commercial aircraft would however render their application prohibitively expensive.

A simpler open-loop implementation of wall-normal transpiration by Quadrio *et al.* (2007) consists of the application of steady streamwise-varying transpiration to a turbulent channel flow with R_p=3300. Quadrio *et al.* (2007) imposed boundary conditions of the form $v^+=A^+\cos(2\pi x^+/\lambda_x^+)$ to the channel walls, where A^+ is the maximum transpiration amplitude and λ_x^+ is the streamwise wavelength of the applied forcing. A parametric investigation yielded a maximum of 13% drag reduction for A^+=4.7 and λ_x^+=226.

Further DNS on wall-normal transpiration was conducted by Min *et al.* (2006) who applied travelling-wave transpiration boundary conditions to the walls of a turbulent channel flow at R_p=2000. It was found that for the optimal parameter combination of an upstream travelling wave, sublaminar skin-friction drag was achieved. However Luchini (2008) suggested that the sublaminar drag observed by Min *et al.* (2006) was instead a pumping effect whereby the transpiration was actively pushing the fluid rather than causing any modification to the turbulent dynamics. Luchini (2008) showed that in the absence of a pressure gradient the transpiration caused a net streamwise flow in the channel, thereby validating his argument. Hœpffner & Fukagata (2009) have more formally defined the difference between methods which create pumping or cause drag reduction, based on the creation of a streamwise mean flow in the absence of a pressure gradient.

Despite the extensive use of zero mass flux synthetic jet actuators for separa-

tion control (e.g. Amitay & Glezer, 2006; Zhang & Zhong, 2010), there exists little experimental work on their application to skin-friction drag reduction. Recent studies do however show that when applied to a turbulent boundary layer, the wall-normal oscillatory flow produced by these actuators is capable of reducing the turbulent intensity and creating drag reduction (Spinosa *et al.*, 2015).

Spanwise wall forcing

It was first discovered experimentally by Bradshaw & Pontikos (1985) that the application of a spanwise pressure gradient to an initially two dimensional boundary layer suppresses the near-wall transfer of momentum and turbulent energy, thereby reducing the turbulent wall shear stress. However, soon after it was recognized that a continuous spanwise pressure gradient only results in temporary drag reduction (Driver & Hebbar, 1987; Moin *et al.*, 1990). After an initial three-dimensional transient period a new steady regime is reached. The turbulent quantities then return to an altered two-dimensional state with any drag reduction being lost.

Following this, the DNS of Jung *et al.* (1992) and the experimental campaign by Laadhari *et al.* (1994) showed that sustained drag reduction could be created through the implementation of wall-oscillations of the form $W{=}W_m \sin(2\pi t/T)$, where W_m is the maximum amplitude of the oscillations and T is the period. It was these initial works that promoted a rich vein of work into drag reduction via spanwise wall forcing. Jung *et al.* (1992) showed that at skin-friction Reynolds number $R_\tau{=}200$, the wall oscillations suppress the frequency and intensity of near-wall turbulent bursts, also resulting in sustained wall-friction reductions of approximately 45%.

Baron & Quadrio (1996) computed the actual power savings achieved through the wall oscillations, given by subtracting the power needed to enforce the wall-

motion from the total drag reduction. Although higher oscillation amplitudes result in larger values of drag reduction, a net power saving was shown to only be obtainable for the lower amplitude investigated (approximately equal to a third of the magnitude of the wall oscillations imposed by Jung *et al.* (1992)). Further experimental investigations were performed by Choi & Graham (1998) who imposed circumferential oscillations on a section of pipe flow at R=23,333 and 36,300 (based on the pipe diameter and bulk velocity). Drag reductions of 25% were observed for oscillation periods in the range $50 \leq T^+ \leq 100$. As the later DNS of Quadrio & Sibilla (2000) at R_p=4900 showed that drag reductions of 40% were possible for the pipe flow geometry, it was suggested that the differences in drag reduction were instead due to the increased Reynolds number. Possible power savings of 7% were computed for this pipe-flow study, occurring only for lower wall velocities. In their parametric study, Quadrio & Ricco (2004) found that at R_τ=200 the maximum drag reduction of 45% occurs for the parameter combination W_m^+=27, T^+=100. They discovered the existence of an optimal oscillation period which occurs in the range $100 \leq T^+ \leq 125$ for each forcing amplitude. The drag reduction also increases with W_m^+ approaching an asymptotic value dependent on the oscillation period.

Berger *et al.* (2000) exploited the Lorentz force to create an oscillating-wall profile in the near-wall region of a turbulent channel flow. The flow of the conductive working fluid was forced by a cross-stream large-scale velocity shear induced by a surface-mounted system of electrodes and magnets. In results comparable with those from direct oscillation of the channel walls, drag reductions of approximately 40% were found for R_τ=100. In an analysis of the power budget for this method Berger *et al.* calculated that the power spent to oscillate the flow was $\mathcal{O}(10^3)$ greater than any power savings caused by the suppression of turbuence. Nevertheless, works such as this which propose new actuation strategies to take

advantage of the drag reduction capabilities of the oscillating-wall mechanism can be considered to be major advancements.

It was found by Choi *et al.* (2002) that the space-averaged turbulent spanwise flow created by the oscillating wall agrees closely with the laminar solution to the Stokes second problem for oscillation periods smaller or comparable with the optimum one. This led to the use of a scaling parameter for the drag reduction. Quadrio & Ricco (2004) found a linear relation between this parameter - a measure of the penetration depth and acceleration of the Stokes layer - and the drag reduction. This relation was noted to be valid only for $T^+ \leq 150$. Quadrio & Ricco (2004) were also the first to explain the existence of the optimal period by comparing it with the characteristic Lagrangian survival time of the near-wall turbulent structures.

More recently, Ricco *et al.* (2012) endowed the scaling parameter with a more direct physical meaning, showing it to be proportional to the maximum streamwise vorticity created by the Stokes layer at constant maximum velocity. Ricco *et al.* (2012) considered the turbulent enstrophy equation rather than the transport equation for the turbulent energy dissipation, observing how the oscillating wall affects the individual terms in the equation. They were able to identify the vorticity production term as being the most dominant near the wall. The raise in vorticity production is balanced by an increase in the turbulent dissipation in the same region. By studying the transient evolution from the start-up of the wall motion, Ricco *et al.* (2012) showed that the turbulent kinetic energy and the skin-friction coefficient decrease because of a short-time transient increase of turbulent enstrophy. This is the latest effort aimed at elucidating the drag reduction mechanism, after research works based on the disruption of the near-wall coherent structures (Baron & Quadrio, 1996), the cyclic inclination of the low-speed streaks (Bandyopadhyay, 2006), the weakening of the low-speed streaks (Di Cicca

et al., 2002; Iuso *et al.*, 2003), and simplified models of the turbulence-producing cycle (Dhanak & Si, 1999; Moarref & Jovanovic, 2012; Duque-Daza *et al.*, 2012).

Viotti *et al.* (2009) converted the unsteady oscillating-wall forcing to a steady streamwise-dependent spanwise motion of the wall in the form $W{=}W_m \cos(2\pi x/\lambda_x)$. Via DNS they found an optimal forcing wavelength of approximately $\lambda^+_{opt}{=}1250$, which is related to T_{opt}, the optimum oscillating-wall period, through $\mathcal{U}_w$, the near-wall convection velocity, as $\lambda_{opt}{=}\mathcal{U}_w T_{opt}$. Skote (2013) employed Viotti *et al.*'s forcing to alter a free-stream turbulent boundary layer and found good agreement between the analytic solution to the spatial Stokes layer flow and the time-averaged spanwise flow. Skote (2013) also showed that the damping of the turbulent Reynolds stresses depends on the penetration depth of the spatial Stokes layer.

The oscillating-wall and steady-wave techniques were generalized by Quadrio *et al.* (2009) who considered wall turbulence forced by wall waves of spanwise velocity of the form $W{=}W_m \cos[2\pi(x/\lambda_x - t/T)]$. A maximum drag reduction of 47% and a maximum net energy saving of 26% were computed for $R_\tau{=}200$. For wall waves travelling at a phase speed comparable with the near-wall turbulent convection velocity, drag increase was also found.

Despite the widespread interest in turbulent drag reduction by active wall forcing, the implementation of these techniques in industrial settings appears to be an insurmountable challenge. Progress is nonetheless being made to improve this scenario. Prominent amongst recent efforts is the experimental work by Gouder *et al.* (2013) on in-plane forcing of wall turbulence through a flexible wall made of electroactive polymers. The main reasons which render the technological applications of active techniques an involved engineering task are *i)* the extremely small typical time scale of the wall forcing (the optimal period for the oscillating-wall technique translates to a frequency of 15,000Hz in commercial aircraft flight

conditions), and *ii)* the requirement of large portion of the surface to be in uniform motion. Therefore, drag reduction methods which operate on a large time scale and rely on finite-size wall actuation are preferable in view of future applications.

Surface mounted discs

By applying a control scheme to the three velocity components in the near-wall region, Keefe (1995) achieved drag reduction of 35%. Minimal actuation was required in the wall-normal direction to obtain the drag reduction, leading to experimental work on the same control scheme applied only in the stream- and spanwise directions. Identical drag reduction occured with this restriction, and Keefe put forward a novel actuation strategy exploiting this. In the patent for the strategy Keefe proposed an array of discs mounted flush to the surface of a flat plate, which also houses shear stress sensors to provide feedback (Keefe, 1997). In both Keefe's patent and published work on this device, no control algorithm is provided and no results are shown. Despite the promising outlook on the applicability of this technique and the prediction of the optimal disc diameter and rotation frequency ($80 - 90\mu$m and 72kHz respectively), Keefe did not further investigate his idea and in the following 15 years neither experimental nor numerical studies on this flow appeared.

Ricco & Hahn (2013) (denoted by RH13 hereafter) showed revived interest in this flow and investigated an open-loop variant of Keefe's technique whereby the discs rotate with a pre-determined constant angular velocity. RH13 performed a numerical parametric investigation at R_τ=180 on D, the disc diameter, and W, the disc tip velocity, shown in figure 1.6. This yielded maximum values for drag reduction and net power saved of 23% and 10%, respectively. RH13 also showed that drag increase occurs for small diameter and rotational periods, that the disc-flow boundary layer must be thicker than a threshold to obtain

drag reduction, and that the power spent to activate the discs can be calculated accurately through the von Kármán laminar viscous pump solution (Panton, 1995) under specified conditions. The Fukagata-Iwamoto-Kasagi (FIK) identity (Fukagata *et al.*, 2002), a simple relationship between the skin-friction coefficient and the Reynolds stress distribution, was modified for the disc flow to show that the near-wall streamwise-elongated jets appearing between discs provide a favourable contribution to drag reduction. Promisingly, the optimal spatial and temporal scales were $\mathcal{L}^+=\mathcal{O}(1000)$ and $\mathcal{T}^+=\mathcal{O}(500)$. This is a significant result when these scales are compared with those of other localized actuation strategies, such as the feedback control based on wall transpiration (Yoshino *et al.*, 2008), which are thought to operate optimally at spatio-temporal scales $\mathcal{L}^+=\mathcal{O}(30)$ and $\mathcal{T}^+=\mathcal{O}(100)$. It is the hope that the results of RH13 will therefore offer fertile ground for new avenues of future research on active turbulent drag reduction.

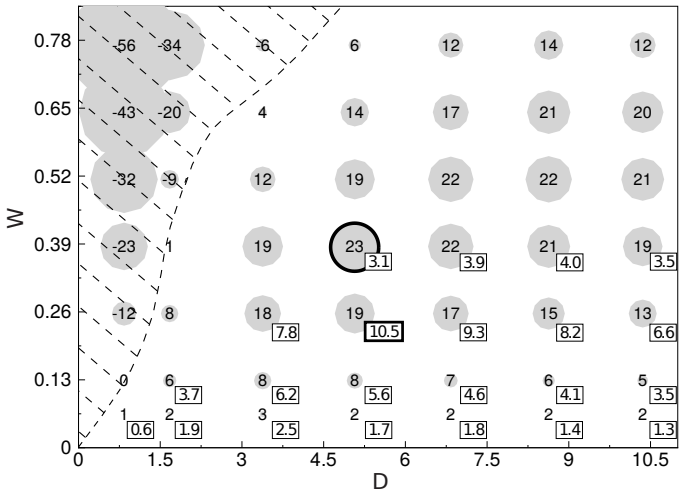

Fig. 1.6: Plot of drag reduction as a function of the disc parameters, as obtained by Ricco & Hahn (2013). The size of the grey circles is proportional to the amount of drag reduction, and the boxed values indicate the net power savings. The shaded region indicates the parameter combinations which resulted in drag increase.

The work of RH13 confirms that the disc actuators can influence the flow

field favourably, resulting in drag reduction. However the mechanism by which this drag reduction occurs is as yet unknown. Although it is evident that the streamwise-elongated structures contribute favourably to drag reduction, the magnitude of this contribution has not been quantified. Further understanding of how the discs engender flow within the channel can lead to improvements in their design, and a possible reduction in the complexity of the actuation strategy. The aims of this project are to make use of direct numerical simulations to *a)* improve on current understanding as to how the disc actuators create drag reduction, *b)* use this understanding to propose modifications to the disc actuators in order to enhance their drag reduction capabilities, and *c)* make the industrial implementation of the disc actuators a more obtainable goal.

2. NUMERICAL PROCEDURES

2.1 Numerical solver, geometry and scaling

A pressure-driven, incompressible, turbulent channel flow at constant mass flow rate is investigated through DNS. The infinite, parallel flat walls of the channel are separated by $L_y^*=2h^*$ where the symbol $*$ denotes a dimensional quantity. A schematic of the geometry is shown in figure 2.1. The streamwise pressure gradient is indicated by Π^*. L_x^* and L_z^* are the dimensions of the computational domain in the streamwise (x^*) and spanwise (z^*) directions. Nodes along y are clustered according to $y(i)=\cos\left[i\pi/(N_y-1)\right]$, where $0\leq i<N_y$, and $N_y=129$ is the number of grid points in the wall-normal direction. The values for Δy_{min} and Δy_{max} are 0.0003 and 0.025, respectively. All simulations are performed at a Poiseuille Reynolds number of $R_p=U_p^*h^*/\nu^*=4200$, where ν^* is the kinematic viscosity of the fluid and U_p^* is the centreline velocity of the laminar Poiseuille flow at the same mass flow rate. The equivalent friction Reynolds number for the uncontrolled stationary-wall case is $R_\tau=u_\tau^*h^*/\nu^*=180$, where $u_\tau^*=\sqrt{\tau_w^*/\rho^*}$ is the friction velocity, τ_w^* is the space- and time-averaged wall-shear stress, and ρ^* is the density of the fluid.

An open-source code called `channelflow` is utilized to solve the Navier-Stokes equations (Gibson, 2006). The code uses Fourier series expansions along the statistically homogeneous x^* and z^* directions, and Chebyshev polynomials along the wall-normal direction y^*. A third-order semi-implicit backward differention scheme is used to advance the equations in time. The time step is changed

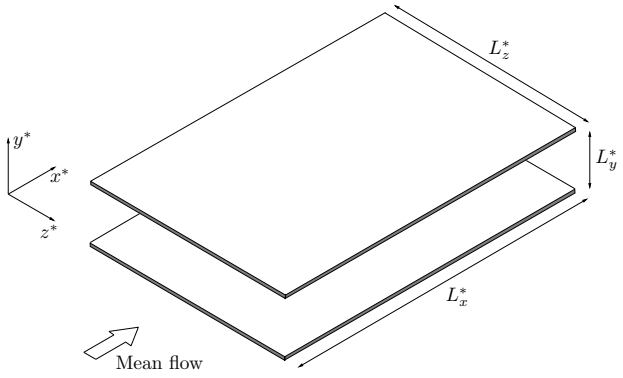

Fig. 2.1: Schematic of the channel geometry.

adaptively between Δt^+_{min}=0.008 and Δt^+_{max}=0.08. This reduces the computational cost by maximizing the CFL number within the range 0.2<CFL<0.4, where CFL=$[|\mathbf{u}'|\,/(\Delta x, \Delta y, \Delta z)_{min}]_{max}\,\Delta t_{prev}$, $\mathbf{u}'$ is the instantaneous velocity field and Δt_{prev} is the previous time step. The nonlinear terms are treated explicitly and the linear terms implicitly. The discretized equations are solved using the Kleiser-Schumann algorithm (Kleiser & Schumann, 1980), outlined in Canuto *et al.* (1988). Dealiasing is carried out by setting the upper third of the modes in the x and z directions to zero. The code has been benchmarked against existing data in literature for fixed (e.g. Kim *et al.*, 1987), and oscillating-wall (e.g. Quadrio & Ricco, 2003) conditions. Details of these checks can be found in RH13. The code has been modified to allow time-dependent disc motion. Validation of the disc boundary conditions has also been done by implementing the discs in other open-source numerical codes, resulting in comparable values of drag reduction and power spent. The code has been parallelized using OpenMP within the scope of this work and simulations have been carried out on the N8 HPC Polaris cluster. Post-processing has been performed on the Iceberg cluster at the University of Sheffield. A detailed description of the code, including results on the parallel scalability is found in Appendix A. Resolution sensitivity checks have been performed, details of which are found in Appendix B.

Lengths are scaled with h^* and velocities are scaled with U_p^*. The time is scaled by h^*/U_p^* and the pressure by $\rho^* U_p^{*2}$. Quantities non-dimensionalized using these outer units are not marked by any symbol. The superscript + will henceforth indicate scaling by viscous units, i.e. with ν^* and u_τ^*. Unless otherwise stated native viscous scaling is used, a terminology first defined by Trujillo *et al.* (1997). This is based on u_τ^* from the case under investigation.

2.2 Flow decomposition

The averaging operators used to decompose the flow are defined in the following. The space- and time-ensemble average is defined as

$$\overline{f}(x,y,z,\tau) = \frac{1}{N_x N_z N} \sum_{n_x=0}^{N_x-1} \sum_{n_z=0}^{N_z-1} \sum_{n_t=0}^{N-1} f(\tilde{x}+2n_x D, y, \tilde{z}+n_z D, n_t T+\tau), \quad (2.1)$$

where $2N_x$ and N_z are the number of discs within the computational domain along $\tilde{x}$ and $\tilde{z}$, respectively. For the oscillating disc case τ is the window time of the disc oscillation, and N is the number of oscillation periods. This average is used to condense the computational domain into the minimal repeating unit, and is used to present phased averaged information on the disc flow.

The time average and the spatial average along the homogeneous directions are defined respectively as

$$\langle f \rangle(x,y,z) = \frac{1}{T}\int_0^T \overline{f}(x,y,z,\tau)\mathrm{d}\tau, \quad \hat{f}(y) = \frac{1}{L_x L_z}\int_0^{L_x}\int_0^{L_z} \langle f \rangle(x,y,z)\mathrm{d}z\mathrm{d}x. \quad (2.2)$$

The time and spatial averages are used to present wall-normal profiles of the disc-flow, and are used in the weighted overage of the Reynolds stresses for input to the Fukagata-Iwamoto-Kasagi identity. A global variable is defined as

$$[f]_g = \int_0^1 \hat{f}(y)\mathrm{d}y.$$

The size of all statistical samples is doubled by averaging over the two halves of the channel, taking into account the existing symmetries. The channel flow field

is expressed by the sum

$$\mathbf{u}(x,y,z,t) = \mathbf{u_m}(y) + \mathbf{u_d}(x,y,z,\tau) + \mathbf{u_t}(x,y,z,t), \tag{2.3}$$

where $\mathbf{u_m}(y) = \{u_m, 0, 0\} = \hat{\mathbf{u}}$ is the mean flow, $\mathbf{u_d}(x,y,z,\tau) = \{u_d, v_d, w_d\} = \overline{\mathbf{u}} - \mathbf{u_m}$ is the disc flow, and $\mathbf{u_t}$ is the fluctuating turbulent component.

2.3 Definition of performance quantities

This section introduces the main quantities used to describe the disc flow, i.e. the turbulent drag reduction, the power spent to activate the discs against the viscous resistance of the fluid, and the net power saved, which is their algebraic sum.

2.3.1 Turbulent drag reduction

The skin-friction coefficient C_f is first defined as $C_f{=}2\tau_w^*/\left(\rho^* U_b^{*2}\right)$, where $U_b^* = [u^*]_g/h^*$ is the bulk velocity. The latter is constant because the simulations are performed under conditions of constant mass flow rate. The drag reduction $\mathcal{R}$ is defined as the percentage change of the skin-friction coefficient with respect to the stationary wall value (Quadrio & Ricco, 2004):

$$\mathcal{R}(\%) = 100\frac{C_{f,s} - C_f}{C_{f,s}}, \tag{2.4}$$

where the subscript s refers to the stationary wall case, and C_f is averaged over the channel walls. Using $\tau_w^*{=}\mu^* u_m^{*\prime}(0)$, where μ^* is dynamic viscosity and the prime denotes differentiation with respect to y, (2.4) becomes $\mathcal{R}(\%) = 100 \cdot \left(1 - u_m'(0)/u_{m,s}'(0)\right)$.

2.3.2 Power spent

As the disc flow is an active drag reduction technique, power is supplied to the system to move the discs against the viscous resistance of the fluid. To calculate

the power spent, we first consider the instantaneous energy equation, given by (1-108) in Hinze (1975) and replicated here as

$$\frac{\partial}{\partial t^*}\frac{u_i^* u_i^*}{2} = -\frac{\partial}{\partial x_j^*}u_j^*\left(\frac{p^*}{\rho^*}+\frac{u_i^* u_i^*}{2}\right)+\nu^*\frac{\partial}{\partial x_j^*}u_i^*\left(\frac{\partial u_i^*}{\partial x_j^*}+\frac{\partial u_j^*}{\partial x_i^*}\right)-\nu^*\left(\frac{\partial u_i^*}{\partial x_j^*}+\frac{\partial u_j^*}{\partial x_i^*}\right)\frac{\partial u_i^*}{\partial x_j^*}, \tag{2.5}$$

where i, j are the indices indicating the spatial coordinates $\tilde{x}$, y, $\tilde{z}$ and the corresponding velocity components (Einstein summation of repeated indices is used). The volume-average of the second term on the right-hand side is the work done by the viscous stresses per unit time,

$$\mathcal{P}_{sp,t}^* = \frac{\nu^*}{L_x^* L_y^* L_z^*}\int_0^{L_x^*}\int_0^{L_y^*}\int_0^{L_z^*}\frac{\partial}{\partial x_i^*}\left[u_j^*\left(\frac{\partial u_i^*}{\partial x_j^*}+\frac{\partial u_j^*}{\partial x_i^*}\right)\right]\mathrm{d}\tilde{z}^*\mathrm{d}y^*\mathrm{d}\tilde{x}^*. \tag{2.6}$$

By substituting (2.3) into (2.6) and by use of (2.1) and (2.2), one finds

$$\mathcal{P}_{sp,t}^* = \frac{\nu^*}{h^*}\left(\widehat{u_d^*\frac{\partial u_d^*}{\partial y^*}}\bigg|_{y^*=0}+\widehat{w_d^*\frac{\partial w_d^*}{\partial y^*}}\bigg|_{y^*=0}\right). \tag{2.7}$$

The power spent (2.7) is to be expressed as a percentage of the power employed to drive the fluid in the streamwise direction, $\mathcal{P}_x^*$. First, by volume-, ensemble- and time-averaging the first term on the right-hand side of (1-108) in Hinze (1975), one obtains

$$\mathcal{P}_x^* = \frac{U_b^*\Pi^*}{\rho^*}, \tag{2.8}$$

By dividing (2.7) by (2.8), the percentage power employed to oscillate the discs with respect to the power spent to drive the fluid along the streamwise direction is then obtained,

$$\mathcal{P}_{sp,t}(\%) = \frac{100R_p}{R_\tau^2 U_b}\left(\widehat{u_d\frac{\partial u_d}{\partial y}}\bigg|_{y=0}+\widehat{w_d\frac{\partial w_d}{\partial y}}\bigg|_{y=0}\right), \tag{2.9}$$

where R_τ is the stationary-wall reference value.

2.3.3 Net power saved

The net power saved, $\mathcal{P}_{net}$, the difference between the power saved due to the disc forcing (which coincides with $\mathcal{R}$ for constant mass flow rate conditions) and

the power spent $\mathcal{P}_{sp,t}$, is defined as

$$\mathcal{P}_{net}(\%) = \mathcal{R}(\%) - \mathcal{P}_{sp,t}(\%). \tag{2.10}$$

3. OSCILLATING DISCS

3.1 Flow definition and modelling of actuators

3.1.1 Numerical parameters

For this investigation the channel walls are covered by flush-mounted rigid discs, shown schematically in figure 3.1. The discs have diameter D and oscillate in time with disc tip velocity

$$\widetilde{W} = W \cos\left(\frac{2\pi t}{T}\right). \tag{3.1}$$

Neighbouring discs in the streamwise direction have opposing sense of rotation, whilst neighbouring discs in the spanwise direction have the same sense of rotation. A parametric study was undertaken on D, W and T, with the parameter range selected in order to focus on the portion of D, W parameter space studied by RH13 which leads to high drag reduction. The region of drag increase found by RH13 was not considered. For disc diameters D=1.78, 3.38, a computational box size of dimensions L_x=6.8π and L_z=2.26π was utilized, where L_x and L_z are the box lengths along the streamwise and spanwise directions, respectively. For D=5.07, L_x=6.8π and L_z=3.4π, and for D=6.76, L_x=9.05π and L_z=2.26π. The dimensions of the computational box are larger than those used in literature for similar values of Reynolds number (i.e. Kim *et al.* (1987) (L_x,L_z)=(4π,2π), Quadrio & Ricco (2003) (L_x,L_z)=(21,4.2)). It should be noted that the streamwise dimension of the box in the current study is significantly larger than that of Kim *et al.* (1987). This is to account for the elongation of

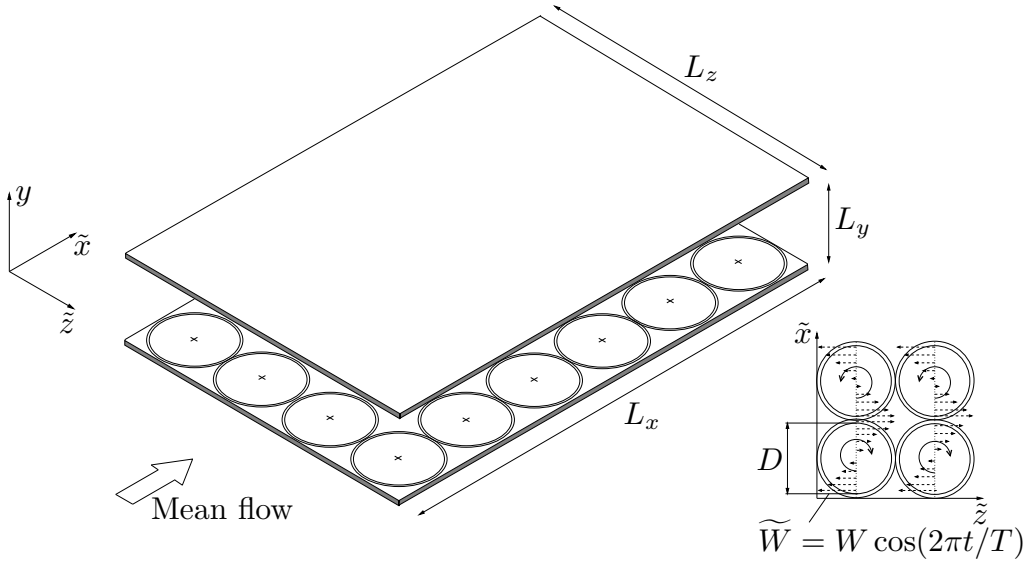

Fig. 3.1: Schematic of the flow domain showing the location and sense of rotation of the discs when $\widetilde{W}$=W.

the near-wall turbulent structures that occurs under drag-reducing conditions (Orlandi & Fatica, 1997). A further check to determine whether L_x and L_z are large enough to incorporate the large-scale structures is to observe whether the two-point correlation coefficient R_{ii}=$\langle u_i(\mathbf{x},t)u_i(\mathbf{x}',t)\rangle$ falls to zero in the streamwise and spanwise directions. Although this check has not been done within the present work, the data of Tsukahara *et al.* (2005) for an uncontrolled channel flow at R_τ=80 suggests that the channel dimensions are sufficiently large. The grid sizes were Δx^+=10, Δz^+=5 in all cases, and the time step was within the range $0.008 \leq \Delta t^+ \leq 0.08$ (scaled in reference viscous units). The initial transient period during which the flow adjusts to the new oscillating-disc regime was discarded following the procedure outlined in Quadrio & Ricco (2004). Flow fields were saved over an integer number of periods at intervals of $T/8$. After the transient was discarded, the total integration time was t^+=6000 for T^+=100, t^+=7500 for T^+=250, 500, and t^+=15000 for T^+=1000.

3.1.2 Disc annular gap

To simulate the disc flow as realistically as possible, a thin annular region of width c was considered around each disc, as shown in figure 3.2. As explained in RH13, there are two reasons for this choice. The clearance flow between each disc and the stationary portion of the wall is simulated to mimic as closely as possible an experimental disc flow set up where such gap would inevitably be present. Secondly, the velocity profile between the disc tip and stationary wall does not present discontinuities. This serves to suppress strongly the Gibbs-type artificial oscillations that would occur if the velocity were not continuous. Ideally, the gap flow would be more realistically simulated by treating the turbulent channel flow and gap flow as coupled systems, but this lies outside the scope of the present study.

As a first approximation, the gap velocity profile is assumed to be symmetric about the disc axis and to change linearly from a maximum velocity at the disc tip to zero at the outer edge of the gap. The tangential velocity u_θ in this region is a function only of r, the radial displacement from the centre of the disc, and time, t. The disc velocity profile is

$$u_\theta(r,t) = \begin{cases} 2Wr\cos(2\pi t/T)/D, & r \le r_1, \\ W(c - r + D/2)\cos(2\pi t/T)/c, & r_1 \le r \le r_2, \end{cases}$$

where $r_1{=}D/2$ and $r_2{=}D/2{+}c$. As a more advanced approximation, the clearance flow is modelled as a thin layer of fluid confined between concentric cylinders. Similarly to the laminar flow between moving flat plates, the flow contained within this annular gap is described by the Womersley number, $N_w{=}c^*\sqrt{2\pi/(\nu^* T^*)}$ (Pozrikidis, 2009). When $N_w{\ll}1$, the linear velocity profile accurately describes the flow. However, for $N_w{=}\mathcal{O}(1)$ the oscillating flow surrounding each disc is confined to a boundary layer which is attached to the oscillating disc and is much thinner than c. The bulk of the annular gap is quasi-stationary. In our

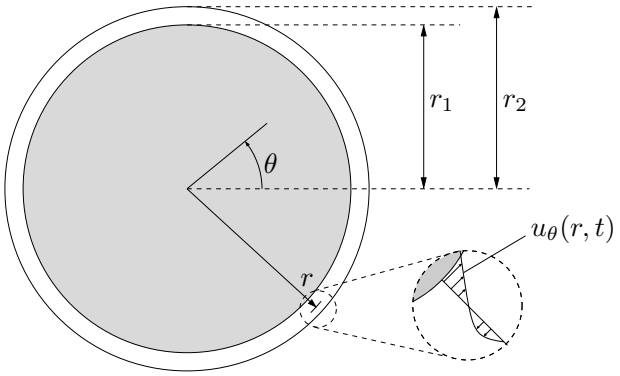

Fig. 3.2: Schematic of disc and annular gap flow.

simulations the minimum N_w=0.51 occurs for the case with the thinnest gap and the largest oscillation period, i.e. for D=1.78, T=130. The maximum N_w=6.42 occurs for D=7.1, T=13. Therefore, it is a sensible choice to simulate the gap via the oscillating layer as N_w attains finite values. Following the analysis of Carmi & Tustaniwskyj (1981), the $u_\theta(r,t)$ velocity profile in the gap is described by the azimuthal momentum equation,

$$\frac{\partial u_\theta}{\partial t} = \frac{1}{R_p}\left(\frac{\partial^2 u_\theta}{\partial r^2} + \frac{1}{r}\frac{\partial u_\theta}{\partial r} - \frac{u_\theta}{r^2}\right). \tag{3.2}$$

Assuming a solution to (3.2) of the form u_θ=$\mathbb{R}\left[\mathring{u}_\theta(r)e^{i2\pi\hat{t}/T}\right]$, where $\mathbb{R}$ denotes the real part and $\hat{t}$ is the rescaled time, $\hat{t}$=t/R_p, the following ordinary differential equation of the Bessel type is obtained

$$\mathring{u}_\theta'' + \frac{\mathring{u}_\theta'}{r} - \left(\frac{2\pi i}{T} + \frac{1}{r^2}\right)\mathring{u}_\theta = 0, \tag{3.3}$$

where the prime denotes differentiation with respect to r. Equation (3.3) is subject to $\mathring{u}_\theta(r_1)$=W, $\mathring{u}_\theta(r_2)$=0. The velocity in the annular gap is

$$u_\theta(r,\hat{t}) = W\cdot\mathbb{R}\left[\frac{\mathcal{K}(\xi r_2)\mathcal{I}(\xi r) - \mathcal{I}(\xi r_2)\mathcal{K}(\xi r)}{\mathcal{I}(\xi r_1)\mathcal{K}(\xi r_2) - \mathcal{I}(\xi r_2)\mathcal{K}(\xi r_1)}e^{i2\pi\hat{t}/T}\right], \tag{3.4}$$

where $\mathcal{I}(\cdot)$ and $\mathcal{K}(\cdot)$ are the first-order modified hyperbolic Bessel functions (Abramowitz & Stegun, 1964) and ξ=$\sqrt{i2\pi/T}$. Velocity profiles are shown in figure 3.3. The Bessel layer was included in the code by reading in a map of

the complex wall velocity at t=0. To advance in time the components within this map were multiplied by $e^{2\pi i\hat{t}/T}$ and the real components were extracted. As the boundary conditions are implemented in spectral space, it was necessary to Fourier transform the time-updated map of the velocity components at each time step, before passing the Fourier components as boundary conditions.

The difference between the values of drag reduction and power spent against the viscous forces computed by use of the two annular-gap models for c=0, 0.02D, and $0.05D$ were within the uncertainty range estimated via numerical resolution checks based on variation of the mesh sizes, time step advancement, and size of the computational box (refer to Appendix B for details). For this reason and because of the higher computational cost caused by the Bessel profile due to the additional spectral transformations, the linear velocity profile model was used. In order to choose the appropriate gap size for the simulations, the dimensional gap values were examined for typical experimental scenarios, presented in table 6 of RH13 for the steady disc flow case. The largest tested gap size of c=$0.05D$ was implemented as it corresponds to a value that would be achievable in the laboratory conditions detailed in this table.

3.2 Laminar flow

For other active turbulent drag reduction techniques the analytical solutions for the corresponding laminar flows induced by wall motion have proven useful for accurately estimating important averaged turbulent quantities, such as the wall spanwise shear (Choi *et al.*, 2002), the power spent for the wall forcing (Ricco & Quadrio, 2008), and the thickness of the generalized Stokes layer generated by the wall waves (Skote, 2011). The laminar solution has also been employed to determine a scaling parameter which relates uniquely to drag reduction under specified wall forcing conditions (Quadrio & Ricco, 2004; Cimarelli *et al.*, 2013).

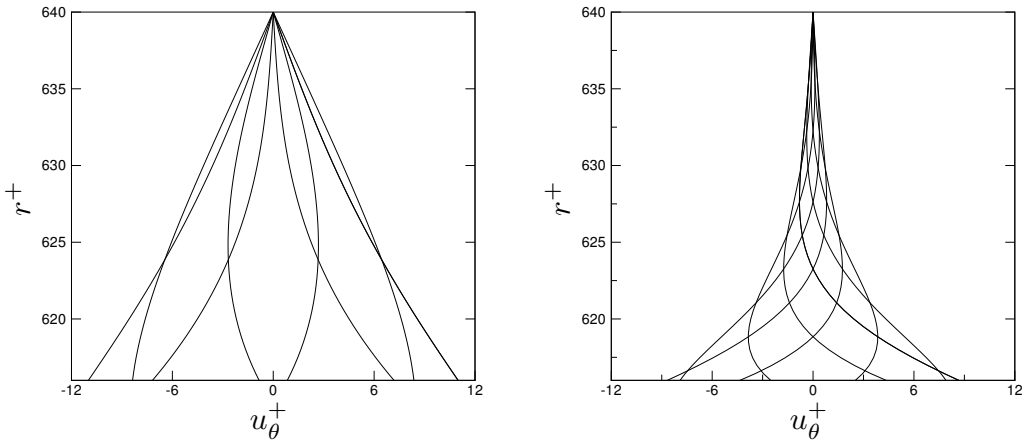

Fig. 3.3: Velocity profiles within the annular gap over a half period of the oscillation, computed through (3.4). Left: D=7.1, W=0.51, T=130, N_w=2.03. Right: D=7.1, W=0.51, T=13, N_w=6.42.

Through the laminar solution of the flow induced by a steadily rotating infinite disc, RH13 obtained an estimate of the time-averaged power spent to move the discs, which showed very good agreement with the power spent computed via DNS.

Inspired by previous works, the laminar flow above an infinite oscillating disc is therefore computed to calculate the power spent to activate the disc and to identify areas over the disc surface where the fluid performs work onto the discs, thus aiding the rotation. This is a form of the regenerative braking effect, studied by RH13 for steady disc rotation. These estimates are then compared with the turbulent quantities in §3.3.5.

3.2.1 Laminar flow over an infinite oscillating disc

The laminar oscillating-disc flow was studied for the first time by Rosenblat (1959) (refer to figure 3.2 for the flow geometry). The velocity components are

$$\{u_r^*, u_\theta^*\} = \frac{2r^*W^*}{D^*}\left\{F'\left(\eta,\breve{t}\right), G\left(\eta,\breve{t}\right)\right\}, \qquad u_y^* = -\frac{4W^*}{D^*}\sqrt{\frac{\nu^*T^*}{\pi}}F\left(\eta,\breve{t}\right), \quad (3.5)$$

where the prime denotes differentiation with respect to $\eta{=}y^*\sqrt{\pi/(\nu^* T^*)}$, the scaled wall-normal coordinate, $\breve{t}{=}2\pi t^*/T^*$ is the scaled time, and u_r^*, u_θ^* and u_y^* are the radial, azimuthal, and axial velocity components, respectively. The following boundary conditions are satisfied

$$\begin{aligned} y^* = 0: &\qquad u_r^* = 0, \quad u_\theta^* = (2r^* W^*/D^*)\cos\breve{t}, \quad u_y^* = 0, \quad p^* = 0. \\ y^* \to \infty: &\qquad u_r^* = 0, \quad u_\theta^* = 0. \end{aligned}$$

Expressions (3.5) are substituted into the cylindrical Navier-Stokes equations to obtain the equations of motion for F' and G under the boundary layer approximation,

$$\begin{aligned} \dot{F}' &= \frac{1}{2}F''' + \gamma(G^2 + 2FF'' - F'^2), \\ \dot{G} &= \frac{1}{2}G'' + 2\gamma(FG' - F'G), \end{aligned} \tag{3.6}$$

with boundary conditions

$$\begin{aligned} \eta = 0: &\qquad F = F' = 0, \quad G = \cos\breve{t}, \\ \eta \to \infty: &\quad F' = G = 0, \end{aligned} \tag{3.7}$$

where the dot denotes differentiation with respect to $\breve{t}$ and $\gamma{=}T^*W^*/(\pi D^*)$. The latter parameter represents the ratio between the oscillation period T^* and the period of rotation $\pi D^*/W^*$ which would occur if the disc rotated steadily with tip velocity W^*. The value $\gamma{=}\pi$ is relevant because it denotes the special case of maximum disc tip displacement equal to the circumference of the disc, i.e. each point at the disc tip covers a distance equal to πD^* during a half period of oscillation.

The system (3.6)-(3.7) was discretized using a first-order finite difference scheme for $\breve{t}$ and a second-order central finite difference scheme for η. The equations were first solved in time by starting from null initial profiles. The boundary condition for G was altered as $G\left(0,\breve{t}\right){=}1-e^{-\breve{t}}$ until G was sufficiently close to unity. The system was then integrated with the boundary condition

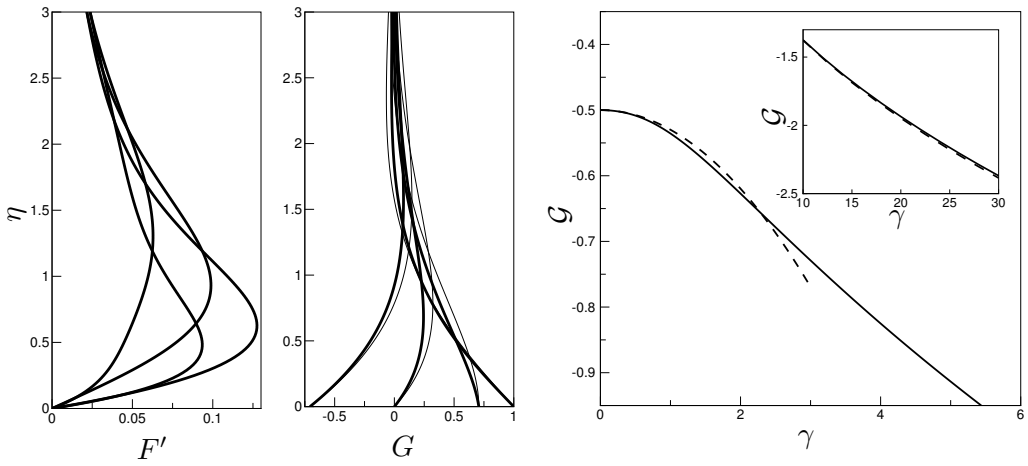

Fig. 3.4: Left: Wall-normal profiles of F' and G at different oscillation phases for γ=1 (thick lines) and γ=0 (thin lines). The latter is given by (3.13) and coincides with the classical Stokes layer solution. Right: Numerically computed values of $\mathcal{G}(\gamma)$ (solid lines) and asymptotic solutions, (3.12) for $\gamma \ll 1$ (dashed line in main plot), and (3.15) for $\gamma \gg 1$ (dashed line in inset).

$G\left(0,\breve{t}\right)=\cos\breve{t}$. Figure 3.4 (left) shows the wall-normal profiles of F' and G at different oscillation phases.

3.2.2 Laminar power spent

The laminar power spent $\mathcal{P}^*_{sp,l}$ is calculated using (2.6), where only $\mathbf{u_d}$ is retained in the laminar case as there is no mean streamwise flow above the disc and the turbulent fluctuations are null ($\mathbf{u_m}$=$\mathbf{u_t}$=0). Substituting u_d=$u_\theta \cos\theta$ and w_d=$u_\theta \sin\theta$ into (2.6), using (3.5) and averaging over θ, r, and time leads to

$$\mathcal{P}^*_{sp,l} = -\frac{\pi^{3/2}\mathcal{G}(\gamma)W^{*2}}{D_0^{*2}}\sqrt{\frac{\nu^*}{T^*}}\left(\frac{D^{*2}}{8}+\frac{c^*D^*}{3}+\frac{c^{*2}}{6}\right), \tag{3.8}$$

where

$$\mathcal{G}(\gamma) = \frac{1}{2\pi}\int_0^{2\pi} G\left(0,\breve{t}\right) G'\left(0,\breve{t}\right)\mathrm{d}\breve{t} \tag{3.9}$$

is shown in figure 3.4 (right). To express $\mathcal{P}^*_{sp,l}$ as percentage of the power spent to drive the fluid along the streamwise direction, (3.8) is divided by (2.8) to obtain

$$\mathcal{P}_{sp,l}(\%) = -\frac{100(\pi R_p)^{3/2}\mathcal{G}(\gamma)W^2}{U_b R_\tau^2 D_0^2\sqrt{T}}\left(\frac{D^2}{8}+\frac{cD}{3}+\frac{c^2}{6}\right). \tag{3.10}$$

Asymptotic limit for $\gamma \ll 1$: the Stokes-layer regime

To obtain an analytical approximation to $\mathcal{G}$ for $\gamma \ll 1$, the expanded form of G in powers of γ can be used,

$$G_{\gamma\ll1}(\eta,\breve{t},\gamma) = G_0(\eta,\breve{t}) + \gamma^2 G_2(\eta,\breve{t}) + \mathcal{O}(\gamma^3), \tag{3.11}$$

where G_0 and G_2 are given in equations (17) and (45) of Rosenblat (1959). Upon differentiation of (3.11) with respect to η, the asymptotic form of $\mathcal{G}(\gamma)$ is

$$\mathcal{G}_{\gamma\ll1}(\gamma) = \frac{1}{2\pi}\int_0^{2\pi} G_0(0,\breve{t})\left[G_0'(0,\breve{t})+\gamma^2 G_2'(0,\breve{t})\right]\mathrm{d}\breve{t} = -\frac{1}{2}+\frac{\gamma^2}{160}\left(15\sqrt{2}-26\right)+\mathcal{O}(\gamma^3), \tag{3.12}$$

which is shown in figure 3.4 (right). The asymptotic solution predicts the numerical solution well for $\gamma<2$.

In the limit $\gamma\ll1$, Rosenblat (1959) obtained a first-order solution

$$u^*_\theta = \frac{2r^*W^*}{D^*}e^{-\sqrt{\pi/(\nu^*T^*)}y^*}\cos\left(\frac{2\pi t^*}{T^*}-\sqrt{\frac{\pi}{\nu^*T^*}}y^*\right), \tag{3.13}$$

which is in the same form as the classical Stokes solution (Batchelor, 1967). Substituting (3.13) into (2.6), the first-order approximation is found, $\mathcal{P}^*_{sp,l} = 0.25W^*\sqrt{\pi\nu^*/T^*}$, which is expressed as percentage of (2.8) to obtain

$$\mathcal{P}_{sp,l,\gamma\ll1}(\%) = \frac{50(\pi R_p)^{3/2}W^2}{U_b R_\tau^2 D_0^2\sqrt{T}}\left(\frac{D^2}{8}+\frac{cD}{3}+\frac{c^2}{6}\right).$$

This is also found directly from (3.10) by setting $\mathcal{G}(0)=-0.5$.

Asymptotic limit for $\gamma \gg 1$: the quasi-steady regime

As suggested by Benney (1964), in the limit $\gamma\gg1$ it is more appropriate to rescale the wall-normal coordinate by the Ekman layer thickness $\delta^*_e=\sqrt{\nu^*D^*/(2W^*)}$.

The rescaled equations (2.19) and (2.20) of Benney (1964) were then solved using the same numerical method described in §3.2.1. The von Kármán equations describing the flow over a steadily rotating disc are recovered in the limit $\gamma \to \infty$. The asymptotic limit of $\mathcal{G}$ for $\gamma \gg 1$ is found by first rescaling $G'(0, \breve{t})$ in (3.9) through δ_e^* and by noting that the time modulation of the disc motion enters the problem only parametrically,

$$G'_{\gamma \gg 1}(0, \breve{t}) = \sqrt{2\gamma} G_s \cos \breve{t}, \tag{3.14}$$

where $G_s = -0.61592$ (Rogers & Lance, 1960). By substituting (3.14) into (3.9) and by use of (3.7), one finds

$$\mathcal{G}_{\gamma \gg 1}(\gamma) = G_s \sqrt{\frac{\gamma}{2}}. \tag{3.15}$$

As shown in figure 3.4 (right, inset), the asymptotic expression (3.15) matches the numerical values well. By substituting (3.15) into (3.10), the asymptotic form of the power spent is obtained

$$\mathcal{P}_{sp,l,\gamma \gg 1}(\%) = \frac{-100\pi G_s R_p^{3/2} W^{5/2}}{U_b R_\tau^2 D_0^2 \sqrt{2D}} \left(\frac{D^2}{8} + \frac{cD}{3} + \frac{c^2}{6} \right).$$

By coincidence, the power spent when $\gamma = 0$, i.e. (3.2.2), is half of the oscillating-wall case at the same W^* and T^* (Ricco & Quadrio, 2008), and the power spent when $\gamma \gg 1$, i.e. (3.2.2), is half of the steady-rotation case at the same W^* and D^* (RH13). The oscillating-disc power spent is expected to be smaller than in these two cases, but for different reasons. The oscillating-wall case requires more power because the motion involves the entire wall surface, while the steady-rotation case consumes more power because the motion is uniform in time.

3.2.3 Laminar regenerative braking effect

The laminar phase- and time-averaged power spent $\mathcal{W}_l$ to oscillate the discs beneath a uniform streamwise flow is computed by following RH13. As the purpose

of this analysis is to obtain a simple estimate of the turbulent case, the streamwise shear flow is superimposed on the Rosenblat flow without considering their nonlinear interaction. A rigorous study of this flow would be the extension of the work by Wang (1989) with oscillatory wall boundary conditions. Starting from (2.6), using (2.3), and setting $\mathbf{u_t}$=0, one finds

$$\mathcal{W}_l(x,0,z,\breve{t}) = \frac{1}{R_p}\left[u_d(x,0,z,\breve{t})\left(u'_m(0) + \left.\frac{\partial u_d}{\partial y}\right|_{y=0}\right) + w_d(x,0,z,\breve{t})\left.\frac{\partial w_d}{\partial y}\right|_{y=0}\right]. \tag{3.16}$$

Using (3.5), (3.16) becomes

$$\mathcal{W}_l(r,\breve{t}) = \frac{2rWG(0,\breve{t},\gamma)}{DR_p}\left(u'_m(0)\cos\theta + \frac{2Wr}{D}\sqrt{\frac{\pi R_p}{T}}G'(0,\breve{t},\gamma)\right).$$

By rearranging to obtain an inequality in r, the region where the streamwise flow exerts work on the disc (regenerative braking effect) is found,

$$r < -\frac{u'_m(0)D\cos\theta}{2WG'(0,\breve{t},\gamma)}\sqrt{\frac{T}{\pi R_p}}. \tag{3.17}$$

In §3.3.5, the region of regenerative braking effect is computed for the turbulent case and compared with the laminar prediction (3.17).

3.3 Turbulent flow

The turbulent flow results are presented in this section. Sections §3.3.1, §3.3.2, §3.3.3, §3.3.6 focus on the drag reduction, section §3.3.4 presents disc flow visualization and statistics, and section §3.3.5 describes the power spent to move the discs and the comparison with the laminar prediction, studied in §3.2.2.

3.3.1 Time evolution

The temporal evolution of the space-averaged wall-shear stress is displayed in figure 3.5 (left). The transient time occurring between the start-up of the disc forcing and the fully established disc-altered regime increases with $\mathcal{R}$. This agrees

with the oscillating wall and RH13, but the duration of the transient for the discs is shorter than for the oscillating wall case. The time modulation of the wall-shear stress is notable for the high $\mathcal{R}$ cases, with the amplitude of the signal increasing with T. The significant time modulation and the shorter transient compared with the oscillating wall technique could be due to the discs forcing the wall turbulence in the streamwise direction. The streamwise wall-shear stress is therefore affected directly whereas in the oscillating-wall case the streamwise shear flow is modified indirectly as the motion is along the spanwise direction only.

The space- and phase-averaged wall-shear stress modulation, shown by the dashed line in figure 3.5 (right), has a period equal to half of the wall velocity. This is expected because of symmetry of the unsteady forcing with respect to the streamwise direction. The wall-shear stress reaches its minimum value approximately $T/8$ after the disc velocity is maximum, i.e. at ϕ=5π/8, 13π/8. The wall-shear stress peaks approximately $T/8$ after the disc velocity is null, i.e. at ϕ=π/8, 9π/8.

3.3.2 Dependence of drag reduction on D, W, T

Figure 3.6 depicts maps of $\mathcal{R}(T,W)(\%)$ for disc sizes D=1.78, 3.38, 5.07, and 6.76. The γ values are shown as hyperbolae in these planes. For cases with $\gamma>\pi$, the maximum displacement is larger than the disc circumference. Figure 3.7 shows the same drag-reduction data, scaled in viscous units. The boxed values represent the net power saved $\mathcal{P}_{net}(\%)$ defined in (2.10). Only positive $\mathcal{P}_{net}$ values are shown and the bold boxes highlight the maximum $\mathcal{P}_{net}$ values.

For D=1.78 and 3.38 and fixed W, drag reduction increases up to an optimum T beyond which it decays. This optimum T depends on D, and increases with the disc diameter. For D=1.78, 3.38 the optimal periods are in the ranges T^+=200-

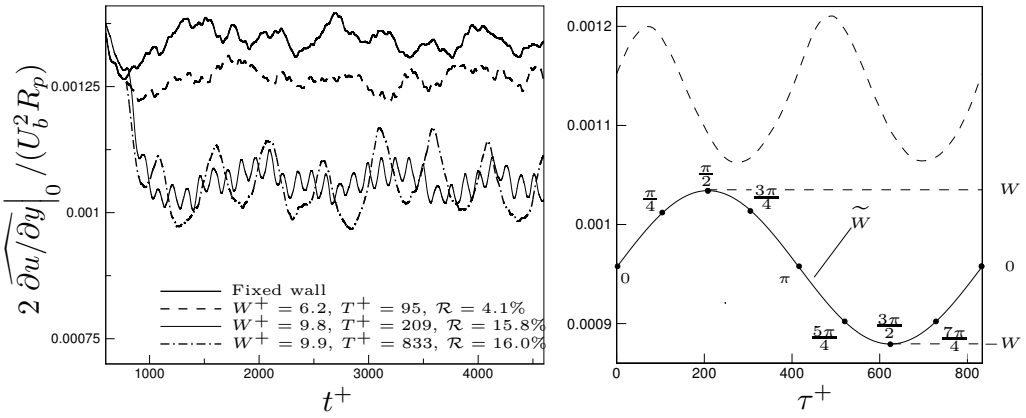

Fig. 3.5: Left: Space-averaged streamwise wall-shear stress vs. time for cases at D=3.38. The disc forcing is initiated at t^+=770. Only a fraction of the total integration time is shown. The space-averaging operator here does not include time averaging. Right: Ensemble- and space-averaged streamwise wall-shear stress vs. τ^+ for D^+=554, W^+=9.9, T^+=833 (dashed line). The disc velocity is shown by the solid line. The phase ϕ is given in the figure.

400 and T^+=400-800, respectively. For D=5.07 and 6.76 the optimal period is not computed and therefore $\mathcal{R}$ increases monotonically with T for fixed W and D. Cases with larger T are not investigated due to the increased simulation time required for the averaging procedure.

For D=1.78 and fixed T, drag reduction increases up to an optimum wall velocity of approximately W=0.26 (W^+=6), above which drag reduction decreases. This behaviour also occurs in the steady-disc case studied by RH13. The optimal W are not found for larger D as the drag reduction increases monotonically with W for fixed D and T.

For $T \gg 1$, the wall forcing is quasi-steady and it is therefore worth comparing the $\mathcal{R}$ value with the ones obtained by steady disc rotation, computed by RH13. RH13's values are however not expected to be recovered in this limit. A primary reason for this is that the power spent in the oscillating-disc case is smaller than in the steady rotation case, as verified in §3.3.5 (in §3.2.2, it is predicted to be

half of the steady case by use of the laminar solution when the oscillation period is large). RH13's values are displayed in figure 3.7 by the dark grey circles on the right-hand side of each map. In most of the cases where the optimal T^+ is detected, i.e. for W^+>3, D=1.78, and for W^+>9, D=3.38 and 5.07, our $\mathcal{R}$ values may reach larger values than RH13's for the same W^+. For D=6.76, all our computed $\mathcal{R}$ are lower than RH13's.

Figure 3.7 also shows that a positive $\mathcal{P}_{net}$ occurs only for $W^+\leq$9. This confirms the finding by RH13 for steady rotation and is expected because the power spent grows rapidly as W grows, as also suggested by the laminar result in (3.10). The largest positive $\mathcal{P}_{net}$ in the parameter range is $6 \pm 1\%$, and is obtained for D^+=855, W^+=6.4, T^+=880, and D^+=568, W^+=6.4, T^+=874.

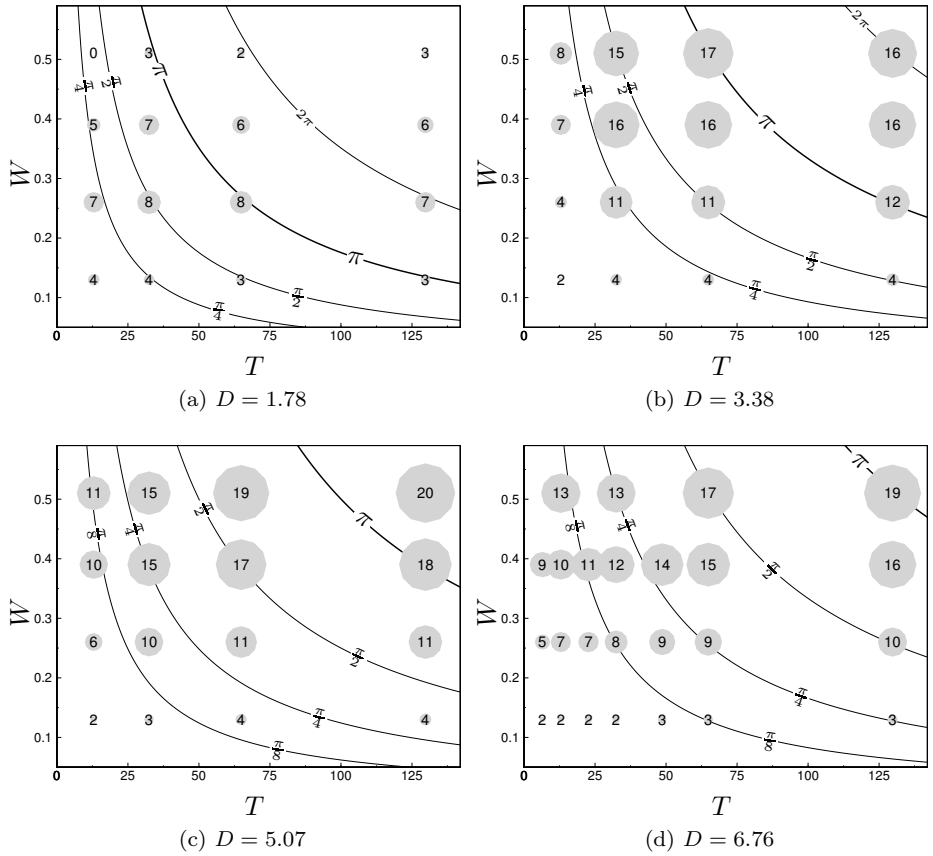

(a) $D = 1.78$ (b) $D = 3.38$

(c) $D = 5.07$ (d) $D = 6.76$

Fig. 3.6: Plots of $\mathcal{R}(T, W)(\%)$ for different D. The circle size is proportional to the drag reduction value. The hyperbolae are constant-γ lines.

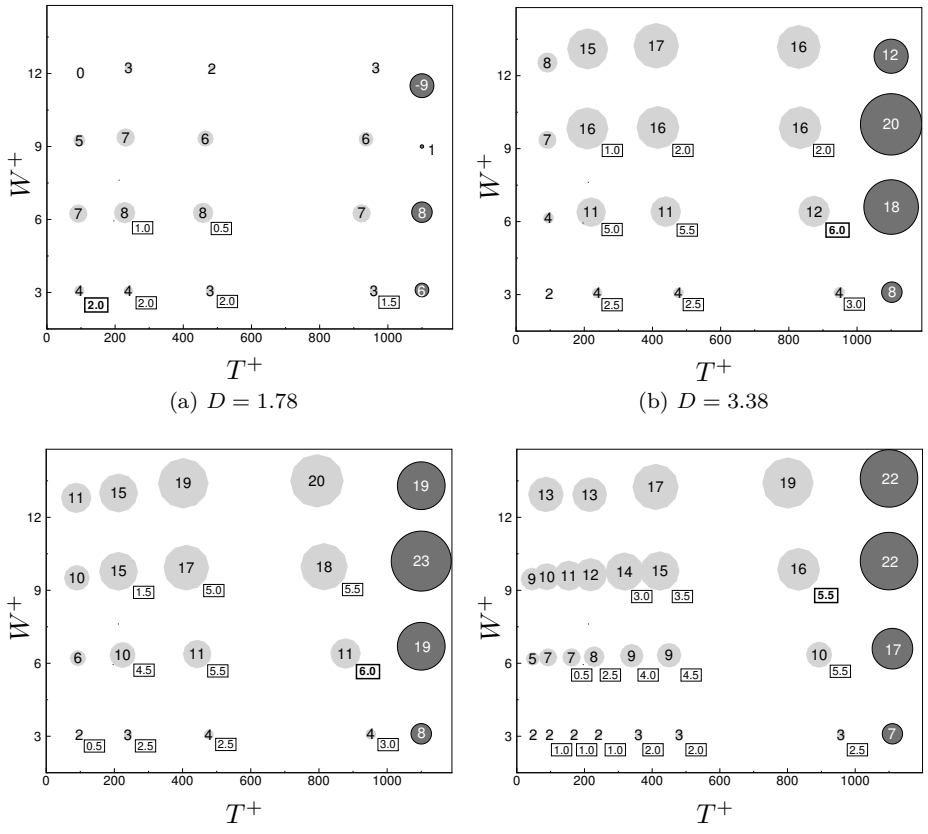

(a) $D = 1.78$ (b) $D = 3.38$

(c) $D = 5.07$ (d) $D = 6.76$

Fig. 3.7: Plots of $\mathcal{R}(T^+, W^+)(\%)$. Scaling is performed using u_τ^* from the native case. The dark grey circles indicate RH13's data and the boxed values denote positive P_{net} values.

3.3.3 The Fukagata-Iwamoto-Kasagi identity

The Fukagata-Iwamoto-Kasagi (FIK) identity relates the skin-friction coefficient of a wall-bounded flow to the Reynolds stresses (Fukagata *et al.*, 2002). It is extended here to take into account the oscillating-disc flow effects (the reader should refer to Appendix A of RH13 for a slightly more detailed derivation for the steady disc flow case). By non-dimensionalizing the streamwise momentum equation into outer units, decomposing the velocity field as discussed in §2.2 and averaging in time, along the homogeneous x and z directions, and over both

halves of the channel, the following is obtained

$$\Pi Re_p = \left(u'_m - \widehat{u_d v_d} - \widehat{u_t v_t}\right)',$$

where the prime indicates differentiation with respect to y. By following the same procedure outlined in Fukagata *et al.* (2002) and noting that the Reynolds stresses term $\widehat{u_t v_t}$ in equation (1) in Fukagata *et al.* (2002) is replaced with the sum $\widehat{u_t v_t} + \widehat{u_d v_d}$, the relationship between C_f and the Reynolds stresses for the disc flow case can be written as

$$C_f = \frac{6}{U_b Re_p} - \frac{6}{U_b^2}\left[(1-y)\left(\widehat{u_t v_t} + \widehat{u_d v_d}\right)\right]_g, \tag{3.18}$$

which is in the same form of the steady case by RH13. The drag reduction computed through the Reynolds stresses via (3.18) is $\mathcal{R}$=16.9% for D=3.38, W^+=13.2 and T^+=411, which agrees with $\mathcal{R}$=17.1%, calculated via the wall shear-stress. Using (3.18), it is also possible to separate the total drag reduction into the change of the turbulent Reynolds stresses $\widehat{u_t v_t} - \langle\widehat{u_{t,s} v_{t,s}}\rangle$ and the contribution of the time averaged disc Reynolds stresses $\widehat{u_d v_d}$, i.e. $\mathcal{R}(\%)=\mathcal{R}_t(\%)+\mathcal{R}_d(\%)$ where

$$\mathcal{R}_t(\%) = 100\frac{R_p\left[(1-y)\left(\widehat{u_t v_t} - \langle\widehat{u_{t,s} v_{t,s}}\rangle\right)\right]_g}{U_b - R_p\left[(1-y)\langle\widehat{u_{t,s} v_{t,s}}\rangle\right]_g}, \tag{3.19}$$

$$\mathcal{R}_d(\%) = 100\frac{R_p\left[(1-y)\,\widehat{u_d v_d}\right]_g}{U_b - R_p\left[(1-y)\langle\widehat{u_{t,s} v_{t,s}}\rangle\right]_g}. \tag{3.20}$$

The subscript s again refers to the stationary wall case. This decomposition is used in section §3.3.6 to study the drag reduction physics.

3.3.4 Disc flow visualizations and statistics

The disc flow for D^+=552, W^+=13.2 and T^+=411 ($\mathcal{R}$=17%) is visualized at different phases in figure 3.8. Isosurfaces of $q^+=\sqrt{u_d^{+2}+w_d^{+2}}$=2.1 are displayed. Similarly to the steady case by RH13, streamwise-elongated tubular structures appear between discs, which extend vertically up to almost one quarter of the

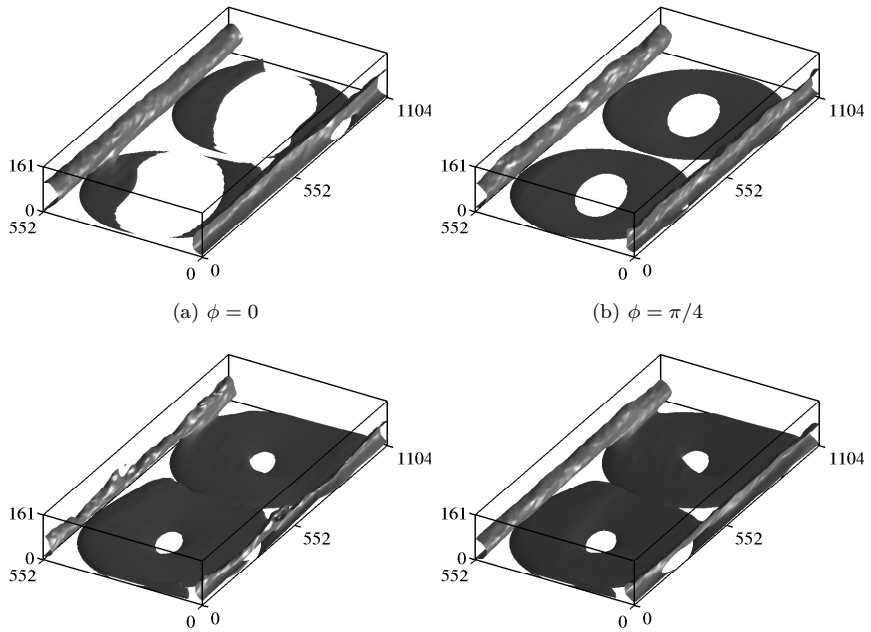

(a) $\phi = 0$ (b) $\phi = \pi/4$

(c) $\phi = \pi/2$ (d) $\phi = 3\pi/4$

Fig. 3.8: Disc-flow visualizations of $q^+(x,y,z)=\sqrt{u_d^{+2}+w_d^{+2}}$=2.1 at phases ϕ=0, $\pi/4$, $\pi/2$, and $3\pi/4$. The disc tip velocity at each phase is shown in figure 3.5 (right). In this figure and in figures 3.9, 3.10, 3.11, and 3.13, D^+=552, W^+=13.2, T^+=411.

channel height. They occur where there is high tangential shear, i.e. where the disc tips are next to each other and rotate in opposite directions, but also over sections of stationary wall. They persist almost undisturbed across the entire period of oscillation, their intensity and shape being only weakly modulated in time. The thin circular patterns on top of the discs instead show a strong modulation in time. This is expected as the patterns are directly related to the disc wall motion. Although at ϕ=0 the disc velocity is null, the circular patterns are still observed as the rotational motion has diffused upward from the wall by viscous effects. Instantaneous isosurfaces of low-speed streaks in the proximity of the wall (not shown) reveal that the intensity of these structures is weakened significantly, similarly to the steady disc-flow case.

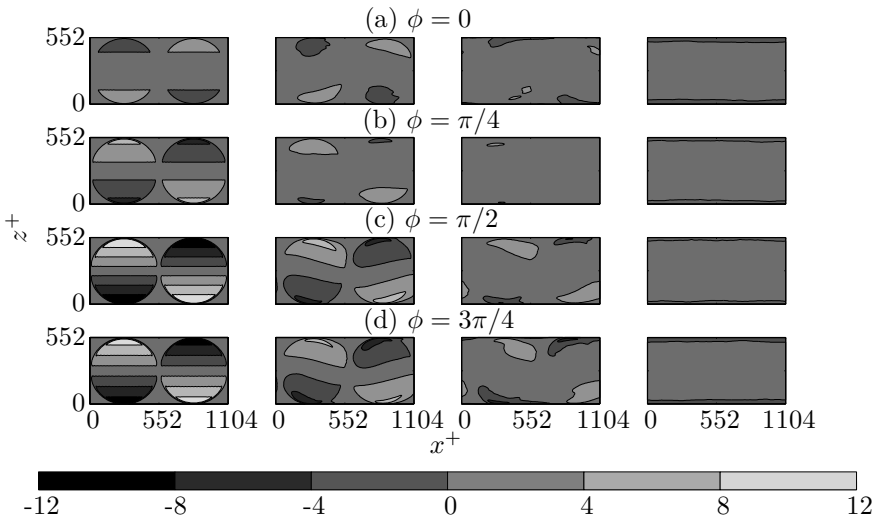

Fig. 3.9: Contour plot of $u_d^+(x, y, z)$ as a function of phase in the $x - z$ plane at y^+=0, y^+=4, y^+=8 and y^+=27 (from left to right).

Contour plots of u_d in $x - z$ planes are shown in figure 3.9. The first column on the left shows the contour at the wall. At y^+=4 and y^+=8, the disc outlines can still be observed, the clarity decreasing with the increased distance from the wall. At these heights the contour lines are no longer straight, but show a wavy modulation. The circular patters created by the disc motion are displaced in the streamwise direction by the mean flow. The magnitude of the shift increases with distance from the wall and at y^+=8 it is about $100\nu^*/u_\tau^*$. At y^+=27 the disc outlines are no longer visible and the structures occurring between discs in figure 3.8 here appear as streamwise-parallel bands of u_d which do not modulate in time and are slower than the mean flow. They also appear at higher wall-normal locations up to the channel half-plane, with their width increasing with height.

The contour plots in figure 3.10 show the ensemble- and time-averaged wall-shear stress. At phases ϕ=0 and π, when the angular velocity of the discs is zero, the wall-shear stress is almost uniform over the disc surface. During the other phases of the cycle, the lines of constant stress are inclined with respect to the streamwise direction and the maximum values are found near the disc tip. The

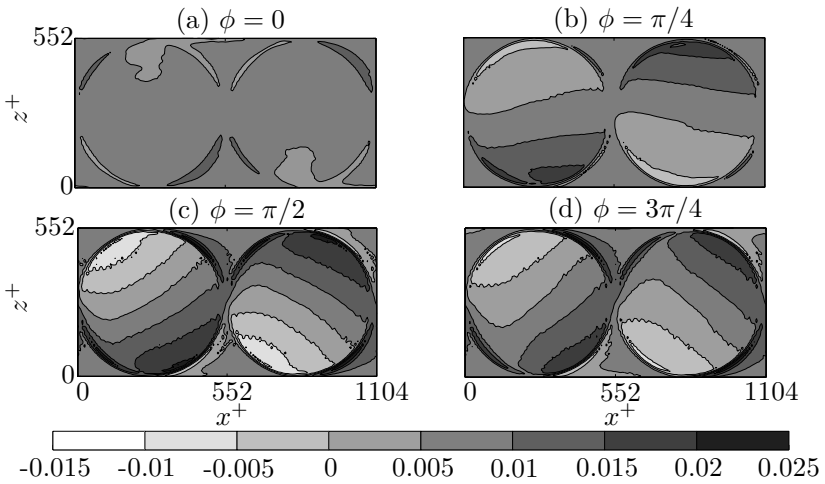

Fig. 3.10: Contour plot of phase-averaged streamwise wall friction, $2\langle \partial u^+/\partial y^+|_0 \rangle / U_b^{+2}$. The skin-friction coefficient is $C_f = 6.79 \cdot 10^{-3}$.

lines show a maximum inclination of about 45° at phases $\phi = 3\pi/4,\ 7\pi/4$, when the deceleration of the discs is maximum.

Figure 3.11 (left) shows contours of the time-averaged $\langle u_d v_d \rangle$ observed from the y-z plane at different streamwise locations. These contours overlap with the elongated structures in figures 3.8 and 3.9, which are therefore recognized as primarily responsible for these additional Reynolds stresses. It is clear that the structures are only slowly varying along the streamwise direction. The flow over the disc surface does not contribute to $\langle u_d v_d \rangle$ because, although u_d is significant, v_d is negligible. Only the contribution to $\langle u_d v_d \rangle$ from both negative u_d and v_d is included in figure 3.11 (left) as u_d and v_d with other combinations of signs only negligibly add to the total stress. The structures are therefore jets oriented toward the wall and backward with respect to the mean flow.

Figure 3.11 (right) shows the time modulation of the root-mean-square (r.m.s.) of the disc streamwise velocity component, defined as $u_{d,rms}(y,\tau) = \sqrt{\widehat{u_d^2}}$, and of the Reynolds stresses $\widehat{u_d^+ v_d^+}$ (where here the spatial average $\widehat{\cdot}$ does not include the time average as in (2.2)). Four profiles are shown for each quantity, for

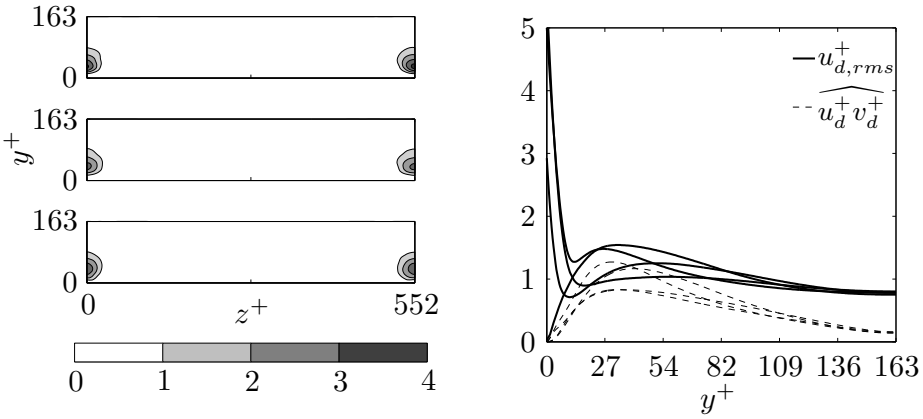

Fig. 3.11: Left: Isosurfaces of $\langle u_d^+ v_d^+ \rangle$ observed from the $y-z$ plane at x^+=0, x^+=160, x^+=320 (from left to right). The plot shows only $\langle u_d^+ v_d^+ \rangle$ for u_d, v_d<0 as within the contour range the contributions from other combinations of u_d and v_d are negligible. Right: Wall-normal profiles of the $u^+_{d,rms}$ (solid lines) and $\widehat{u_d^+ v_d^+}$ (dashed lines). Profiles are shown for phases from the first half of the disc oscillation.

phases from the first half period of the oscillation. Data from the second half are not shown as the profiles coincide at opposite oscillation phases. The disc flow penetrates into the channel up to $y^+ \approx 15$. When the disc tip velocity is close to its maximum, the profiles of $u_{d,rms}$ and $w_{d,rms}$ (the latter not shown) decay from their wall value and follow each other closely up to $y^+ \approx 10$. At higher locations, the magnitude of $u^+_{d,rms}$ is larger than that of the wall-normal and spanwise velocity profiles.

In the bulk of the channel, for y^+>50, the profiles modulate only slightly in time. This therefore further confirms that the intense temporal modulation of the disc flow is confined in the viscous sublayer and buffer region. $u^+_{d,rms}$ decays to ≈0.7 as the channel centreline is approached. As expected, the Reynolds stresses $\widehat{u_d^+ v_d^+}$ show a slow time modulation and are always positive, proving that the streamwise-elongated structures favourably contribute to the drag reduction through $\mathcal{R}_d$ in (3.20). Neither $u^+_{d,rms}$ nor $\widehat{u_d^+ v_d^+}$ modulate in time for y^+>120.

3.3.5 Power spent

Comparison with laminar power spent

Figure 3.12 (left) shows the comparison between the power spent $\mathcal{P}_{sp,t}$ to impose the disc motion, computed via (2.9) with DNS data, and the laminar power spent, calculated via (3.10). The values match satisfactorily for low $\mathcal{P}_{sp,t}$, and the disagreement grows for larger $\mathcal{P}_{sp,t}$. This is due to the larger values of W, which intensify the nonlinear interactions between the disc flow and the streamwise turbulent mean flow, and promote the interference between neighbouring discs. As the laminar calculations are performed by not accounting for the disc interference through the assumption of infinite disc size and by neglecting the streamwise mean flow, the agreement is expected to worsen for large W. Figure 3.12 (left) also shows that the power spent for cases with positive $\mathcal{P}_{net}$ is predicted more accurately by the laminar solution than for cases with negative $\mathcal{P}_{net}$, a result also found by RH13.

Figure 3.12 (right) presents the same data of the right plot, with the symbols coloured according to T. The agreement is best for the largest oscillation periods, T=130, and it worsens as T decreases. The trend for T=130 closely resembles the one of the steadily rotating discs by RH13, which is consistent with the wall forcing becoming quasi-steady at large periods. For T=130, the highest value of $\mathcal{P}_{sp,t}$=37%, occurring for D=1.78, W=0.51, differs from $\mathcal{P}_{sp,l}$ by 17%, while a disagreement of 15% is found by RH13 for the same $\mathcal{P}_{sp,l}$ value.

Turbulent regenerative braking effect

For the majority of oscillation cycle, power is spent by the discs to overcome the frictional resistance of the fluid. However, for part of the oscillation, work is performed by the fluid on the disc. This is a form of the regenerative breaking effect which also occurs for the case of uniform spanwise wall oscillations. Contour

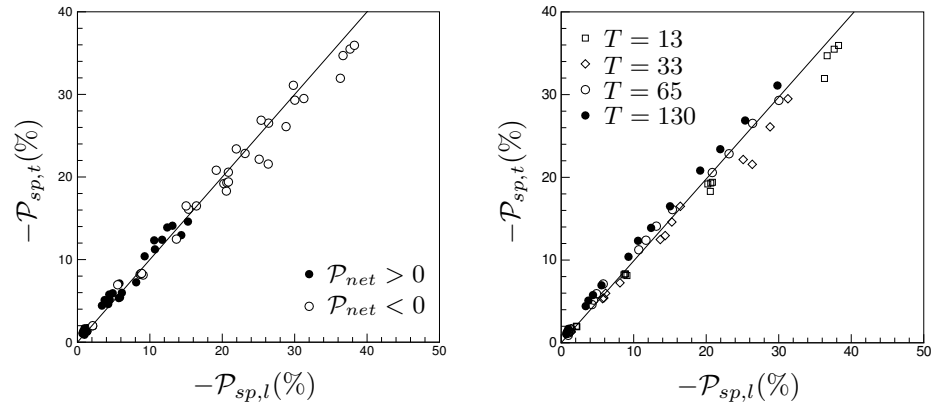

Fig. 3.12: Left: $\mathcal{P}_{sp,t}(\%)$, computed through DNS via (2.9), vs. $\mathcal{P}_{sp,l}(\%)$, computed through (3.10), the power spent by an infinite disc oscillating beneath a still fluid. Data are coloured according to $\mathcal{P}_{net}$. Right: $\mathcal{P}_{sp,t}(\%)$ vs. $\mathcal{P}_{sp,l}(\%)$, with symbols grouped according to T.

plots of the localized power spent $\mathcal{W}_t$, defined as

$$\mathcal{W}_t(x,z,\tau)(\%) = \frac{100R_p}{R_\tau^2 U_b}\left(u_d\frac{\partial u_d}{\partial y}\bigg|_{y=0} + w_d\frac{\partial w_d}{\partial y}\bigg|_{y=0}\right), \tag{3.21}$$

are shown in figure 3.13 for $\phi{=}\pi/4$, $3\pi/4$. The white regions over the disc surface correspond to the regenerative braking effect, where $\mathcal{W}_t{\geq}0$, i.e. the fluid performs work on the discs. The dashed lines represent the regions of $\mathcal{W}_l(r,\tau){>}0$, predicted through the laminar solution by (3.17). Although the regenerative braking areas computed via DNS are slightly shifted upstream when compared with those predicted through the laminar solution, the overall agreement is very good and better than in RH13's case.

3.3.6 A discussion on drag reduction physics and scaling

The results in the preceding sections prove that the oscillating discs effectively modify the flow in two distinct ways, which are discussed in the following and illustrated in figure 3.14.

- *Role of disc boundary layer*

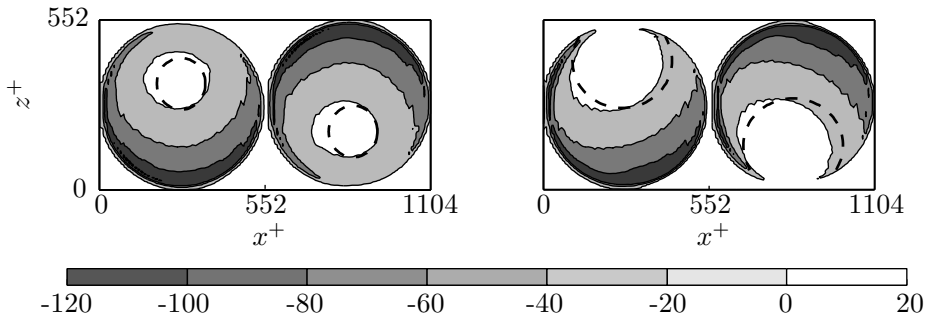

Fig. 3.13: Spatial variation of $\mathcal{W}_t$, computed via (3.21), for $\phi{=}\pi/4$ (left) and $\phi{=}3\pi/4$ (right). The white areas over the disc surfaces for which $\mathcal{W}_t{>}0$ denote locations where the fluid is performing work onto the disc. The areas of regenerative braking predicted by the laminar solution, i.e. where $\mathcal{W}_l{>}0$ and (3.17) applies, are enclosed by the dashed lines.

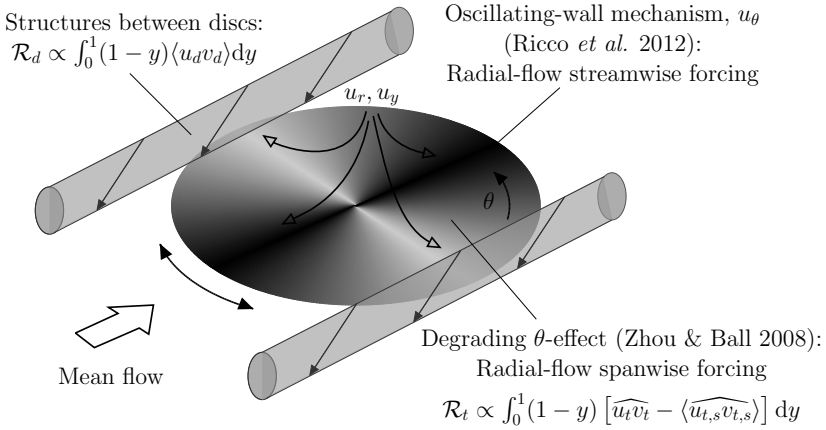

Fig. 3.14: Schematic of the two mechanisms responsible for drag reduction induced by oscillating discs. One mechanism is linked to the attenuation of the turbulent Reynolds stresses and is quantified by $\mathcal{R}_t$ in (3.19). The degrading effect of the oscillation angle θ (Zhou & Ball, 2008) is represented by the shading. The second mechanism is due to the structures between discs and is quantified by $\mathcal{R}_d$ in (3.20). The radial streaming induced by the Rosenblat pump is denoted by the open arrows.

The circular pattern which forms over a disc as a direct consequence of the disc rotation (shown in figure 3.8) is a thin region of high-shear flow.

The laminar analysis suggests that this oscillatory boundary layer resembles the oscillating-wall Stokes layer (of thickness $\delta_s^*=\sqrt{\nu^* T^*}$) at high frequency (refer to §3.2.2 when $\gamma \ll 1$), and the Ekman layer of the von Kármán viscous pump (of thickness $\delta_e^*=\sqrt{\nu^* D^*/(2W^*)}$) at high periods (refer to §3.2.2 when $\gamma \gg 1$). It is therefore reasonable to expect that the wall turbulence over the disc surface is modified similarly to the oscillating-wall case at high frequency and to the steady-rotation case studied by RH13 at high periods. The parameter γ, written as $\gamma=(2/\pi)\,(\delta_s^*/\delta_e^*)^2$, can be interpreted as the threshold that distinguishes these two limiting regimes. The thinner boundary layer between these two limits dictates the way the turbulence is altered. When $\gamma=\mathcal{O}(1)$, an intermediate oscillating-disc forcing regime is identified, for which viscous effects diffuse from the wall due to both unsteady oscillatory effects and to large-scale rotational motion.

When $\gamma \ll 1$, the drag-reduction mechanism is analogous to the one advanced by Ricco *et al.* (2012) for the oscillating-wall flow, namely that the near-wall periodic shear acts to increase the turbulent enstrophy and to attenuate the Reynolds stresses. Important differences from the oscillating-wall case are i) the wallward motion of high-speed fluid, entrained by the disc oscillation from the interior of the channel, ii) the radial-flow effects due to centrifugal forces, which are proportional to the nonlinear term F'^2 (refer to (3.6) for the laminar case) and produce additional spanwise forcing in planes perpendicular to the streamwise direction, iii) the radial dependence of the forcing amplitude, and iv) the degrading effect on drag reduction due to wall oscillations which are not spanwise oriented. The latter effect was first documented by Zhou & Ball (2008), who proved that spanwise wall oscillations produce the largest drag reduction, while streamwise wall oscillations lead to approximately a third of the spanwise-oscillation value. The shad-

ing on the disc surface in figure 3.14 illustrates the effectiveness of the wall oscillations at different orientation angles.

- *Role of quasi-steady inter-disc structures*

  The second contribution is from the tubular interdisc structures, which are streamwise-elongated and quasi-steady as they persist throughout the disc oscillation. They are primarily synthetic jets, an indirect byproduct of the disc rotation (as in RH13) or disc oscillation. As discussed in §3.3.4, these jets are directed wallward and backward with respect to the mean flow u_m. The time-averaged flow between discs is therefore retarded with respect to the mean flow. Further insight into the generation of these structures could lead to other actuation methods leading to a similar drag reduction benefit. Although the structures appear directly above the regions of high shear created by neighbouring discs in the spanwise direction, they are largely unaffected by the time-modulation of the shear. These structures could be a product of the interaction between the radial streaming flows of neighbouring discs, which have a non-zero mean (refer to figure 3.4 (left)).

The FIK identity is useful because the role of disc boundary layer on drag reduction is distilled into $\mathcal{R}_t$, which sums up the decrease of turbulent Reynolds stresses, while the role of the structures is given by $\mathcal{R}_d$, which is solely due to the additional disc-flow Reynolds stresses. $\mathcal{R}_t$ and $\mathcal{R}_d$ quantify mathematically the two drag-reduction effects.

It has been shown that drag reduction scales linearly with the penetration depth of the laminar layer for different spanwise wall forcing conditions, such as spatially uniform spanwise oscillation, travelling and steady wall waves (Ricco *et al.*, 2012; Cimarelli *et al.*, 2013). An analogous scaling is obtained in the following. The definition of the oscillating-wall penetration depth advanced by Choi *et al.* (2002) is modified to account for the viscous diffusion effects induced

by the disc oscillation. Choi *et al.* (2002)'s definition is employed because it takes into account the influence of the wall forcing amplitude, which was not necessary in Quadrio & Ricco (2011) because the wave amplitude was constant. Following the discussion on the role of the disc boundary layer on drag reduction, the crucial point is that only $\mathcal{R}_t$, i.e. the portion of drag reduction related to the attenuation of the turbulent Reynolds stresses, is scaled with the penetration thickness. The scaling is carried out for the case with the largest diameter, D=6.76, for which the infinite-disc laminar flow solution best represents the disc boundary layer flow because of the limited interference between discs.

From the envelope of the Stokes layer velocity profile engendered by an oscillating wall

$$W_e^+ = W_m^+ \exp\left(-\sqrt{\pi/T^+}y^+\right),$$

Choi *et al.* (2002) defined the penetration depth as

$$y_d^+ = \sqrt{T^+/\pi}\ln\left(W_m^+/W_{th}^+\right),$$

where W_m^+ is the maximum wall velocity and W_{th}^+ is a threshold value below which the induced spanwise oscillations have little effect on the channel flow. For the oscillating disc case, the enveloping function for the laminar azimuthal disc velocity, W_e^+=$W^+G_e(\eta,\gamma)$, where

$$G_e(\eta,\gamma) = \max_{\breve{t}} G(\eta,\breve{t},\gamma),$$

plays a role analogous to the exponential envelope for the classical Stokes layer. Defining the inverse of G_e, L=G_e^{-1}, the penetration depth of the oscillating-disc layer is obtained as

$$\delta^+ = \sqrt{T^+/\pi}\ \mathsf{L}\left(W^+/W_{th}^+\right). \tag{3.22}$$

Note that in the limit of $\gamma \to 0$ one finds

$$\lim_{\gamma\to 0}\mathsf{L}\left(W^+/W_{th}^+\right) = \ln\left(W^+/W_{th}^+\right).$$

The Stokes layer penetration depth is therefore obtained as a special case. In figure 3.15 (left), the drag-reduction contributor $\mathcal{R}_t$ shows a satisfactory linear scaling with the penetration depth, computed via (3.22) with W_{th}^{+}=2.25.

In order to find a scaling for $\mathcal{R}_d$, the portion of drag reduction only due to the inter-disc structures, the FIK identity and the laminar solution discussed in §3.2 are employed. From (3.20), it is evident that $\mathcal{R}_d$ is proportional to $\widehat{u_d v_d}$. Through the definitions of the laminar velocity components (3.5), $u_d \sim W$ and $v_d \sim W\sqrt{T}$. It then follows that a reasonable estimate could be $u_d v_d \sim W^2\sqrt{T}$ at the edge of the discs where the structures appear. It is then logical to look for a scaling of $\mathcal{R}_d$ in the form $W^m T^n$. An excellent linear fit for the drag reduction data is found for $(m,n)=(2,0.3)$, as shown in figure 3.15 (right). Outer-unit scaling for W and T applies, which means that the structures are not influenced by the change in u_τ^*. The exponent of W is as predicted by the laminar solution. The deviation of the coefficient n from that predicted by the laminar analysis (i.e. n=0.5) can be accounted for by the factors which are not taken into account in the laminar analysis, such as the disc-flow interaction with the streamwise turbulent flow and between neighbouring discs.

3.4 Outlook

In line with the analysis by RH13 for the steady disc-flow technique, it is instructive to render the scaled oscillating disc forcing parameters dimensional to guide laboratory experiments and to estimate the characteristic length and time scales of the wall forcing for flows of technological relevance. Table 3.1 displays estimated data for three flows of industrial interest and two flows of experimental interest with the optimal parameters D=6.76, W=0.39, and T=130, which lead to $\mathcal{R}$=16% and $\mathcal{P}_{net}$=5.5%. This table may be compared with the analogous table 6 in RH13 for the steady rotation case, although it should be noted that f^* indi-

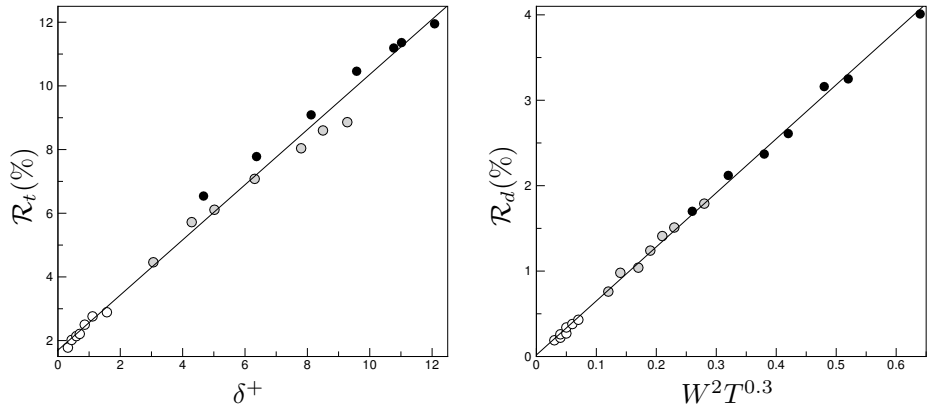

Fig. 3.15: Left: $\mathcal{R}_t$, the contribution to drag reduction due to turbulent Reynolds stress attenuation, vs. δ^+, the penetration depth, defined in (3.22). Right: $\mathcal{R}_d$, the contribution to drag reduction due to the disc-flow Reynolds stresses, vs. $W^2T^{0.3}$. The diameter is D=6.76. White circles: W^+=3, light grey: W^+=6, black: W^+=9.

cates the oscillation frequency in the present case ($f^*=2\pi/T^*$) and the rotational frequency in RH13's case ($f^*=\omega^*/2\pi$, where ω^* is the angular velocity).

Experimental realization of the disc-flow technique is possible with D^*=4 – 8 cm, W^*=0.2 m/s in a water channel and 4.6 m/s in a wind tunnel. The frequencies are f^*=0.37 Hz and 16 Hz, respectively. The dimensional parameters in flight are D^*=5.8 mm, W^*=70.7 m/s, and f^*=1752 Hz. Commercially available electromagnetic motors (D^*=2 mm, $f^*=\mathcal{O}(10^3)$ Hz), adapted for oscillatory motion, would guarantee these time and length scales of forcing (Kuang-Chen Liu *et al.*, 2010). The optimal frequency in flight is approximately half of the optimal one for steady rotation: f^*=1752 Hz for the oscillating discs compared to f^*=3718 Hz for the steady rotating discs.

Figure 3.16 shows characteristic time and length scales of the oscillating-disc technique and of other drag reduction methods. The typical length scale of the oscillating-disc technique is larger than that of the steadily rotating discs and the standing wave forcing, whilst being two orders of magnitude greater than both

riblets and the feedback control systems studied by Yoshino *et al.* (2008). The typical time scale of the oscillating disc flow is one order of magnitude larger than that of the oscillating wall forcing. It is also worth pointing out that these are optimal values for the tested parameter range and that our results in §3.3.2 hint at the possibility to obtain comparable drag-reduction values for even larger oscillation periods and diameters, which are denoted by the dashed lines in figure 3.16.

This discussion is closed by mentioning another advantage of the oscillating-disc flow when compared to the steady-disc flow by RH13. As shown in figure 3.6 (d), it is possible to achieve $\mathcal{R}$=13% with $\gamma=\pi/8$, T=12, W=0.51, i.e. the disc tip undertakes a maximum displacement of only 1/8 of the disc circumference. Therefore, for this case the disc-flow technique could be realized in a laboratory by use of a thin elastic seal between the disc and the stationary wall. This design would eliminate any clearance around the discs, which would not be possible for the case of steady rotation.

Parameter	Flight (BL)	Ship (BL)	Train (BL)	WT (BL)	WC (CF)
U^* (m/s)	225	10	83	11.6	0.4
$\nu^* \cdot 10^6$ (m^2/s)	35.3	1.5	15.7	15.7	1.1
x^* (m)	1.5	1.5	1.8	1.0	-
h^* (mm)	22	22	27	25	10
u_τ^* (m/s)	7.9	0.4	2.9	0.5	0.02
Re_τ	4970	4970	4970	800	180
$C_f \cdot 10^3$	2.4	2.4	2.4	3.8	8.1
D^* (mm)	5.7	5.6	6.9	39.6	70.9
W^* (m/s)	70.7	3.1	26.1	4.6	0.2
T^* (ms)	0.6	12.5	1.9	61	2700
f^* (Hz)	1752	80	536	16	0.4

Tab. 3.1: Dimensional quantities for the optimum $\mathcal{P}_{net}$ case for three flows of industrial and two of experimental interest (D=6.76, W=0.39 and T=130). In the headings (BL) indicates a turbulent boundary layer with no pressure gradient, and (CF) indicates a pressure-driven channel flow. WT and WC stand for wind tunnel and water channel respectively. For headings marked BL, U^* represents the free-stream mean velocity, x^* is the downstream location and h^* the boundary layer thickness; whilst for the CF case U^* represents the bulk velocity and h^* the channel half-height. The relations used: h^*=$0.37x^*(x^*U^*/\nu^*)^{-0.2}$ and C_f=$0.37\left[\log_{10}(x^*U^*/\nu^*)\right]^{-2.584}$ for BL; C_f=$0.0336R_\tau^{-0.273}$ for CF are from Pope (2000).

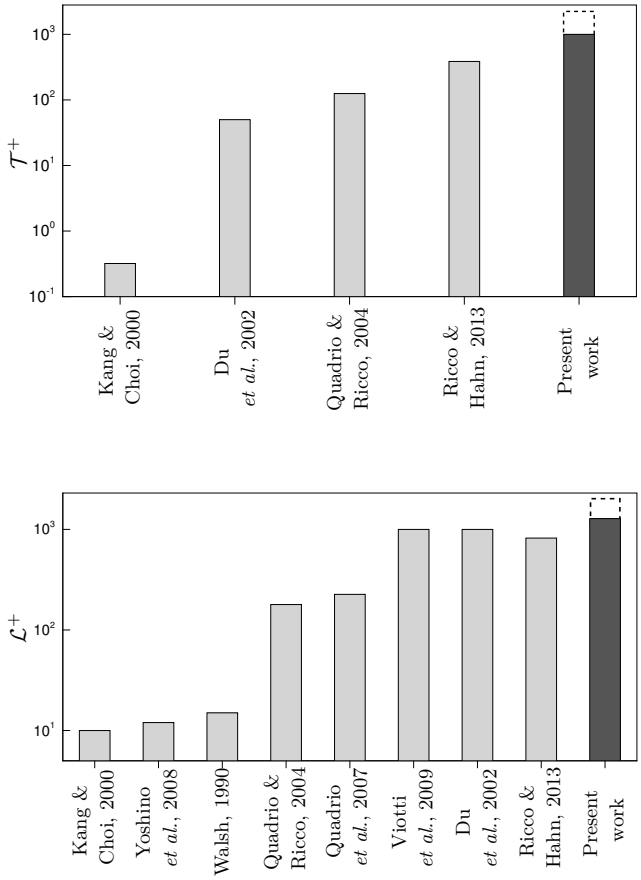

Fig. 3.16: Characteristic optimal time and length scales, $\mathcal{T}^+$, $\mathcal{L}^+$, for a range of drag reduction methods are shown for comparison with the oscillating disc technique. From left to right the time scales are given as follows: time between successive flow field measurements (Kang & Choi, 2000), period of transverse travelling wave forcing (Du *et al.*, 2002), period of spanwise wall oscillations (Quadrio & Ricco, 2004), period of rotation of steady disc forcing (Ricco & Hahn, 2013), and period of disc oscillation. From left to right the length scales are given as follows: maximum displacement of wall-normal wall motions (Kang & Choi, 2000), spacing of sensors for feedback control of wall deformation (Yoshino *et al.*, 2008), riblet spacing (Walsh, 1990), maximum displacement of temporally oscillating wall (Quadrio & Ricco, 2004), wavelength of streamwise-sinusoidal wall transpiration (Quadrio *et al.*, 2007), wavelength of standing wave forcing (Viotti *et al.*, 2009), wavelength of transverse travelling wave forcing (Du *et al.*, 2002), diameter of steady discs (Ricco & Hahn, 2013), and diameter of oscillating discs.

4. ARRANGEMENTS OF DISC ACTUATORS

In this chapter the effect of wall arrangement on steadily rotating discs is investigated. As the disc motion is now steady, the averaging procedure is different and so is reviewed here. The time average is defined as

$$f(x,y,z) = \frac{1}{t_f - t_i}\int_{t_i}^{t_f} \overline{f}(x,y,z,t)\mathrm{d}t,$$

where t_i and t_f denote the start and finish of the averaging time, respectively. Finally, the spatial average along the homogeneous directions is defined as

$$\hat{f}(y) = \frac{1}{L_x L_z}\int_0^{L_x}\int_0^{L_z} \langle f\rangle(x,y,z)\mathrm{d}z\mathrm{d}x.$$

4.1 Introduction of disc layouts

The discs are located on both walls, have diameter D and rotate steadily with an angular velocity Ω. The disc-tip velocity is $W{=}\Omega D/2$. In RH13 the discs are arranged in a square packing scheme, with discs which are adjacent in the streamwise direction spinning in opposite directions and discs along the spanwise direction rotating in the same direction. This configuration was chosen to resemble the standing wave studied by Viotti *et al.* (2009), and will henceforth be referred to as case 0. The layout for case 0 and the modified disc arrangements investigated herein are presented in Fig. 4.1. The coverage $\mathcal{C}$ is defined as the percentage of the wall surface which is in motion. For each arrangement, a coverage $\mathcal{C}_n$ is defined, with the subscript n referring to the layouts as numbered in Fig. 4.1. For the reference case studied by RH13 (case 0), $\mathcal{C}_0{=}78\%$. For case 5, the

arrangement is not the hexagonal lattice that gives maximum coverage for packing of equal circles (i.e. $\mathcal{C}$=91%). As the channel domain must be rectangular, it is not possible to configure the discs in this manner whilst maintaining an integer number of discs. The layout shown at the bottom right of Fig. 4.1 is instead simulated. The coverage for this arrangement is $\mathcal{C}_5$=84% and an integer number of discs is enforced. The spanwise length of the domain for case 5 is L_z=2.11π for D=3.38 and L_z=3.17π for D=5.02, due to the hexagonal disc arrangement. As stated in §3, the dimensions of the periodic box are larger than those used in current literature at similar Reynolds number (e.g. Kim *et al.*, 1987; Quadrio & Ricco, 2003). The increased streamwise extent of the channel compared with Kim *et al.* (1987) is to allow for the elongation of the near-wall turbulent structures that occurs under drag-reduced conditions (Orlandi & Fatica, 1997).

The disc diameters and velocities studied are D=3.38 and 5.02, and W=0.13, 0.26, 0.39, and 0.52. These forcing parameters are the ones that guarantee a high drag reduction of about 20% in the configuration studied by RH13. The term column is used to indicate disc alignment along the streamwise direction and the term row is used to denote disc alignment along the spanwise direction.

4.2 Effect of annular gap on performance quantities

Again as in RH13 and the previous chapter, a small annular region of thickness c is simulated around each disc. The wall velocity in this region decays linearly from the maximum at the disc tip to zero at the stationary wall and is independent from the azimuthal direction. The azimuthal velocity u_θ varies with the radial coordinate r as follows:

$$u_\theta(r) = \begin{cases} 2Wr/D, & r \leq D/2, \\ W(c - r + D/2)/c, & D/2 \leq r \leq D/2 + c. \end{cases}$$

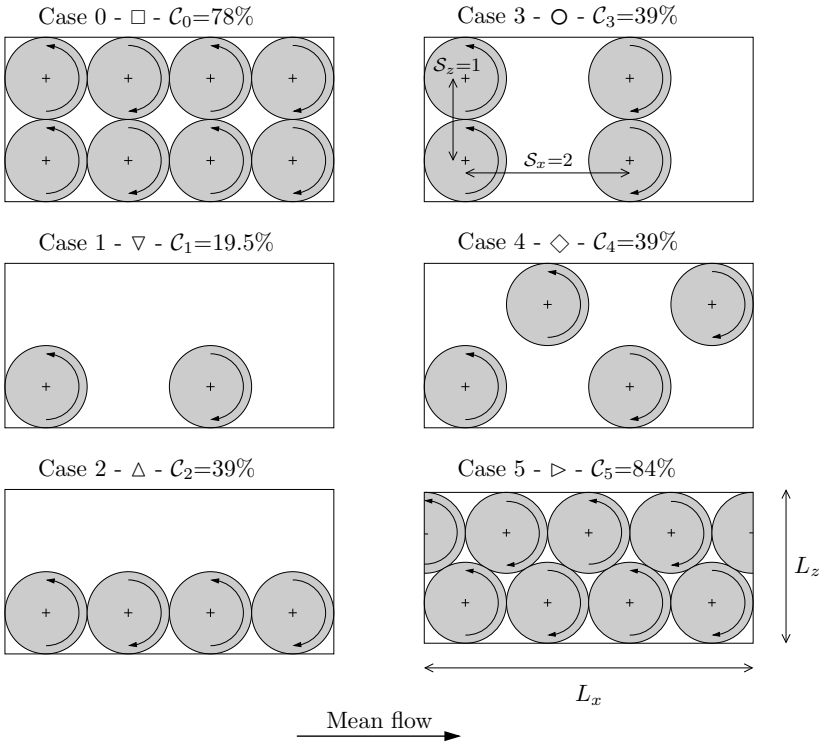

Fig. 4.1: Disc layouts in the wall x-z plane.

This serves to mimic an experimental scenario where a gap would inevitably be present. As shown by RH13, the Gibbs phenomenon at the disc edges is also almost entirely suppressed. It would be significant if the gap were not simulated because of the velocity discontinuity at the boundary between the disc tip and stationary wall. The effect of gap size on the performance quantities for D_0=3.56 and W=0.39 is shown in Fig. 4.2, where D_0=D+2c is the outer diameter of the circle occupied by the disc and the annular gap. Although the Gibbs phenomenon does occur for c=0, it does not influence the computation of drag reduction as the effect is limited to the disc edge. The drag reduction decreases by about 1% as c increases from 0 to $0.08D_0$. It then decreases more rapidly and, by c=$0.12D_0$, $\mathcal{R}$ is 70% of the value obtained without the annular gap. The power spent decreases almost linearly and more rapidly than $\mathcal{R}$ as the gap size increases. The averaged wall-shear stress therefore responds primarily to the large scales of

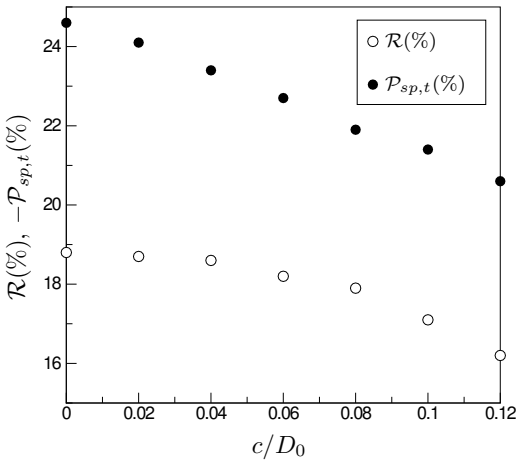

Fig. 4.2: Drag reduction $\mathcal{R}$ and power spent $\mathcal{P}_{sp,t}$ vs. c/D_0 for D_0=3.56 and W=0.39.

the disc forcing, while the power spent shows a more marked dependence on the precise distribution of wall actuation. More evidence of this emerges in §5.3 where the dependence of these quantities on the spectral representation of wall forcing is investigated. The gap size in the following cases is c=0.06D_0, which would most closely resemble the clearance in a water channel or in a wind tunnel set up.

The drag reduction computed in RH13 for D=3.38, W=0.39, and c/D_0=0.05 is $\mathcal{R}$=19.5%, which is larger than the corresponding value estimated from the data in Fig. 4.2, $\mathcal{R}$=18.5%. This discrepancy is larger than the uncertainty range of the numerical calculations. The difference between the C_f in the actuated-wall case in RH13 (C_f=6.64·10^{-3}) and the C_f computed here for c/D_0=0.06 (C_f=6.68·10^{-3}) leads to only a 0.4% difference in $\mathcal{R}$ if the stationary-wall C_f computed by RH13 is used as reference case (C_f=8.25·10^{-3}). More accurate resolution checks on the stationary-wall C_f lead to C_f=8.19·10^{-3}, which explains the 1% difference in $\mathcal{R}$.

4.3 Influence of layout and coverage on performance quantities

4.3.1 Drag reduction

The drag reduction $\mathcal{R}$ is shown in Figs. 4.3 and 4.4 as a function of the coverage $\mathcal{C}$ for D=3.38 and different W. The numerical values are found in Appendix C. The different symbols denote the different arrangements and the different colours indicate different W. The solid lines in Fig. 4.3 represent the drag reduction predicted through $\mathcal{R}=(\mathcal{C}/\mathcal{C}_0)\mathcal{R}_0$, i.e. via straight lines passing through the origin and the $\mathcal{R}_0$ values by RH13. These are not interpolating lines of the drag reduction data. $\mathcal{R}$ values falling on these lines obey linear scaling with coverage. For cases with W=0.13, shown by the white symbols, $\mathcal{R}$ scales linearly with $\mathcal{C}$. This implies that the drag reduction is only produced by the shearing effect of the flow over the disc surface. The hexagonal arrangement (case 5), which gives the maximum wall coverage $\mathcal{C}_5$=84%, also follows the linear scaling with $\mathcal{C}$. The scaling starts to deteriorate for some of the cases with W=0.26 and 0.39 (light and dark grey symbols), and is completely lost for W=0.52 (bold white symbols). A different physical mechanism must be responsible for drag reduction for the cases which do not follow the linear scaling with coverage. Except for case 5 and W=0.39, in all the cases that do not fall on the straight lines, $\mathcal{R}$ is larger than the corresponding value predicted by the coverage scaling. The drag reduction for case 0 and W=0.52 ($\mathcal{R}$=11.9%) is lower than the one given by cases 3 and 4 for the same W and D ($\mathcal{R}$=15.5%) despite the removal of half of the discs.

For cases with $\mathcal{C}_1$=19.5%, in which the surface is covered by a fourth of the number of discs used by RH13, the additional drag reduction with respect to coverage increases monotonically with W. Although cases 2, 3, and 4 all have the same coverage, $\mathcal{C}$=39%, the drag reduction values differ for the same W and D because they have different disc arrangements. Case 2, for which discs are

aligned in one column (upward facing triangles), obeys coverage scaling up to W=0.39. Case 3, for which discs aligned along every other row (circles), and case 4, which has a checkerboard disc arrangement (diamonds), instead lose this scaling for $W \geq$0.26. At the same W, the $\mathcal{R}$ values of cases 2 and 3 only differ by small amounts, which are within the uncertainty range for all the W tested. For $0.26 \leq W \leq 0.39$, it follows that the additional drag reduction with respect to the value predicted by the linear scaling with coverage occurs when a portion of stationary wall of the streamwise extent of one diameter is present between discs. The spanwise space between discs does not have an effect because case 3 (discs next to each other along z) and case 4 (spanwise space at either side of discs) lead to the same drag reduction.

The case of hexagonal arrangement, $\mathcal{C}_5$=84%, presents drag reduction values which are shifted below the coverage line for W=0.39. This is consistent with the upward shift of cases which present a streamwise region of stationary wall. In the hexagonal arrangement the streamwise spacing between discs is instead reduced and therefore drag reduction deteriorates with respect to the coverage line.

The drag reduction given by case 2 (discs aligned in one column) loses the linear scaling only at W=0.52, even though no streamwise spacing is present. An upward shift with respect to the coverage line also occurs for case 5 at W=0.52. Similarly to the upward shift of case 2 at the same W, this is not due to the streamwise fixed-wall space as in cases 1, 3, and 4 because discs are closely packed along the streamwise direction. It is neither due to the spanwise space of fixed wall at the side of each disc because the additional drag reduction is the same in cases 2 and 5, although case 2 displays more spanwise space than case 5. The drag reduction at W=0.52 being higher than the value predicted by the linear scaling with coverage remains unexplained at this point.

By defining a new quantity, $\mathcal{E}=\mathcal{R}/\mathcal{C}$, the coverage gain of the disc actuators

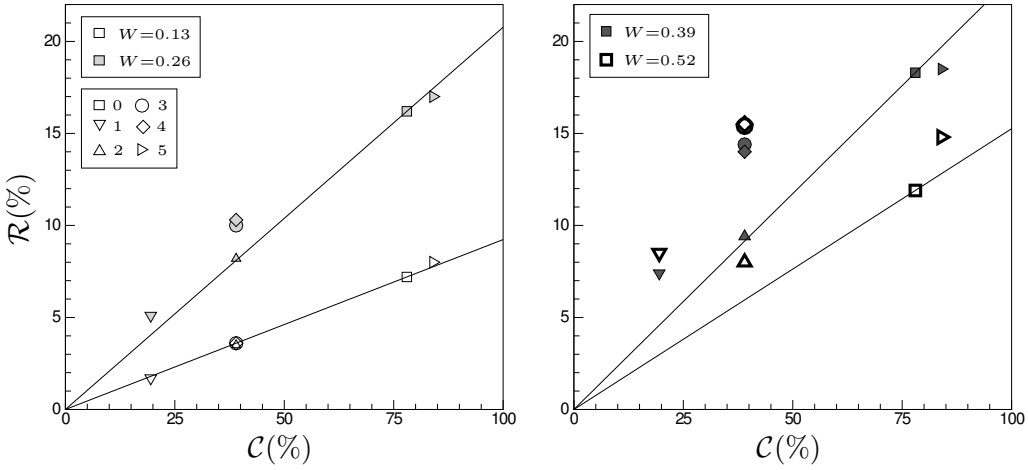

Fig. 4.3: Drag reduction vs. coverage for D=3.38. In the legend, the symbols are numbered according to the layouts in Fig. 4.1 and are coloured according to W.

is given as the drag reduction induced per actuated area. For cases in which $\mathcal{E}>\mathcal{E}_0$, where $\mathcal{E}_0=\mathcal{R}_0/\mathcal{C}_0$ is the coverage gain for case 0, larger drag reduction occurs compared to case 0 for the same number of discs. Fig. 4.4 presents $\mathcal{E}/\mathcal{E}_0$ as a function of $\mathcal{C}$. In this scaling, it emerges that the gain is null at W=0.13, independent of $\mathcal{C}$ when W=0.26 for cases that do not follow coverage, and at its maximum at low coverage and high W.

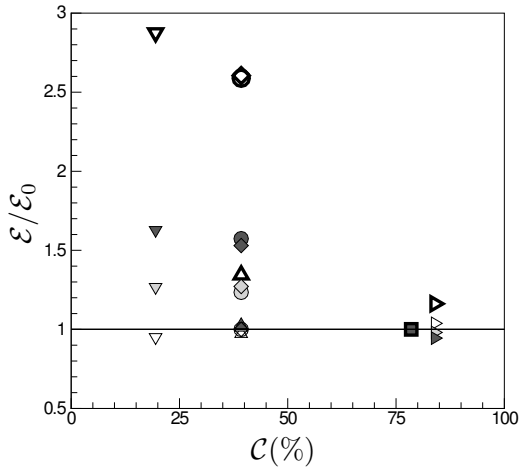

Fig. 4.4: Drag reduction gain $\mathcal{E}/\mathcal{E}_0$ vs. coverage for D=3.38. Symbols are as in Fig. 4.1 and coloured according to the legends shown in Fig. 4.3.

For the cases examined heretofore, the displacement between adjacent streamwise and spanwise disc centres has been either D_0 or $2D_0$. More arrangements of discs can be studied by defining the spacings $\mathcal{S}_x$=x_d/D_0 and $\mathcal{S}_z$=z_d/D_0, where x_d and z_d are the distances between neighbouring disc centres in the x and z directions, respectively. $\mathcal{S}_x$ and $\mathcal{S}_z$ are shown graphically in case 3 in Fig. 4.1. Fig. 4.5 (left) shows $\mathcal{R}$ for different $\mathcal{S}_x$ and $\mathcal{S}_z$ with disc parameters D=3.38, W=0.52. An optimum spacing is found for $(\mathcal{S}_x, \mathcal{S}_z)$=(1.5,1) resulting in $\mathcal{R}$=17%. For comparison the RH13 value (case 0) is $\mathcal{R}$=12% for the same disc parameters.

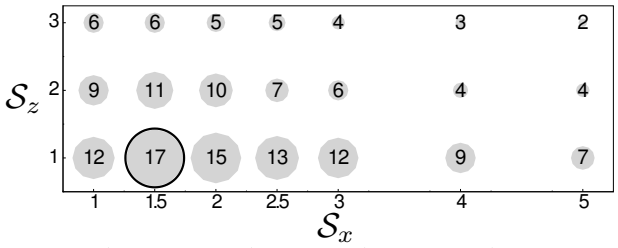

Case	D	W	$\mathcal{R}_{sw}$(%)	$\mathcal{R}_{pred}$(%)	$\mathcal{R}$(%)
0	3.38	0.26	33	16.4	16.2
2	3.38	0.26	33	8.2	8.2
5	3.38	0.13	16	8.6	8.7

Fig. 4.5: Top: Map of $\mathcal{R}(\mathcal{S}_x, \mathcal{S}_z)$(%) for D=3.38, W=0.52. Bottom: Comparison of drag reduction data from the DNS with those given from rescaling of Viotti *et al.* (2009).

As $\mathcal{R}$ scales with coverage at low W, a prediction of the drag reduction engendered by the discs is attempted, starting from the data computed in Viotti *et al.* (2009) (page 10) for the standing-wave case. As noted by RH13, the wall forcing created along the disc centres is similar to a triangular wave of wavelength λ_x=$2D_0$ and amplitude W. The drag reduction given by the discs can be predicted as $\mathcal{R}_{pred}$=$C_w \cdot C_\theta \cdot \mathcal{C} \cdot \mathcal{R}_{sw}$, where C_w is the scaling factor due to waveform, C_θ models the effect of the orientation of wall forcing, $\mathcal{C}$ accounts for

the wall coverage, and $\mathcal{R}_{sw}$ is the drag reduction in the standing-wave case by Viotti *et al.* (2009) for λ_x=$2D_0$. The factors are approximated as follows.

Waveform It is known that temporal and spatial forcing can be largely treated as analogous to one another (Quadrio *et al.*, 2009). The temporal non-sinusoidal spanwise wall-forcing investigated by Cimarelli *et al.* (2013) can thus be used to gauge the influence of the spatially non-sinusoidal spanwise wall-forcing of the discs. Waveform *j* on page 4 of Cimarelli *et al.* (2013) closely resembles the triangular wave spanwise forcing of the discs, which results in C_w=85%.

Streamwise forcing The streamwise forcing which is present in the disc technique does not occur in the standing-wave case studied by Viotti *et al.* (2009). The effect of wall oscillations at an angle θ with respect to the mean flow has been studied by Zhou & Ball (2008). While pure spanwise oscillations produce the maximum drag reduction, the response to streamwise oscillations reduces to a third. The influence of wall-forcing orientation is accounted for by C_θ=75%, estimated by averaging Zhou & Ball's data over the angle of wall forcing.

Coverage This is quantified by the coverage value $\mathcal{C}_n$ for each case, given in Fig. 4.1.

The table in Fig. 4.5 (right) shows the $\mathcal{R}$ values for three sample layouts and disc parameter combinations. The prediction $\mathcal{R}_{pred}$ of the numerically computed $\mathcal{R}$ is excellent for the cases tested.

4.3.2 Power spent

The effect of coverage is now studied on the power spent, shown as a function of $\mathcal{C}$ in Fig. 4.6. The numerical values are found in Appendix C. For all W the

linear scaling of power spent with coverage is excellent and much more robust than for drag reduction, shown in Fig. 4.3. The power spent therefore does not depend on the disc arrangements for fixed $\mathcal{C}$. This follows from the power spent being solely related to the wall motion and largely independent of the dynamics of turbulence within the channel. The solid lines represent the laminar prediction to the power spent $\mathcal{P}_{sp,l}$, calculated from the solution to the flow induced by an infinite disc rotating beneath a quiescent fluid (Batchelor, 1967). An amended and improved version of the formula in RH13, which now takes into account the effect of the gap flow, is used. This reads

$$\mathcal{P}_{sp,l}(\%) = 100\frac{\mathcal{C}}{\mathcal{C}_0}\frac{\pi G_k R_p^{3/2} W^{5/2}}{U_b R_\tau^2 D_0^2}\sqrt{\frac{2}{D}}\left(\frac{D^2}{8}+\frac{cD}{3}+\frac{c^2}{6}\right), \tag{4.1}$$

where G_k=−0.61592 is given in Schlichting (1979), and R_p and R_τ are the Poiseuille and friction Reynolds numbers respectively, defined in Sec. 3.1. Equation (4.1) predicts $\mathcal{P}_{sp,t}$ well, with the turbulent $\mathcal{P}_{sp,t}$ being always slightly larger than the laminar $\mathcal{P}_{sp,l}$.

4.4 The Fukagata-Iwamoto-Kasagi identity

In this section, the FIK identity (Fukagata *et al.*, 2002) is used to further understand the mechanism of drag reduction for the disc arrangements studied in §4.3. This identity quantifies the effect of the laminar flow and of the Reynolds stresses to the skin-friction coefficient. RH13 and Wise & Ricco (2014) (henceforth referred to as WR14) showed that through this identity it is possible to distinguish two separate contributions to drag reduction, which arise from (a) the modification in the turbulent Reynolds stresses relative to the uncontrolled case, and from (b) the Reynolds stresses $\widehat{u_d v_d}$, related to the structures appearing between discs and described in RH13 on page 13 and in WR14 on pages 557-558. The drag reduction is written as $\mathcal{R}$=$\mathcal{R}_t$+$\mathcal{R}_d$, where $\mathcal{R}_t$ synthesizes effect (a) and

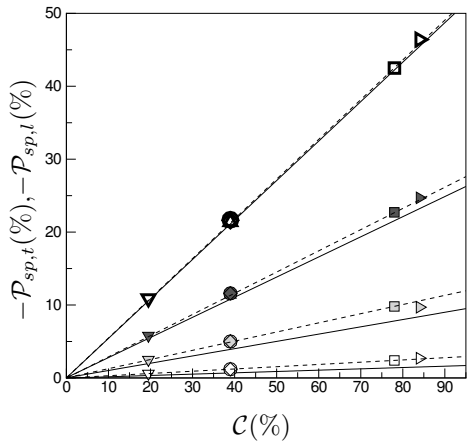

Fig. 4.6: Power spent vs. coverage for D=3.38. The different symbols correspond to the different layouts as indicated in Fig. 4.1 and are coloured according W, as shown in the legend of Fig. 4.3. The solid lines represent the prediction of power spent by the laminar solution given by (4.1). The dashed lines are found by rescaling the RH13 $\mathcal{P}_{sp,t}$ values with respect to coverage, i.e. they connect the origin and the RH13 values (square symbols).

$\mathcal{R}_d$ is related to (b). Their expressions are:

$$\mathcal{R}_t(\%) = 100\frac{R_p\left[(1-y)\left(\widehat{u_t v_t} - \langle\widehat{u_{t,s}v_{t,s}}\rangle\right)\right]_g}{U_b - R_p\left[(1-y)\langle\widehat{u_{t,s}v_{t,s}}\rangle\right]_g},$$

$$\mathcal{R}_d(\%) = 100\frac{R_p\left[(1-y)\,\widehat{u_d v_d}\right]_g}{U_b - R_p\left[(1-y)\langle\widehat{u_{t,s}v_{t,s}}\rangle\right]_g}.$$

Fig. 4.7 shows $\mathcal{R}_t$ and $\mathcal{R}_d$ (light and dark grey respectively) for each layout and different W for D=3.38. For case 0 the contribution from $\mathcal{R}_t$ increases from 7% at W=0.13 to 13% at W=0.26 and 0.39. It decays to 6% for W=0.52. In the oscillating case studied by WR14, $\mathcal{R}_t$ scales linearly with the disc boundary layer thickness δ, defined in RH13 and WR14 as a measure of the viscous diffusion from the disc surface. Using data from RH13, $\mathcal{R}_t$ also scales linearly with δ for steady rotation. Furthermore, $\mathcal{R}_t$ scales with coverage for W=0.13 for all layouts. The contribution to the overall drag reduction from $\mathcal{R}_d$ is negligible for cases 1 and 2 at all W, for which there is no spanwise interaction between the discs, and for all cases at W=0.13. The impact of the interdisc structures on drag reduction,

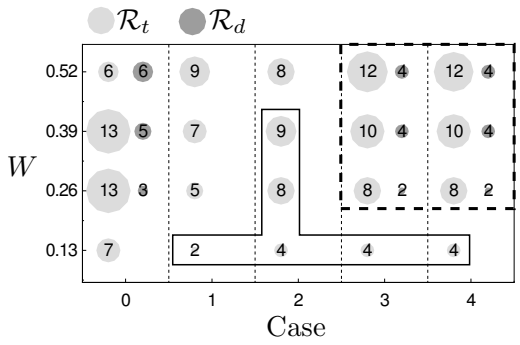

Fig. 4.7: Percentage contributions of $\mathcal{R}_t$ and $\mathcal{R}_d$ to $\mathcal{R}$ for D=3.38. $\mathcal{R}_t$ represents the contribution from the modification of the turbulent Reynolds stresses (light grey), and $\mathcal{R}_d$ is the contribution from the interdisc structures (dark grey). Cases boxed by the solid line obey linear scaling with $\mathcal{C}$, while cases boxed by the dashed line are influenced by the interdisc structures. Case 0 is not boxed because it is the reference case against which the other cases are compared.

synthesized by $\mathcal{R}_d$, becomes important for cases 3 and 4, whose $\mathcal{R}_t$ and $\mathcal{R}_d$ values are the same for the same W.

The cases for which $\mathcal{R}_d$ attains a finite value are boxed by the dashed line. Spanwise interaction between the discs must therefore be important for the formation of these structures, although at this stage it is still not clear why cases 3 and 4 have the same $\mathcal{R}_t$ and $\mathcal{R}_d$ values despite the shift of columns. For the cases boxed by the solid line, coverage scaling applies and structures do not appear, although in RH13 for W=0.26 and 0.39 the structures do contribute to the overall drag reduction.

4.5 Flow visualizations

The contribution of $\mathcal{R}_d$ in cases 3 and 4 is proved to be important through the use of the FIK identity. Therefore, we resort to flow visualizations to display the interdisc structures that are responsible for $\mathcal{R}_d$. Isosurfaces of q=$\sqrt{u_d^2 + v_d^2 + w_d^2}$=0.08 are shown in Fig. 4.8 for cases 3 and 4, the white arrows indicating the direction

of disc rotation. In both cases the disc boundary layers are clearly visible. The plots show the presence of the tubular structures first shown in RH13, elongated in the streamwise direction and situated between adjacent discs in the spanwise direction. For cases 1 and 2, the structures are instead not evident for similar values of q. The only instances where the structures are clearly visible occurs when there is spanwise interaction between the discs. This happens only for $W \geq 0.26$ and for cases 0, 3, and 4, where the distance between the nearest disc centres is smaller than or equal to $\sqrt{2}D_0$.

A contour of $u_d v_d$ for case 3 at y^+=14 is shown in Fig. 4.9, indicating the disc side where the structure is created. The contour for case 4 is nearly identical. Differently from the experimental study by Klewicki & Hill (2003) of the laminar flow over a finite rotating surface patch, structures are not visible over both sides of the disc. They do however propagate downstream parallel to the mean flow as the structures observed by Klewicki & Hill. Fig. 4.9 shows that in all cases where there is a contribution from $\mathcal{R}_d$, the structures originate from the disc side where the wall forcing is along the upstream direction. When only one disc is included in the domain, the structures do not appear. Therefore the structures are created: i) when there is sufficient spanwise interaction between discs, i.e. $W \geq 0.26$ and the distance between disc centres located in adjacent columns is smaller than or equal to $\sqrt{2}D_0$, and ii) at the disc sides where the wall streamwise motion is in the opposite direction to the mean flow.

4.6 Radial streaming

The FIK identity and flow visualizations of the structures have been useful to shed further light on the formation of the interdisc structures, but have not helped to explain the extra drag reduction effect with respect to coverage, discussed in §4.3. To gain more insight, since streamwise fixed-wall space is a common feature of

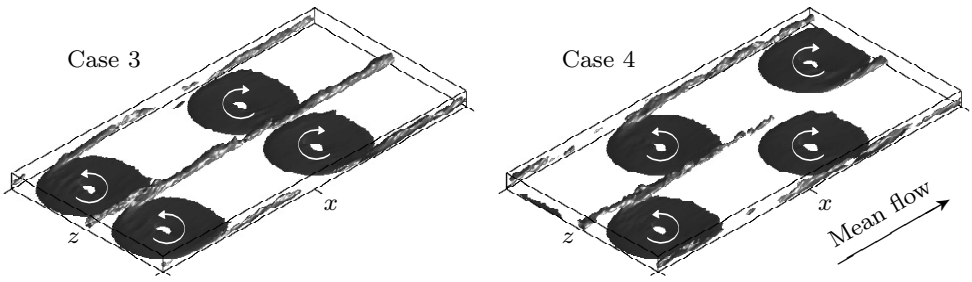

Fig. 4.8: Isosurfaces of $q=\sqrt{u_d^2+v_d^2+w_d^2}$=0.08 for case 3 (left) and case 4 (right), and D=3.38, W=0.52.

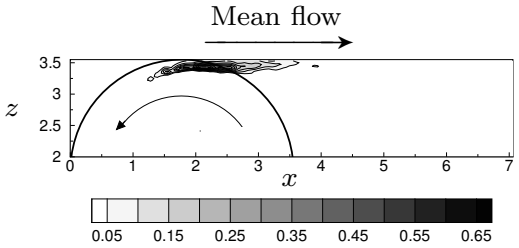

Fig. 4.9: Contour of $u_d v_d$ at y^+=14 for D=3.38, W=0.52, and case 3.

the cases which present the additional drag reduction, the flow between discs is studied. The streamwise development of $\mathcal{R}$ along the disc centreline in case 3 is shown in Fig. 4.10 by the solid line. The drag reduction is non-zero at the disc centre and asymmetric about this point. A local peak of maximum drag reduction of 95% occurs in the upstream disc region and intense drag increase appears in the downstream disc region. Between discs there is a region of about $\mathcal{R}$=20% that is responsible for the additional drag reduction with respect to coverage. This region must be created through the interaction between the mean flow and the disc flow because the net disc-flow wall-shear stress would be null if u_m=0, i.e. if the streamwise pressure gradient were absent, owing to the disc-flow symmetry.

By use of the laminar solution, the skin-friction coefficient is predicted as follows:

$$C_{f,l}(x) = \frac{2}{U_b^2 R_p}\left[u_m'(0) + F_k\left(\frac{2W}{D}\right)^{3/2} R_p^{1/2} x\right], \tag{4.2}$$

where F_k=0.51 is given in Schlichting (1979). This prediction is not rigorous as

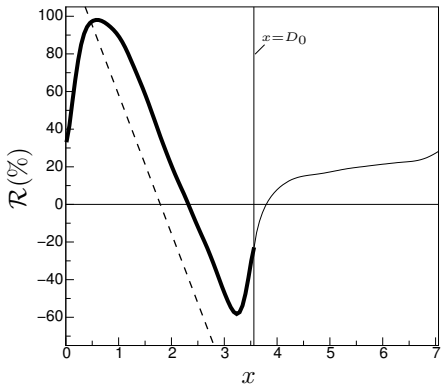

Fig. 4.10: Streamwise development of $\mathcal{R}$ along the disc centreline for case 3 for W=0.52. The thick line indicates the profile for the flow over the disc surface and the dashed line represents the drag reduction predicted by the laminar solution (4.2).

the interaction between the mean and disc flow is not considered and end effects are neglected. Despite this, as shown in Fig. 4.10, the gradient of $\mathcal{R}$ with respect to x is well predicted on the disc surface, although the drag reduction computed via the laminar solution is higher than 100% due to flow reversal as the disc edge is not modelled. The DNS trend of $\mathcal{R}$ is shifted along x by about $45\nu^*/u_\tau^*$ relatively to the laminar prediction. This is consistent with the streamwise shift in the disc flow of about $100\nu^*/u_\tau^*$ observed at y^+=8 in the oscillating-disc case by WR14. This shift must be due to the interaction between the mean and disc flows, which is not considered in the laminar analysis.

To further investigate the flow above the fixed-wall region between discs, the downstream development of u_d along the centreline of the discs, shown in Fig. 4.11 (left), is studied. The profiles are separated by $40\nu^*/u_\tau^*$ and those on the disc surface are indicated by the grey bars. From the beginning of the domain and up to about the disc centre, the disc creates a radial flow along the negative x direction which retards the streamwise flow, thereby causing drag reduction. From the centre of the disc and up to the downstream disc tip, the radial flow

enhances the streamwise flow, resulting in drag increase. The radial flow is most energetic near the disc tips and this is represented by the peaks of drag reduction and drag increase in Fig. 4.10. The streamwise shift in the disc flow is also evident in Fig. 4.11 (left), shown by the switch from negative to positive u_d occurring between points C and D at a distance of about $80\nu^*/u_\tau^*$ downstream of the disc centre.

The disc flow persists further in the upstream direction than it does downstream, which explains the region of drag reduction above the fixed wall in Fig. 4.10. The disc flow upstream of a disc persists for $480\nu^*/u_\tau^*$ from the upstream disc tip (point B), whereas the disc flow along the positive x direction vanishes within a distance of only $120\nu^*/u_\tau^*$ downstream of the disc tip (point D). In Fig. 4.11 (left) the peak of the u_d profile varies above the disc, whereas in the laminar solution this location is invariant. The difference must be accounted for by the interaction of the disc flow with the mean streamwise flow. Immediately off the disc surface the peak y-location of the disc flow increases by Δy=0.015. As the wallward flow above the disc caused by the von Kármán pumping effect does not occur above the fixed wall, the radial flow is allowed to diffuse further into the channel.

Fig. 4.11 (right) presents the radial flow u_r as a function of y for two locations on the disc surface. A graphical definition of u_r is provided in Fig. 4.11 (inset). The thick solid line is the radial flow above the disc at x=2.72, z=1.36, displaced by r=1.04 from the disc centre. The dashed line is the laminar prediction for the disc flow at the same r. It is evident that at the same location the laminar and turbulent flow profiles do not coincide. The thin solid line indicates the turbulent disc flow at a location $100\nu^*/u_\tau^*$ downstream of the laminar prediction (x=3.27, z=1.36). At this location the turbulent and laminar profiles are almost identical for y<0.05, confirming the downstream shift of the disc flow.

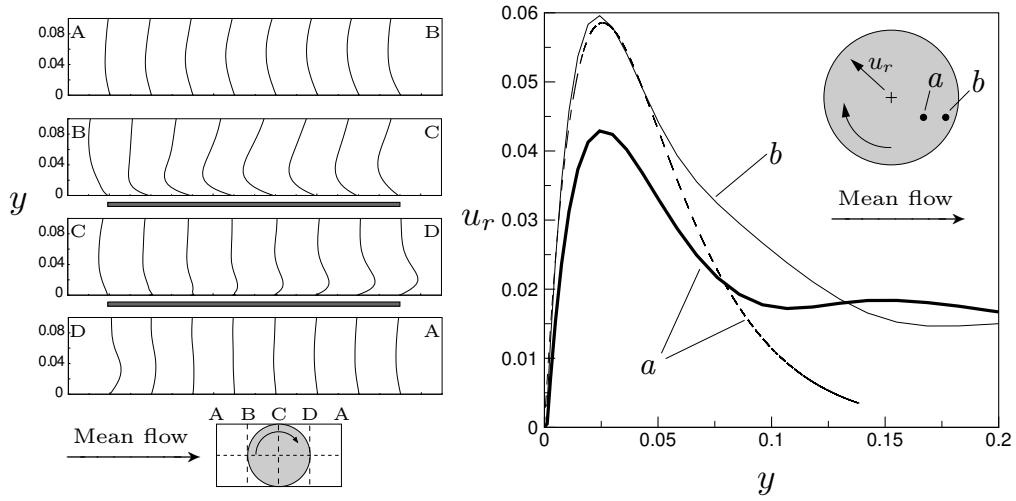

Fig. 4.11: Left: Streamwise disc flow u_d vs. y at different locations along the disc centreline for W=0.52. The letters A-D indicate which wall section the plot corresponds to. The plots above the grey bars correspond to locations on the disc surface. Right: Radial flow u_r vs. y for different locations on the disc surface. The solid lines represent turbulent profiles at locations a (thick line) and b (thin line), separated by $100\nu^*/u_\tau^*$. The dashed line denotes the laminar profile at the a location.

5. MODIFICATIONS TO CONTROL STRATEGY

5.1 Half-disc actuators

As evidenced in §4.6 by Fig. 4.10 the radial flow induced by the downstream half of the discs causes drag increase. To eliminate this effect, a half-disc configuration is studied, whereby the downstream disc half is covered and the wall-velocity is zero. The half-disc actuators are investigated for D=3.38,5.07 and W=0.13,0.26,0.39. The drag reduction data for the half-disc simulations (subscript h) are presented in the table in Fig. 5.1 (right) with the corresponding data for case 0 (subscript 0). As shown in Fig. 5.1 (left), the negative effect of the downstream radial flow is eliminated by covering this portion of the disc. The azimuthal flow, which contributes favourably to drag reduction, is also removed. As expected, the prediction of the laminar solution (dashed lines) is worse than in the full-disc case.

For both disc diameters and W=0.26, the drag reduction decreases when the downstream disc half is covered. This is because for low W the negative effect of the radial flow is less important than the benefit of the azimuthal forcing. For W>0.26 the drag reduction increases when the downstream disc half is covered and a maximum $\mathcal{R}_h$=25.6% is computed. For high W the removal of the downstream disc section and the associated radial flow therefore outweighs the loss of beneficial effects induced by the azimuthal flow.

Although the increased drag reduction from this configuration is an interesting result, our model contains many simplifications. In an experimental set up a

step would occur between the covered and uncovered halves of the disc, resulting in recirculation regions. Neither this nor any interaction between the mean flow and the disc housing is considered. A novel flow-control device has been realized experimentally by Koch & Kozulovic (2013) who performed boundary layer experiments on a disc set up with one spanwise half covered. Differently from our actuators this is a passive method as the disc motion is driven by the mean flow and there is no external power input. As the uncovered disc half rotates, the velocity difference between the mean flow and the wall decreases, thereby reducing the wall-shear stress while drawing energy from the mean flow.

A discussion must be included on the categorization of flow control methods as either drag reduction or pumping Hœpffner & Fukagata (2009). For the original disc actuators, studied by RH13 (case 0 in Fig. 4.1), although a mean flow is induced by the discs in the absence of streamwise pressure gradient, this mean flow is null when averaged along the streamwise direction. Therefore RH13's disc-flow control method can be categorized as drag reduction. For the half-disc technique, a net upstream mean flow is instead created in the absence of streamwise pressure gradient as an indirect response to the wall forcing, whose average in either the spanwise or streamwise direction is null. The half-disc method can thus be classified as indirect pumping. Direct pumping would instead occur if the reduction of wall friction were induced by a body force or a wall velocity distribution which are not zero when averaged along the streamwise direction.

5.2 Annular actuators

The laminar solution provides further direction for improvement of the disc-flow technique. The wallward flow produced by the von Kármán pump, which is uniform over the disc surface in planes parallel to the wall, can be expected to

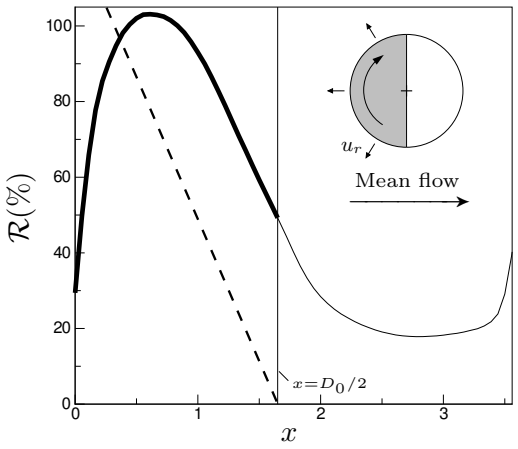

D=3.38

W	$\mathcal{R}_0(\%)$	$\mathcal{R}_h(\%)$
0.26	16.2	13.7
0.39	18.3	21.8
0.52	11.9	25.4

D=5.07

W	$\mathcal{R}_0(\%)$	$\mathcal{R}_h(\%)$
0.26	17.5	13.0
0.39	22.3	21.1
0.52	18.5	25.6

Fig. 5.1: Left: Streamwise development of $\mathcal{R}$ along the half-disc centreline for D=3.38, W=0.52. The thick line indicates the profiles for the flow over the actuated half disc surface. The dashed line indicates the drag reduction predicted from the laminar solution (4.2). Inset: Schematic of a half-disc actuator. Right: Performance data for half-disc simulations.

direct the streamwise flow towards the wall, causing a detrimental effect to drag reduction. Furthermore, the azimuthal forcing near the disc centre is of low velocity and, as shown in §4.2, the large-scale forcing appears to be important for drag reduction. Therefore, annular actuators are studied, with the intent of attenuating the wallward flow and eliminating the low velocity motion near the disc centre, which is thought to have a marginal contribution to drag reduction. The ratio of the internal and external radii, a=r_i/R, is varied from 0 to 1, and the drag reduction and power spent are shown as functions of a in Fig. 5.2. A schematic of the actuators is shown in Fig. 5.2 (inset).

The drag reduction remains approximately constant at $\mathcal{R}$=19% for a<0.375.

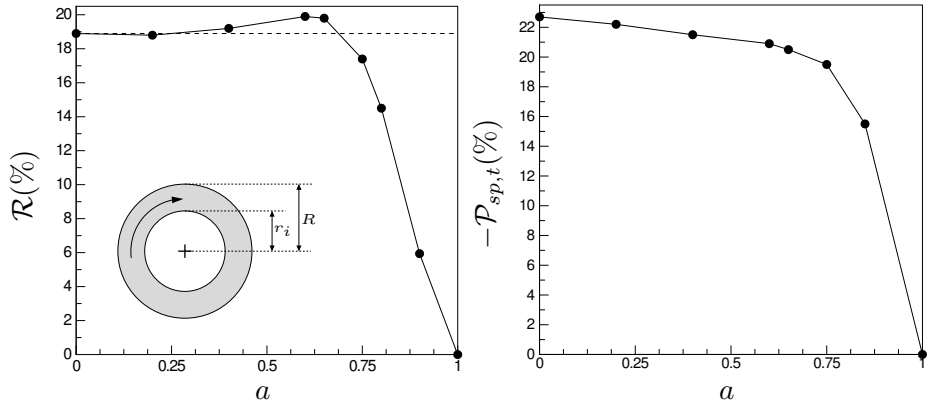

Fig. 5.2: Performance quantities vs. annulus ratio, $a{=}r_i/R$, for $D{=}3.38$ and $W{=}0.39$. Left: Drag reduction, $\mathcal{R}$. Right: Power spent, $\mathcal{P}_{sp,t}$. Inset: Schematic of an annular actuator.

An optimum of $\mathcal{R}{=}20\%$ is reached at $a{=}0.6$, beyond which the drag reduction decreases. This confirms the prediction that the flow induced near the disc centre has an overall negative effect on drag reduction. Beyond the optimum $a{=}0.6$ the removal of the central part of the disc causes a sharp decrease in $\mathcal{R}$ to a null value for $a{=}1$.

The power spent, shown in Fig. 5.2 (right), instead shows a slow monotonic decrease as a increases, up to $a{=}0.75$. Beyond $a{=}0.75$ there is a rapid decay in $\mathcal{P}_{sp,t}$ as more of the disc centre is removed. This can be explained as a vast proportion of the disc energy is contained in the outer region, i.e. where the wall velocity is high. The removal of the inner part of the disc thus does not largely affect the power spent, as it is the region of low wall-velocity that is being eliminated. For the tip-velocity investigated, the use of annular actuators does not lead to net power savings.

5.3 Spectral truncation

The investigation of annular actuators confirms that the large scale forcing is important for drag reduction. The spectral representation of the boundary con-

ditions is therefore examined to elucidate the effects of large and small scale forcing. By truncating the number of Fourier modes that describe the disc motion, it is possible to force only a specified range of scales. The proportion of modes forced in the homogeneous directions is given by $k(\%)=100k_{f,i}/N_i$, where $k_{f,i}$ is the maximum forced wavenumber, $\mathcal{N}_i$ is the total number of modes, and the i subscript denotes the streamwise or spanwise direction. The truncation of modes is symmetrical in each direction, and so $k=100k_x/\mathcal{N}_x=100k_z/\mathcal{N}_z$. The drag reduction and power spent are plotted as functions of k in Fig. 5.3 (left). As the number of forced modes increases, both $\mathcal{R}$ and $\mathcal{P}_{sp,t}$ asymptotically approach the values given when all of the modes are included. The drag reduction reaches the asymptotic value only when k=8%, while $\mathcal{P}_{sp,t}$ reaches the asymptote when k=47%. The contour plots of azimuthal wall velocity for these truncations are shown in Fig. 5.3 (insets). Fig. 5.3 (right) displays the energy contained within the streamwise modes. A large proportion of the energy is contained within the low wavenumber modes. The energy of the wall streamwise velocity has a peak value at k_x=2, then drops monotonically with k_x up to about $k_x = 50$, at which it attains small values comprised between 10^{-5} and 10^{-6}. The energy of the wall spanwise velocity has peaks of amplitude decreasing continuously by more than one order of magnitude and occurring at k_x=2, 14 and 82. These peaks are separated by minima at k_x=6 and 54 of magnitude 10^{-2} and 10^{-5}, respectively.

The results in Fig. 5.3 (left) bear analogy with the effects of gap size and annular actuators on the performance quantities, presented in §4.2 and 5.2, respectively. In all cases it is evident that the large scale forcing is most responsible for the drag reduction, shown by the lack of significant change in $\mathcal{R}$ when high-wavenumber modes are eliminated from the disc spectral representation, the gap size is increased, or the central part of the disc is removed. This is significant as it means that low-order models, which only capture prescribed features of the

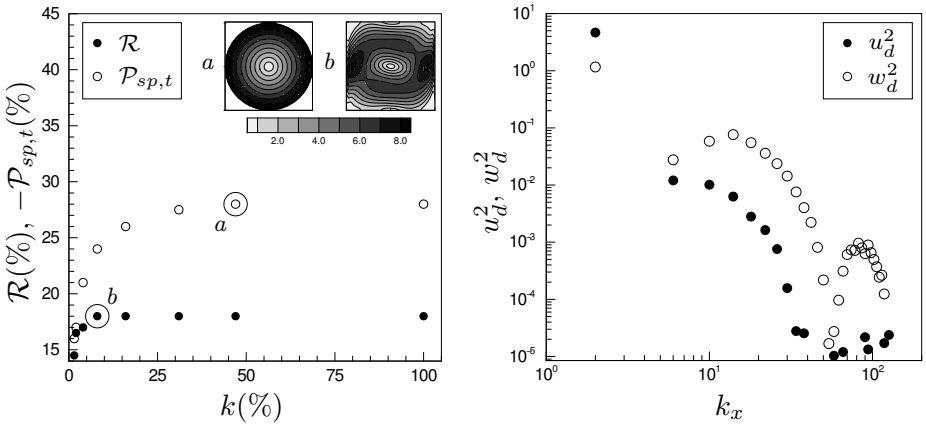

Fig. 5.3: Left: Effect of spectral truncation on performance quantities. $\mathcal{R}$ and $\mathcal{P}_{sp,t}$ vs. k, the proportion of modes synthesizing the wall boundary conditions. Inset: Contours of $q{=}\sqrt{u_d^2+w_d^2}$ at $y{=}0$ for the circled cases for $k{=}47\%$ (left) and $k{=}8\%$ (right). Right: Energy of streamwise and spanwise forcing, measured by u_d^2 and w_d^2, vs. the streamwise wavenumber k_x.

turbulence dynamics, might be sufficient for computing accurate values of drag reduction. The boundary conditions have also been modified to only force either the spanwise or streamwise wall velocity. Drag increase occurred in both cases. This shows that a fully nonlinear mechanism must be responsible for drag reduction.

5.4 Freely-rotating discs

In this section unactuated discs are positioned on the channel walls. The discs rotate freely according to the torques which act upon them. Therefore the angular velocity of each disc is proportional to the turbulent shear on its surface. There is an analogy here to superhydrophobic surfaces. For such surfaces a slip velocity u_s is defined, related to the shear at the wall through a slip-length L_s. A spatial representation for wall-velocity is thus given by $u_{s,i}{=}L_{s,i}\,\partial u_i/\partial y|_{wall}$ where $u_{s,i}$ and $L_{s,i}$ are the wall-velocity and the slip length in the i-th directions,

respectively.

Passive discs have been experimentally investigated by Koch & Kozulovic (2013). In this work an unactuated wall-mounted disc is contained within a housing which allows one spanwise half of the disc to be exposed to the flow. The uncovered half of the disc is driven by the mean flow, causing the disc to rotate. This thereby reduces the velocity difference between the mean flow and the wall, over the unconvered half of the disc. This in turn reduces the wall-shear stress. A separate passive control method is herein investigated whereby discs rotate independently, driven by the distribution of the turbulent shear stress.

Discs of mass m^* and diameter D^* are flush-mounted on the channel walls in a square-packing array as in chapter 3, and allowed to rotate independently of one other. Each disc moves according to the angular equation of motion

$$I^*\ddot{\theta}^* = \Sigma\mathcal{T}^*, \tag{5.1}$$

where $I^*{=}m^*D^{*2}/8$ is the moment of inertia of the disc, $\ddot{\theta}^*$ is its angular acceleration, and $\Sigma\mathcal{T}^*$ is the sum of torques acting upon the disc. In order to accurately describe the disc motion the following torques are considered: *a)* the fluid torque $\mathcal{T}_t$ coming from the turbulent wall-shear stress acting on the disc surface, *b)* the friction opposing the disc motion coming from the fluid contained within the disc housing $\mathcal{F}_f$, and *c)* the mechanical friction $\mathcal{F}_m$ present in such a bearing as would be used to mount the device. Although $\mathcal{T}_t$ can be computed from the DNS, $\mathcal{F}_f$ and $\mathcal{F}_t$ must be modelled. Equation (5.1) can thus be written as

$$\mathcal{T}_t - \mathcal{F}_f - \mathcal{F}_m = I\ddot{\theta}, \tag{5.2}$$

where a schematic of the disc and torques acting upon it is presented in figure 5.4. The turbulent torque $\mathcal{T}^*{}_t$ is computed directly from the flow field for each disc according to

$$\mathcal{T}_t^* = \frac{1}{\mu^*}\int_0^{D^*/2}\int_0^{2\pi} r^{*2}\tau_\theta^*\mathrm{d}\theta\mathrm{d}r^*,$$

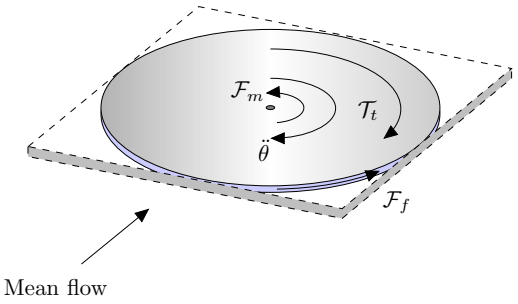

Fig. 5.4: Schematic of the torques acting on each disc

where $\tau^*_\theta = \partial u^*_\theta / \partial y^*|_{wall}$, and the coordinate system is the same as that shown in figure 3.2. The frictional torque arising from the fluid contained within the disc housing is estimated using the laminar von Kármán solution, outlined in Schlichting (1979). This model implies that the gap which would inevitably occur between the disc and the housing beneath is sufficiently thin for the laminar assumption to be valid. The torque on a disc rotating beneath a quiescent fluid is given by Schlichting (1979) as

$$\mathcal{F}^*_f = \frac{\nu^{*1/2} G_k \pi \rho^* D^{*4} \left|\dot{\theta}^*\right|^{3/2}}{32}.$$

Finally the mechanical friction $\mathcal{F}^*_m$ within the disc bearing is estimated. Only rolling friction is considered. As such the friction is modelled as a fixed proportion of the external torques acting on the disc. This proportion is constant and independent of angular velocity. A proportional constant of f=0.0015 is chosen, where $\mathcal{F}^*_m = -f(\mathcal{T}^*_t - \mathcal{F}^*_f)$. This is equivalent to the upper bound for rolling friction in ball bearings (Brändlein *et al.*, 1999). A detailed derivation of the equation of motion for the freely-rotating discs is presented in Appendix D. Scaled in outer units the equation of motion for the discs is

$$I\ddot{\theta} = (1-f)\left[\frac{1}{R_p}\int_0^{D^*/2}\int_0^{2\pi} r^2 \frac{\partial u_\theta}{\partial y} \mathrm{d}\theta \mathrm{d}r - \kappa\left|\theta\right|^{3/2}\right], \tag{5.3}$$

where $I = a\pi D^4 b/32$, and $\kappa = \mathrm{sgn}(\theta) G_k \pi D^4/(32 R_p^{1/2})$. The $\mathrm{sgn}(\theta)$ term is introduced here to ensure that the fluid friction is always acting to retard the disc

motion.

The DNS code was modified extensively to implement the freely-rotating disc boundary conditions. A brief description of the algorithm to update the disc velocities is presented herein. Each time the flow field is advanced in time the turbulent torque $\mathcal{T}_t$ acting on each disc is calculated for the present time step, i.e. step n. The predicted angular velocities of the discs at the next time step are then calculated explicitly according to

$$\dot{\theta}_{n+1} = \dot{\theta}_n + \frac{(1-f)\Delta t}{I}\left(\mathcal{T}_{t,n} - \kappa\left|\dot{\theta}_n\right|^{3/2}\right),$$

where the subscripts n and $n+1$ refer to the current and proceeding time steps, respectively. The map of the wall-velocity components is computed from the disc angular velocities, before being Fourier transformed and passed as boundary conditions. The angular velocities at step $n+1$ are then iteratively updated as

$$\dot{\theta}_{n+1} = \dot{\theta}_n + \frac{(1-f)\Delta t}{I}\left(\mathcal{T}_{t,n+1} - \kappa\left|\dot{\theta}_{n+1}\right|^{3/2}\right),$$

where $\mathcal{T}_{t,n+1}$ is the turbulent torque on each disc computed from the updated velocity field. This continues until the value for $\mathcal{T}_{t,n+1}$ converges, at which point the code progresses to the next time step.

Within this investigation a disc diameter of D=3.38 has been considered. The dimensions of the computational box dimensions are smaller than in the preceeding sections (L_x=2.26π, L_z=1.13π), while the grid resolution remains the same. This therefore means that a total of 4 discs are present within the computational domain, 2 on each channel wall. As the simulations are computationally costly due to the feedback needed to implement the boundary conditions, only two values of I have been investigated. Simulations have also been performed where the corrector step in the time-advancement of the disc-velocities is not enforced, i.e. a first-order explicit scheme. κ is dependent on D only and is identical in both cases. After discarding the initial transient period that occurs upon the introduc-

tion of the freely-rotating disc boundary conditions, the total integration time in both cases was t^+=6000.

It is necessary to first of all estimate dimensionless values of I that could be achievable in an experimental scenario. The experimental water channel parameters shown in table 3.1, are thus used for these calculations. Based on the values of u_τ^*, ρ^* and ν^* in this table, carbon fibre discs with D^*=35mm, and b^*=0.5mm result in a dimensionless moment of inertia of $I^+=2{\cdot}10^1 1$. Simulations of freely-rotating discs with this value of I^+ result in no disc motion. Results are instead presented for $I^+=2{\cdot}10^6$, which corresponds to a dimensional thickness b^*=5μm. It is noted that the manufacture of such discs would be a formidable challenge.

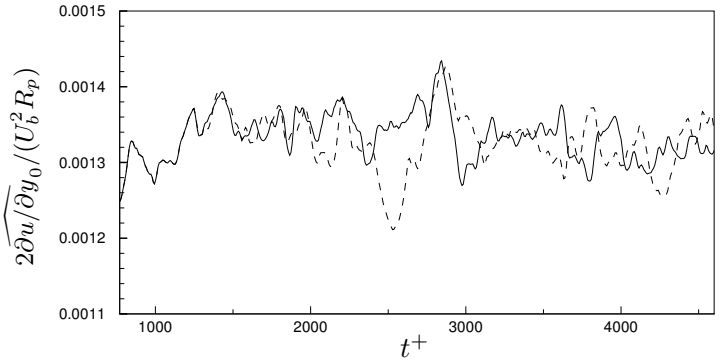

Fig. 5.5: Space-averaged streamwise wall-shear stress vs. time for D=3.38, $I^+=2{\cdot}10^6$ (dashed line). The wall-shear stress for the fixed-wall case is shown for comparison, and denoted by the solid line. The freely rotating disc boundary conditions are applied at t^+=770. Only a fraction of the total integration time is shown. The space-averaging operator here does not include time averaging.

The temporal evolution of the space-averaged wall-shear stress is displayed in figure 5.5. The freely-rotating disc boundary conditions are applied at t^+=770, and only a fraction of the total integration time is shown. The implementation of the freely rotating disc boundary conditions results in zero net drag reduction. As shown in figure 5.6 the maximum disc-tip velocity achieved is approximately W^+=0.2, hence the lack of drag reduction is unsurprising.

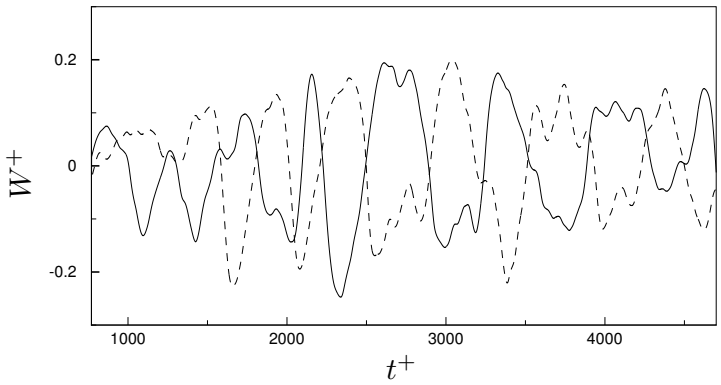

Fig. 5.6: Disc-tip velocity vs. time for D=3.38, I^+=2·10^6. Data for only two discs are shown.

A final arrangement has been investigated whereby freely-rotating disc boundary conditions are initiated after a period of steady rotation. Steadily rotating discs with diameter D=3.38, and tip-velocity W=0.52 (W^+=12) are applied to a fully-turbulent channel flow until a drag reduction regime of approximately $\mathcal{R}$=12% is obtained. At this stage the active disc rotation is terminated and the discs obey the equation of motion (5.3). The temporal development of the wall-shear stress is displayed in figure 5.7. The steady rotation boundary conditions are applied at t^+=770, and terminated at t^+=1540, this period is denoted by the shaded box in figure 5.7. For t^+>1540 no further energy is supplied to the discs to enforce their rotation. Once the active disc motion is stopped the wall-shear stress increases, returning to the fixed-wall value by approximately t^+=1900. The disc-tip velocity vs. time for the same arrangement is presented in figure 5.8. Once the active disc rotation is stopped at t^+=1540 the discs rapidly decelerate, reaching W^+=0 by t^+=1570.

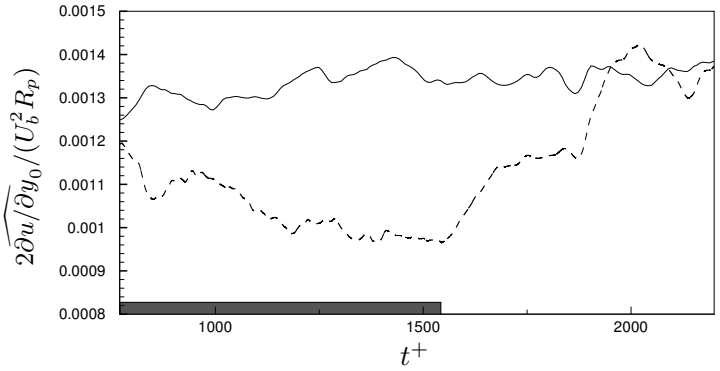

Fig. 5.7: Space-averaged streamwise wall-shear stress vs. time for D=3.38, I^+=2·10^6 (dashed line). Active disc rotation is enforced for 770<t^+<1540. For $t^+\geq$1540 the discs rotate according to equation 5.3. The wall-shear stress for the fixed-wall case is shown for comparison, and denoted by the solid line. Only a fraction of the total integration time is shown. The space-averaging operator here does not include time averaging.

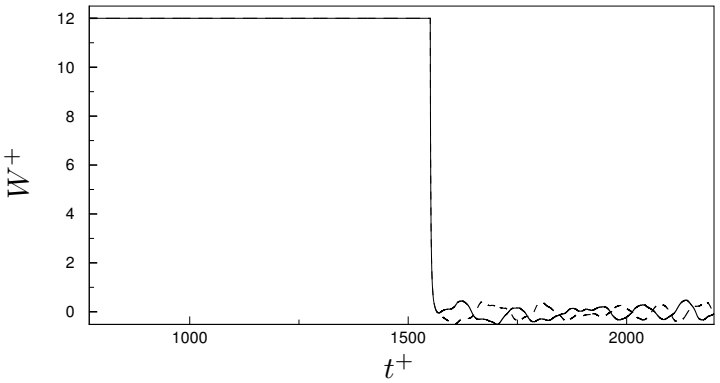

Fig. 5.8: Disc-tip velocity vs. time for D=3.38, I^+=2·10^6. Data for only two discs are shown to improve legibility.

6. SUMMARY AND FUTURE WORK

In this thesis the response of a turbulent channel flow to disc actuators has been investigated. In the first part of the thesis a novel oscillating-disc actuation strategy has been studied. This is followed by work on the effects of the arrangement of the actuators, and finally on modifications to the actuators to improve the resultant drag reduction. In all cases direct numerical simulations (DNS) have been performed at R_τ=180, based on the friction velocity of the stationary-wall reference case. The code utilized has been the subject of extensive grid resolution tests, and estimated uncertainty values for the performance quantities have been given where appropriate.

For the oscillating disc actuators it has been found that reductions of up to 20% in the wall-shear stress, and net power savings of 5.5% can be achieved. The optimal parameters for drag reduction (D^+=1089, W^+=13.4, T^+=801), and for power savings (D^+=855, W^+=6.4, T^+=880), have been determined from a parametric study. The dimensional values of the optimal parameters are presented for three flows of industrial interest, showing increased spatio-temporal forcing scales when compared to similar techniques. This therefore represents a step towards the implementation of the discs in relevant scenarios. Due to computational constraints the parameter range investigated has not been exhaustive. Further study is required, especially at larger values of D, to fully optimize this technique.

Through an extension of the Fukagata-Iwamoto-Kasagi (FIK) identity (Fukagata *et al.*, 2002) the total drag reduction has been separated into contributions from the modification to the turbulent Reynolds stresses, and from the time-

averaged disc Reynolds stresses. This has proved useful in identifying scalings for the two mechanisms thought to be responsible for the drag reduction. Flow visualizations have been effectively used to show that tubular structures presented between discs in the spanwise direction are wholly responsible for the disc Reynolds stresses.

The Rosenblat solution to the laminar flow above an oscillating disc has been useful as a predictor for the power spent enforcing the disc motion. Excellent agreement has been shown between the predicted laminar values and the values computed by the DNS. The laminar solution has also proven useful in predicting regions both in time and space where the power spent by the discs is positive. This means that in these regions energy transfer is from the fluid to the discs, a form of the regenerative braking effect. As alluded to previously, scalings for the drag reduction mechanisms have been found through the extended FIK identity. The first of these mechanisms is related to the shearing effect of the disc boundary layer, for which the drag reduction scales with the penetration depth of the layer. The second is related to the disc-flow Reynolds stresses, and in this case the drag reduction scales linearly with a simple function of the disc parameters. These scalings show an improved understanding of the control technique. Specifically it allows for the *a priori* estimation of drag reduction given a combination of disc parameters.

The second part of the thesis focusses on various layouts of the steadily-rotating disc actuators first studied by Ricco & Hahn (2013) (RH13). The layouts have been studied both with regards to the percentage of actuated wall in each case, and to the spacing between actuators in the homogeneous directions. It has been found that for low disc-tip velocities the drag reduction scales well with the percentage actuated area. However for higher tip velocities this scaling is lost. In some cases a reduction in the coverage, and therefore in the number of discs

on the channel walls, causes an increase in drag reduction. The reduction in the number of actuators can thus be considered a reduction in the complexity of the technique. As this also coincides an increase in performance, it therefore means that a further step has taken towards implementation of the control strategy. The increase in drag reduction coincides with increased spacing between actuators in the streamwise direction. A radial streaming effect created by the disc motion is responsible for the increase, a result found through comparison of the turbulent disc flow with the laminar von Kármán solution. The FIK identity used in collusion with flow visualizations has allowed criteria to be determined for the creation of the tubular structures present both in both RH13 and in Chapter 3. It has been found that the structures are created only when there is sufficient interaction between discs in the spanwise direction.

In the final part of the thesis modifications to the disc actuators are presented and discussed. These include novel half-disc and annular actuators, as well as a passive implementation of the disc drag reduction mechanism. Maximum drag reduction of 26% is observed for the half-disc actuators. These improvements to the strategy have been made following comparison of the induced flow with the laminar solution. The half-disc configuration eliminates the streamwise body forcing that was being created by the original disc actuators, an element of the control strategy that was causing local drag increase. The annular actuators retain the annular forcing created by the disc, and thus also retain the mechanism for drag reduction caused by the shearing effect of the disc boundary layer. The improvement comes from the removal of the central part of the disc for which the wall-velocity is lower. This also removes the induced wallward flow, thereby increasing the drag reduction. Finally a passive-disc drag reduction strategy where the discs are left to rotate dependent on the turbulent shear-stress results in zero net drag reduction.

The thesis is here concluded with a note on the proposed direction of research in the disc flow-control method. This strategy must be investigated at higher Reynolds number before it can be considered plausible for industrial application. As the optimal forcing parameters may change with Reynolds number, as may the maximum attainable values of drag reduction and power savings themselves, further study into the Reynolds number effect is of paramount importance. Finally, the results on the passive actuators represent another area which would benefit from further research. It is recognized that the modelling of the freely-rotating discs may require further consideration. The code used within the present study is however not suitable for this study, as it would surely be computationally very heavy.

APPENDIX

A. THE CHANNELFLOW CODE

The code implemented in this work, found at `channelflow.org` is an open-source C++ direct numerical simulator for the fluid flow between two infinite, periodic, rectangular, parallel plates. The code replicates an incompressible wall-bounded flow contained within $\Theta \equiv L_x\mathbb{T} \times [0,2] \times L_z\mathbb{T}$, where $\mathbb{T}$ is the periodic unit interval. In this domain the flow is governed by the incompressible Navier-Stokes equations, given in equations (1.1) and (1.2).

The computational domain created within Θ has N_x, N_y and N_z gridpoints in the x, y and z directions respectively. In physical space these gridpoints are be given by

$$\begin{aligned} x_n &= \frac{nL_x}{N_x}, \qquad n = 0, 1, 2, ..., N_x - 1, \\ z_n &= \frac{nL_z}{N_z}, \qquad n = 0, 1, 2, ..., N_z - 1. \end{aligned}$$

The velocity and pressure variables are represented in spectral as well as physical space, and `channelflow` makes use of the Fastest Fourier Transform in the West (FFTW) libraries to perform these conversions. By transforming the variables from physical to spectral space differentiation in the x and z directions is simplified.

The code uses Chebyshev discretisation in the y direction to obtain greater refinement in the region immediately adjacent to the walls. This refinement is created according to

$$y_n = \frac{b+a}{2} + \frac{b-a}{2} \cos\left(\frac{n\pi}{N_y - 1}\right), \qquad n = 0, 1, 2, ..., N_y - 1,$$

where y_n is the location of the n-th coordinate, and a and b are the locations of the channel walls (a=$-b$=-1).

A.1 Nonlinear terms

`Channelflow` implements any of the convection, divergence, skew-symmetric or rotational forms of the nonlinear term, detailed in table A.1. Of these forms -

Convection form:	$\mathbf{u}\cdot\nabla\mathbf{u}$
Divergence form:	$\nabla\cdot(\mathbf{uu})$
Skew-symmetric form:	$\frac{1}{2}\mathbf{u}\cdot\nabla\mathbf{u}+\frac{\mathbf{1}}{\mathbf{2}}\nabla\cdot(\mathbf{uu})$
Rotational form:	$(\nabla\times\mathbf{u})\times\mathbf{u}+\frac{\mathbf{1}}{\mathbf{2}}\nabla(\mathbf{u}\cdot\mathbf{u})$

Tab. A.1: Forms of the nonlinear term which are implemented within the channelflow code.

all of which are identical in continuous mathematics (assuming $\nabla\cdot\mathbf{u}$=0) - the rotational form is the least expensive computationally and is thus chosen for the current work. The rotational form is less accurate than the skew-symmetric form (Zang, 1991), particularly in the near-wall region. The use of Chebyshev discretisation in the wall-normal direction limits this error (Horiuti, 1987), as does the use of dealiased transforms.

The code does not carry out the computation on the rotational form as described by equation (1.1). Instead, the nonlinear term is expanded using Reynolds' decomposition, after which the rotational form is applied to the turbulent convective term only. When the rotational form is in use the equation to be solved at each time step is thus

$$\frac{\partial\mathbf{u}_t}{\partial t}+\nabla\left[p+\frac{1}{2}\mathbf{u}_t\cdot\mathbf{u}_t\right]=\frac{1}{R_p}\nabla^2\mathbf{u}_t-(\nabla\times\mathbf{u}_t)\times\mathbf{u}_t+\mathbf{u}_m\frac{\partial\mathbf{u}_t}{\partial x}+v_t\frac{\partial\mathbf{u}_m}{\partial y}+\frac{1}{R_p}\nabla^2\mathbf{u}_m-\Pi_x. \tag{A.1}$$

In order to make the time-stepping algorithm more compact to present, the following definitions are used following the convention of (Gibson, 2006). The nonlinear term, $\mathbf{N}(\mathbf{u})$, is defined as

$$\mathbf{N}(\mathbf{u}) \triangleq (\nabla \times \mathbf{u_t}) \times \mathbf{u_t} + \mathbf{u_p}\frac{\partial \mathbf{u_t}}{\partial \mathbf{x}} + \mathbf{v_t}\frac{\partial \mathbf{u_p}}{\partial \mathbf{y}},$$

the modified pressure, $\mathbf{q}$, is

$$\mathbf{q} \triangleq p + \frac{1}{2}\mathbf{u}_t \cdot \mathbf{u}_t,$$

the linear term, $\mathbf{Lu}$, is

$$\mathbf{Lu} \triangleq \frac{1}{R_p}\nabla^2 \mathbf{u}_t,$$

and the constant term $\mathbf{C}$ is

$$\mathbf{C} \triangleq \frac{1}{R_p}\frac{\partial^2 \mathbf{u}_m}{\partial y^2} - \Pi_x.$$

Using these definitions, (A.1) is now written as:

$$\frac{\partial \mathbf{u_t}}{\partial t} + \nabla \mathbf{q} = \mathbf{Lu} - \mathbf{N}(\mathbf{u}) + \mathbf{C}. \tag{A.2}$$

Time advancement within the code is carried out in Fourier space, and so the continuous Fourier transform must be applied to equation (A.2). Using the Fourier transformed ∇, ∇^2 and L operators, given in Gibson (2006), we obtain

$$\frac{\partial \hat{\mathbf{u}}}{\partial t} + \hat{\nabla}\hat{\mathbf{q}} = \hat{\mathbf{L}}\hat{\mathbf{u}} - \hat{\mathbf{N}} + \hat{\mathbf{C}},$$

where the wavenumber subscripts are omitted for convenience.

A.2 Time-stepping algorithm

`Channelflow` can implement any of seven time-stepping algorithms. Of these the 3^{rd} order semi-implicit backward differentiation method (`SBDF3`) is the default. This is due to its stability, and as it results in pressure and velocity fields of the same order accuracy. In this scheme the linear term $\mathbf{L}(\mathbf{u})$ is treated implicitly

and the nonlinear term $\mathbf{N}(\mathbf{u})$ explicitly. Specifically the `SBDF3` method uses a 3$^{\text{rd}}$ order backward Euler scheme for $\mathbf{Lu}$ and an explicit Adams-Bashford method for $\mathbf{N}(\mathbf{u})$. In order to illustrate the method it can be applied to equation (A.2) as follows:

$$\frac{11\hat{\mathbf{u}}^{n+1} - 18\hat{\mathbf{u}}^{n} + 9\hat{\mathbf{u}}^{n-1} - 2\hat{\mathbf{u}}^{n-2}}{6\Delta t} + \hat{\nabla}\hat{\mathbf{q}} = \hat{\mathbf{L}}\hat{\mathbf{u}}^{n+1} - 3\hat{\mathbf{N}}^{n} + 3\hat{\mathbf{N}}^{n-1} - \hat{\mathbf{N}}^{n-2} + \hat{C}.$$

After rearranging, this takes the form of a Helmholtz equation

$$\hat{\mathbf{L}}\hat{\mathbf{u}}^{n+1} - \lambda\hat{\mathbf{u}}^{n+1} = \hat{\mathbf{S}}, \tag{A.3}$$

where λ=$11/(6\Delta t)$ and $\hat{\mathbf{S}}$ is the source term containing terms at time step n or previous. This is then solved in Fourier space.

A.3 Kleiser-Schumann algorithm

To describe the Kleiser-Schumann algorithm it is necessary to expand the linear operator $\hat{\mathbf{L}}$, and to discretise the modified pressure $\hat{\mathbf{q}}$ in the source term, from equation (A.3) this obtains

$$\nu\hat{\mathbf{u}}''^{n+1} - \lambda\hat{\mathbf{u}}^{n+1} - \hat{\nabla}\hat{q}^{n+1} = \hat{\mathbf{S}}, \tag{A.4}$$

where the prime denotes differentiation with respect to y, and λ is redefined as

$$\lambda \triangleq \frac{11}{6\Delta t} + 4\pi^2\left(\frac{k_x^2}{L_x^2} + \frac{k_z^2}{L_z^2}\right).$$

At each timestep it is thus necessary to solve (A.4) for each Fourier mode combination. Completing the system of equations we also have the Fourier transformed continuity equation and the boundary conditions

$$\hat{\nabla}\cdot\hat{\mathbf{u}} = \quad 0, \tag{A.5}$$

$$\hat{\mathbf{u}}_{k_x,k_z} = \quad \hat{\mathbf{u}}_w, \tag{A.6}$$

where $\hat{\mathbf{u}}_w$ is the velocity vector at the wall. Equations (A.4)-(A.6) are referred to as the tau equations by Gibson (2006) and consist of a set of three coupled

differential equations with four unknowns. The algorithm, first presented by Kleiser & Schumann (1980) decomposes the tau equations into independent one-dimensional Helmholtz equations which are then easily solved. Using the method described by Canuto *et al.* (1988) we first obtain the Poisson equation for pressure through the differentiation and summation of the momentum equations, and simplification through the continuity equation. In Fourier space this equation is written as

$$\hat{q}'' - (k_x^2 + k_z^2)\hat{q} = \hat{\nabla} \cdot \hat{\mathbf{S}}, \tag{A.7}$$

and has boundary conditions

$$\hat{\nabla} \cdot \hat{\mathbf{u}}_{k_x,k_z}(\pm 1) = 0, \quad \text{i.e.,} \quad \hat{v}'_{k_x,k_z}(\pm 1) = 0.$$

Taking only the y component of (A.4), and the Poisson pressure equation (A.7), a system of equations for $\hat{v}$ and $\hat{q}$ can be isolated. If the derivative with respect to y is now expressed as $\mathcal{D}$, these equations can be put into matrix form as

$$\mathcal{L}\begin{pmatrix} \hat{p} \\ \\ \hat{v} \end{pmatrix} = \hat{f} \qquad \hat{v}(\pm 1) = \hat{v}'(\pm 1) = 0, \tag{A.8}$$

where $\mathcal{L}$ and $\hat{f}$ are given by

$$\mathcal{L} = \begin{pmatrix} \mathcal{D}^2 - (k_x^2 + k_z^2) & 0 \\ \\ -\frac{1}{\rho} & \nu\mathcal{D}^2 - \lambda \end{pmatrix} \quad , \quad \hat{f} = \begin{pmatrix} \hat{\nabla} \cdot \hat{\mathbf{S}} \\ \\ -\hat{S}_1 \end{pmatrix}.$$

Equation (A.8) is described by Kleiser & Schumann (1980) as the A-problem and is not easily solved due to the appearance of $\hat{q}$ in the equation for $\hat{v}$, whilst the boundary conditions also contain $\hat{v}$.

To solve the A-problem, Kleiser & Schumann (1980) formed the related B-problem, consisting of two scalar, uncoupled Helmholtz equations. The solution to the A-problem can then be expressed as a linear combination to three separate

solutions to the B-problem.

$$\mathcal{L}\begin{pmatrix}\hat{q}\\ \\ \hat{v}\end{pmatrix} = \hat{f} \qquad \hat{q}(\pm 1) = \hat{q}_{b\pm}, \quad \hat{v}(\pm 1) = 0.$$

The separation of the A-problem into the three individual solutions to the B-problem is done by decomposing the pressure field into those solved for: (1) zero pressure boundary conditions at either wall $(\hat{v}_p, \hat{p}_p)$, (2) unit pressure boundary conditions at the upper wall $(\hat{v}_+, \hat{p}_+)$ and (3) unit pressure boundary conditions at the lower wall $(\hat{v}_-, \hat{p}_-)$

$$\begin{pmatrix}\hat{q}\\ \\ \hat{v}\end{pmatrix} = \begin{pmatrix}\hat{q}_p\\ \\ \hat{v}_p\end{pmatrix} + \delta_+ \begin{pmatrix}\hat{q}_+\\ \\ \hat{v}_+\end{pmatrix} + \delta_- \begin{pmatrix}\hat{q}_-\\ \\ \hat{v}_-\end{pmatrix}.$$

The relation between the A-problem and the linear combination of the B-problems is then expressed as follows

$$\mathcal{L}\begin{pmatrix}\hat{q}\\ \\ \hat{v}\end{pmatrix} = \mathcal{L}\begin{pmatrix}\hat{q}_p\\ \\ \hat{v}_p\end{pmatrix} + \delta_+\mathcal{L}\begin{pmatrix}\hat{q}_+\\ \\ \hat{v}_+\end{pmatrix} + \delta_-\mathcal{L}\begin{pmatrix}\hat{q}_-\\ \\ \hat{v}_-\end{pmatrix},$$

where δ_+ and δ_- are constants operating on solutions of the latter two versions of the B-problem.

As described above the first B-problem to be solved is for zero pressure boundary conditions at either wall, the problem given by

$$\mathcal{L}\begin{pmatrix}\hat{q}_p\\ \\ \hat{v}_p\end{pmatrix} = \hat{f} \qquad \hat{q}_p(\pm 1) = \hat{v}_p(\pm 1) = 0.$$

The second B-problem then posed is that with unit pressure boundary conditions at y=+1 (the upper wall), the solutions to this one are given by ($\hat{p}_+$,$\hat{v}_+$) and the problem is written as

$$\mathcal{L}\begin{pmatrix}\hat{q}_+\\ \\ \hat{v}_+\end{pmatrix} = 0 \qquad \hat{q}_+(+1) = 1, \quad \hat{q}_+(-1) = \hat{v}_+(\pm 1) = 0.$$

Finally, the third B-problem to be solved is that with unit pressure boundary conditions at $y = -1$ (the lower wall), the solutions given by $(\hat{p}_-, \hat{v}_-)$ and the problem is written as

$$\mathcal{L}\begin{pmatrix}\hat{q}_- \\ \\ \hat{v}_-\end{pmatrix} = 0 \qquad \hat{q}_-(-1) = 1, \quad \hat{q}_-(+1) = \hat{v}_-(\pm 1) = 0.$$

The boundary contions for the A-problem can be written in the form termed by Kleiser & Schumann (1980) the influence-matrix equation

$$\begin{bmatrix}\hat{v}'_+(+1) & \hat{v}'_-(+1) \\ \\ \hat{v}'_+(-1) & \hat{v}'_-(-1)\end{bmatrix}\begin{pmatrix}\delta_+ \\ \\ \delta_-\end{pmatrix} = -\begin{pmatrix}\hat{v}_p(+1) \\ \\ \hat{v}_p(-1)\end{pmatrix}.$$

It is noted that by solving this influence-matrix equation for $\delta_\pm$ the correct boundary conditions to the B-problem are given, the solution to which also satisfies the original A-problem.

The derivation of the Poisson pressure equation (A.7) from the time-discretised Helmholtz equation (A.3) is performed assuming the ability to perform continuous differentiation in the y direction. However had this derivation been carried out with the additional terms created from discretisation, the solution would need to be corrected to remove any associated error. Kleiser & Schumann (1980) outline a *tau correction* step in their algorithm which channelflow is able to perform, however this is not necessary for sufficiently large N_y (Canuto *et al.*, 1988).

A.4 Parallel scalability

The strong scaling of the parallel version of the channel code is shown in figure A.1 (left). For this test the problem to be solved remains constant (i.e. the number of grid points in the simulation remains constant), and the number of processing elements is varied. The test case was a stationary wall simulation with 128 nodes in the x and z directions, and 129 nodes in y. The speed-up S_p, is defined as

S_p=T_0/T_p, where T_0 is the time taken for the simulation to run in serial, and T_p is the time taken to run the simulation on p processors. The maximum speed-up was obtained for 32 processors. Limitations associated with the computer cluster have meant it was not possible to use more than 32 processors for shared-memory parallelisation. The strong scaling efficiency of the parallel code, given by E_p=$T_0/(pT_p)$ is plotted in figure A.1 (right). Given these results, a compromise was then sought between speed-up, efficiency, and queue-time on the cluster. All simulations in the present work have been performed using 16 CPUs.

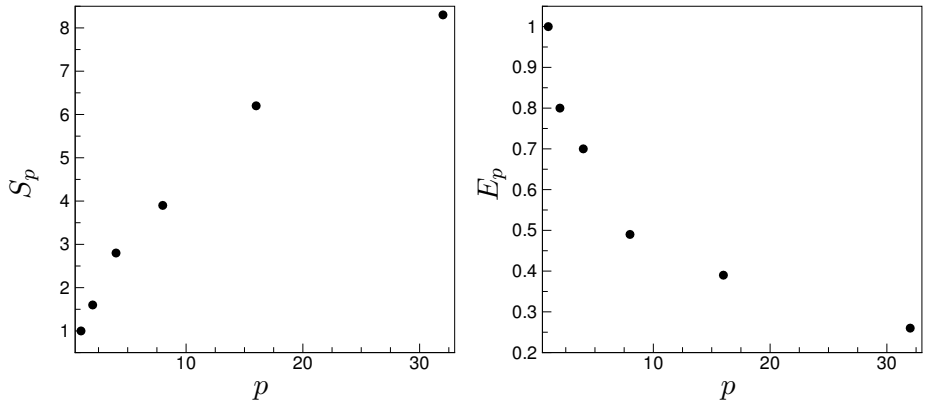

Fig. A.1: Left: Speed-up, S_p vs. p, the number of processing elements. Right: Strong scaling efficiency, E_p vs. p.

B. RESOLUTION CHECKS

Resolution checks have been performed on the maximum $\mathcal{P}_{net}$ and maximum $\mathcal{R}$ cases in section §3.3.2 for D=3.38 to observe uncertainty in the performance quantities due to the effect of the discretisation parameters. The results are presented in tables B.2 and B.1. From table B.2 the maximum drag reduction value for D=3.38 is given as $\mathcal{R}$=17±0.5%. From table B.1 the maximum $\mathcal{P}_{net}$ is given as $\mathcal{P}_{net}$=6±1.0%. Although not included in the tables, the drag reduction computed using the FIK identity is within 3% for all cases listed below. It is expected that there is larger uncertainty in the oscillating disc simulations than in the steady disc rotation cases. This is due to the unsteady nature of the forcing.

L_x	L_z	Δx^+	Δz^+	N_x	N_y	N_z	$\mathcal{R}(\%)$	$-\mathcal{P}_{sp,t}(\%)$	$\mathcal{P}_{net}(\%)$
6.79	2.26	10	5	334	129	222	17.1	26.4	-9.3
6.79	2.26	11.5	5.75	334	129	222	17.2	22.9	-5.1
4.59	2.26	11.5	5.75	222	129	222	17.8	22.9	-5.1
6.79	2.26	8	5.75	480	129	222	17.4	23.2	-5.5
6.79	2.26	11.5	4	334	129	320	17.6	27.1	-9.3
6.79	2.26	11.5	5.75	334	161	222	17.9	25.5	-7.7
4.59	3.4	11.5	5.75	222	129	334	17.8	25.7	-7.9
6.79	1.13	11.5	5.75	334	257	112	17.7	23.1	-5.4
6.79	2.26	8	4	320	129	320	18.0	27	-9.0

Tab. B.1: The effects of discretisation parameters on calculated values from the maximum $\mathcal{R}$ case for D=3.38. The period of the time average is constant for each case, $t_f - t_i$=1690. The disc parameters are D=3.38, W=0.51 and T=65.

L_x	L_z	Δx^+	Δz^+	N_x	N_y	N_z	$\mathcal{R}(\%)$	$-\mathcal{P}_{sp,t}(\%)$	$\mathcal{P}_{net}(\%)$
6.79	2.26	10	5	384	129	256	11.8	5.8	6.0
6.79	2.26	11.5	5.75	334	129	222	11.6	5.2	6.4
4.59	2.26	11.5	5.75	222	129	222	12.0	5.3	6.7
6.79	2.26	8	5.75	480	129	222	12.1	5.7	6.4
6.79	2.26	11.5	4	334	129	320	12.4	5.4	7.0
6.79	2.26	11.5	5.75	334	161	222	12.1	5.8	6.4
4.59	3.4	11.5	5.75	222	129	334	11.7	5.3	6.3
6.79	1.13	11.5	5.75	334	257	112	11.7	5.8	5.9
6.79	2.26	8	4	320	129	320	12.1	6.0	6.1

Tab. B.2: The effects of discretisation parameters on calculated values from the maximum $\mathcal{P}_{net}$ case for D=3.38. The period of the time average is constant for each case, $t_f - t_i$=1690. The disc parameters are D=3.38, W=0.26 and T=130.

C. TABLE OF DATA FOR ARRANGEMENTS OF DISC ACTUATORS

The data for $\mathcal{R}$ and $\mathcal{P}_{sp,t}$ for Chapter 4 are given in Table C.1.

	Case	W	$\mathcal{R}(\%)$	$-\mathcal{P}_{sp,t}(\%)$		Case	W	$\mathcal{R}(\%)$	$-\mathcal{P}_{sp,t}(\%)$
	0	0.13	7.2	2.4		3	0.13	3.6	1.2
	0	0.26	16.2	9.8		3	0.26	10.3	5.0
□	0	0.39	18.3	22.7	○	3	0.39	14.0	11.6
	0	0.52	11.9	42.5		3	0.52	15.5	21.7
	1	0.13	1.7	0.6		4	0.13	3.6	1.2
	1	0.26	5.1	2.5		4	0.26	10.3	5.0
▽	1	0.39	7.4	5.8	◇	4	0.39	14.0	11.6
	1	0.52	8.5	10.9		4	0.52	15.5	21.6
	2	0.13	3.5	1.2		5	0.13	8.0	2.7
	2	0.26	8.2	5.0		5	0.26	17.0	9.7
△	2	0.39	9.4	11.4	▷	5	0.39	18.5	24.7
	2	0.52	8	21.4		5	0.52	14.8	46.4

Tab. C.1: Performance data for different forcing conditions and layouts.

D. DERIVATION OF EQUATION OF MOTION FOR FREELY-ROTATING DISCS

Herein is detailed the derivation of the non-dimensional equations of motion for the freely-rotating discs. This begins from equation (5.1),

$$I^*\ddot{\theta}^* = \Sigma\mathcal{T}^*,$$

where $I^*{=}m^*D^{*2}/8$ is the moment of inertia of the disc, $\ddot{\theta}^*$ is its angular acceleration, and $\Sigma\mathcal{T}^*$ is the sum of torques acting upon it.

The mass m^* of the disc is equal to the product of its volume and density, i.e. $m^*{=}\rho_d^*V^*$, where $\rho{*}_d$ is the density of the disc material, $V^*{=}\pi D^{*2}b^*/4$ is its volume, and b^* is its thickness. Writing ρ_d^* as a multiple of the fluid density ρ^* (i.e. $\rho_d^*{=}a\rho^*$), the moment of inertia of the disc is given by

$$I^* = \frac{a\pi D^{*4}b^*\rho^*}{32}$$

The turbulent torque $\mathcal{T}_t^*$ is then equivalent to the integral of $\tau_\theta^* r$ over the disc surface, where $\tau_\theta^*{=}\mu^*\,\partial u_\theta^*/\partial y^*|_{wall}$ is the azimuthal shear stress on the disc. $\mathcal{T}_t^*$ is therefore

$$\mathcal{T}_t^* = \int_0^{D^*/2}\int_0^{2\pi} \mu^* r^{*2}\left.\frac{\partial u_\theta^*}{\partial y^*}\right|_{wall} \mathrm{d}\theta^*\mathrm{d}r.$$

The fluid friction torque $\mathcal{F}_f^*$ is modelled by the laminar von Kármán rotating disc solution. The torque on the wetted surface of a disc rotating beneath a quiescent fluid is given in Schlichting (1979) as

$$\mathcal{F}_f^* = \frac{\nu^{*1/2}G_k\pi\rho^*D^{*4}\left|\dot{\theta}^*\right|^{3/2}}{32}.$$

Modelling the mechanical friction $\mathcal{F}_m^*$ as a constant proportional loss of the other torques acting on the disc, i.e. as $\mathcal{F}_m^*{=}{-}f(\mathcal{T}_t^* - \mathcal{F}_f^*)$, the dimensional equation of motion for the disc is obtained

$$\frac{a\pi D^{*4}b^*}{32}\ddot{\theta}^* = (1-f)\left[\nu^*\int_0^{D^*/2}\int_0^{2\pi} r^{*2}\frac{\partial u_{\theta^*}}{\partial y^*}\mathrm{d}\theta^*\mathrm{d}r^* - \mathrm{sgn}(\theta^*)\frac{\nu^{*1/2}G_k\pi\rho^*D^{*4}\left|\dot{\theta}^*\right|^{3/2}}{32}\right].$$

The $\mathrm{sgn}(\theta^*)$ term is introduced here to ensure that the fluid friction always acts in the opposite direction to the disc motion. Non-dimensionalization into outer units yields

$$I\ddot{\theta} = (1-f)\left[\frac{1}{R_p}\int_0^{D/2}\int_0^{2\pi} r^2\frac{\partial u_\theta}{\partial y}\mathrm{d}\theta\mathrm{d}r - \kappa\left|\theta\right|^{3/2}\right],$$

where $I{=}a\pi D^4b/32$, and $\kappa{=}\mathrm{sgn}(\theta)G_k\pi D^4/(32R_p^{1/2})$.

BIBLIOGRAPHY

Abramowitz, M. & Stegun, I. 1964 *Handbook of Mathematical Functions*. Nat. Bureau Stand. Appl. Math. Ser. 55.

Amitay, M. & Glezer, A. 2006 Aerodynamic flow control using synthetic jet actuators. In *Control of Fluid Flow*, pp. 45–73. Springer.

Bandyopadhyay, P. R. 2006 Stokes mechanism of drag reduction. *J. Appl. Mech.* **73**, 483–489.

Baron, A. & Quadrio, M. 1996 Turbulent drag reduction by spanwise wall oscillations. *Appl. Sc. Res.* **55**, 311–326.

Batchelor, G. K. 1967 *An Introduction to Fluid Dynamics*. Cambridge University Press.

Bechert, D., Bartenwerfer, M., Hoppe, G. & Reif, W. E. 1986 Drag reduction mechanisms derived from sharkskin. In *15th Congr. of the Intl Council of the Aeronautical Sciences*. London, UK: AIAA.

Bechert, D. & Bertenwerfer, M. 1989 The viscous flow on surfaces with longitudinal ribs. *J. Fluid Mech.* **206**, 105–209.

Bechert, D., Brusek, M., Hagel, W., Höven, J. G. T. v. d. & Hoppe, G. 1997 Experiments on drag reducing surfaces and their optimization with an adjustable geometry. *J. Fluid Mech.* **338**, 59–87.

Bechert, D., Hoppe, G. & Reif, W. E. 1985 On the drag reduction of the shark skin. *AIAA Paper* pp. 85–0546.

Benney, D. 1964 The flow induced by a disk oscillating in its own plane. *J. Fluid Mech.* **18** (03), 385–391.

Berger, T., Kim, J., Lee, C. & Lim, J. 2000 Turbulent boundary layer control utilizing the Lorentz force. *Phys. Fluids* **12** (3), 631–649.

Bisignani, G. 2011 IATA Annual Report 2011. *Tech. Rep.*. International Air Transport Association, Singapore.

Bradshaw, P. & Pontikos, N. S. 1985 Measurements in the turbulent boundary layer on an 'infinite' swept wing. *J. Fluid Mech.* **159**, 105–130.

Brändlein, J., Eschmann, P., Hasbargen, L. & Weigang, K. 1999 *Ball and roller bearings: theory, design, and application*. John Wiley & Sons, 3rd ed.

Canuto, C., Hussaini, M., Quarteroni, A. & Zang, T. 1988 *Spectral Methods in Fluid Dynamics*. Springer-Verlag, New York.

Carmi, S. & Tustaniwskyj, J. 1981 Stability of modulated finite-gap cylindrical Couette flow: linear theory. *J. Fluid Mech.* **108**, 19–42.

Choi, H., Moin, P. & Kim, J. 1993 Direct numerical simulation of turbulent flow over riblets. *J. Fluid Mech.* **255**, 503.

Choi, H., Moin, P. & Kim, J. 1994 Active turbulence control for drag reduction in wall-bounded flows. *J. Fluid Mech.* **262**, 75.

Choi, J.-I., Xu, C.-X. & Sung, H. 2002 Drag reduction by spanwise wall oscillation in wall-bounded turbulent flows. *AIAA J.* **40** (5), 842.

Choi, K.-S. & Graham, M. 1998 Drag reduction of turbulent pipe flows by circular-wall oscillation. *Phys. Fluids* **10** (1), 7–9.

Cimarelli, A., Frohnapfel, B., Hasegawa, Y., De Angelis, E. & Quadrio, M. 2013 Prediction of turbulence control for arbitrary periodic spanwise wall movement. *Phys. Fluids* **25** (075102).

Dhanak, M. & Si, C. 1999 On reduction of turbulent wall friction through spanwise oscillations. *J. Fluid Mech.* **383**, 175–195.

Di Cicca, G. M., Iuso, G., Spazzini, P. G. & Onorato, M. 2002 Particle image velocimetry investigation of a turbulent boundary layer manipulated by spanwise oscillations. *J. Fluid Mech.* **467**, 41–56.

Driver, D. & Hebbar, S. 1987 Experimental study of a three-dimensional, shear-driven, turbulent boundary layer. *AIAA J.* **25** (35).

Du, Y., Symeonidis, V. & Karniadakis, G. 2002 Drag reduction in wall-bounded turbulence via a transverse travelling wave. *J. Fluid Mech.* **457**, 1–4.

Duque-Daza, C., Baig, M., Lockerby, D., Chernyshenko, S. & Davies, C. 2012 Modelling turbulent skin-friction control using linearized Navier-Stokes equations. *J. Fluid Mech.* **702**, 403–414.

Favaro, A. 1918 *Intorno al trattato di Leonardo da Vinci sul moto e misura dell'acqua*. Reale Accademia dei Lincei. Rendiconti.

Fukagata, K., Iwamoto, K. & Kasagi, N. 2002 Contribution of Reynolds stress distribution to the skin friction in wall-bounded flows. *Phys. Fluids* **14** (11), 73.

García-Mayoral, R. & Jiménez, J. 2011 Drag reduction by riblets. *Phil. Trans. Royal Soc. A* **369** (1940), 1412–1427.

Gibson, J. F. 2006 Channelflow: a spectral Navier-Stokes simulator in C++. *http://www.channelflow.org/*.

Goldstein, D., Handler, R. & Sirovich, L. 1995 Direct numerical simulation of turbulent flow over a modelled riblet-covered surface. *J. Fluid Mech.* **302** (10), 333–376.

Gouder, K., Potter, M. & Morrison, J. 2013 Turbulent friction drag reduction using electroactive polymer and electromagnetically driven surfaces. *Exp. Fluids* **54**, 1.

Gad-el Hak, M. 2000 *Flow control - Passive, Active and Reactive Flow Management*. Cambridge University Press.

Hinze, J. 1975 *Turbulence*. McGraw Hill, Inc. – Second Edition.

Hœpffner, J. & Fukagata, K. 2009 Pumping or drag reduction? *J. Fluid Mech.* **635**, 171.

Hooshmand, A., Youngs, R., Wallace, J. & Balint, J. L. 1983 An experimental study of changes in the structure of a turbulent boundary layer due to surface geometry changes. *AIAA Paper* pp. 83–0230.

Horiuti, K. 1987 Comparison of conservative and rotational forms in large eddy simulation of turbulent channel flow. *J. Comp. Phys.* **71**, 343–370.

Iuso, G., Di Cicca, G. M., Onorato, M., Spazzini, P. G. & R., M. 2003 Velocity streak structure modifications induced by flow manipulation. *Phys. Fluids* **15** (9), 2602–2612.

Jung, W., Mangiavacchi, N. & Akhavan, R. 1992 Suppression of turbulence in wall-bounded flows by high-frequency spanwise oscillations. *Phys. Fluids A* **4** (8), 1605.

Kang, S. & Choi, H. 2000 Active wall motions for skin-friction drag reduction. *Phys. Fluids* **12** (12), 3301–3304.

von Kármán, T. 1937 Turbulence. *J. Roy. Aeronaut. Soc.* **41** (1109).

Kasagi, N., Suzuki, Y. & Fukagata, K. 2009 Micromechanical systems-based feedback control of turbulence for skin friction reduction. *Ann. Rev. Fluid Mech.* **41**, 231.

Keefe, L. 1995 Drag reduction by nonlinear flow control. *Tech. Rep.* CR-195058. NASA.

Keefe, L. 1997 A normal vorticity actuator for near-wall modification of turbulent shear flows. *AIAA Paper* **97-0547**.

Keefe, L. 1998 Method and apparatus for reducing the drag of flows over surfaces. *United States Patent* **5,803,409**.

Kennedy, J. L. 1993 *Oil and gas pipeline fundamentals*, 2nd edn. PennWell Books.

Kim, J., Moin, P. & Moser, R. 1987 Turbulence statistics in fully developed channel flow at low Reynolds number. *J. Fluid Mech.* **177**, 133–166.

Kleiser, L. & Schumann, U. 1980 Treatment of incompressibility and boundary conditions in 3-D numerical spectral simulations of plane channel flows. In *Proc. 3rd GAMM Conf. Numerical Methods in Fluid Mechanics* (ed. E. Hirschel), p. 165. GAMM, Vieweg.

Klewicki, J. & Hill, R. 2003 Laminar boundary layer response to rotation of a finite diameter surface patch. *Phys. Fluids* **15** (1), 101.

Koch, H. & Kozulovic, D. 2013 Drag reduction by boundary layer control with passively moving wall. In *ASME 2013 Fluids Engineering Division Summer Meeting*, p. V01BT15A004. American Society of Mechanical Engineers.

Kuang-Chen Liu, D., Friend, J. & Yeo, L. 2010 A brief review of actuation at the micro-scale using electrostatics, electromagnetics and piezoelectric ultrasonics. *Acoust. Sci. & Tech.* **31**, 115 – 123.

Laadhari, F., Skandaji, L. & Morel, R. 1994 Turbulence reduction in a boundary layer by local spanwise oscillating surface. *Phys. Fluids* **6** (10), 3218.

Luchini, P. 2008 Acoustic streaming and lower-than-laminar drag in controlled channel flow. In *Progress in Industrial Mathematics at ECMI 2006*, pp. 169–177. Springer.

Min, T., Kang, S. M., Speyer, J. L. & Kim, J. 2006 Sustained sub-laminar drag in a fully developed channel flow. *J. Fluid Mech.* **558**, 309–318.

Moarref, R. & Jovanovic, M. 2012 Model-based design of transverse wall oscillations for turbulent drag reduction. *J. Fluid Mech.* **707**, 205–240.

Moin, P., Shih, T., Driver, D. & Mansour, N. 1990 Direct numerical simulation of a three-dimensional turbulent boundary layer. *Phys. Fluids A* **2** (1846).

Orlandi, P. & Fatica, M. 1997 Direct simulations of turbulent flow in a pipe rotating about its axis. *J. Fluid Mech.* **343**, 43–72.

Panton, R. 1995 *Incompressible Flow*. Wiley-Interscience – Second Edition.

Pope, S. 2000 *Turbulent Flows*. Cambridge University Press.

Pozrikidis, C. 2009 *Fluid Dynamics: Theory, Computation, and Numerical Simulation*. Springer.

Prandtl, L. 1904 Uber Flussigkeitsbewegung bei sehr kleiner Reibung. In *Proc. Third Int. Math. Cond.*, pp. 484–491. Heidelberg, Germany.

Quadrio, M., Floryan, J. & Luchini, P. 2007 Effect of streamwise-periodic wall transpiration on turbulent friction drag. *J. Fluid Mech.* **576**, 424–444.

Quadrio, M. & Ricco, P. 2003 Initial response of a turbulent channel flow to spanwise oscillation of the walls. *J. Turbul.* **4 007**.

Quadrio, M. & Ricco, P. 2004 Critical assessment of turbulent drag reduction through spanwise wall oscillations. *J. Fluid Mech.* **521**, 251.

Quadrio, M. & Ricco, P. 2011 The laminar generalized Stokes layer and turbulent drag reduction. *J. Fluid Mech.* **667**, 135–157.

Quadrio, M., Ricco, P. & Viotti, C. 2009 Streamwise-travelling waves of spanwise wall velocity for turbulent drag reduction. *J. Fluid Mech.* **627**, 161.

Quadrio, M. & Sibilla, S. 2000 Numerical simulation of turbulent flow in a pipe oscillating around its axis. *J. Fluid Mech.* **424**, 217–241.

Reynolds, O. 1883 An experimental investigation of the circumstances which determine whether the motion of water shall be direct or sinuous, and of the law of resistance in parallel channels. *Phil. Trans. R. Soc.* **35** (224-226), 84–99.

Reynolds, O. 1895 On the dynamical theory of incompressible viscous flows and the determination of criterion. *Phil. Trans. R. Soc.* **186**, 123–164.

Ricco, P. & Hahn, S. 2013 Turbulent drag reduction through rotating discs. *J. Fluid Mech.* **722**, 267.

Ricco, P., Ottonelli, C., Hasegawa, Y. & Quadrio, M. 2012 Changes in turbulent dissipation in a channel flow with oscillating walls. *J. Fluid Mech.* **700**, 77–104.

Ricco, P. & Quadrio, M. 2008 Wall-oscillation conditions for drag reduction in turbulent channel flow. *Int. J. Heat Fluid Flow* **29**, 601–612.

Richardson, L. 1921 Some measurements of atmospheric turbulence. *Phil. Trans. R. Soc.* **221** (582-593), 1–28.

Robert, J. 1992 Drag reduction: an industrial challenge. In *Skin friction drag reduction*, pp. 2.1–2.15. AGARD Report 786.

Robinson, S. K. 1991 Coherent motions in the turbulent boundary layer. *Annu. Rev. Fluid Mech.* **23**, 601–639.

Rogers, M. & Lance, G. 1960 The rotationally symmetric flow of a viscous fluid in the presence of an infinite rotating disk. *J. Fluid Mech.* **7** (4), 617.

Rosenblat, S. 1959 Torsional oscillations of a plane in a viscous fluid. *J. Fluid Mech.* **6** (2), 206.

Sasamori, M., Mamori, H., Iwamoto, K. & Murata, A. 2014 Experimental study on drag–reduction effect due to sinusoidal riblets in turbulent channel flow. *Experiments in Fluids* **55** (10), 1.

Schlichting, H. 1979 *Boundary-layer theory*. McGraw Hill.Inc.

Schrauf, G. 2006 Key aerodynamic technologies for aircraft performance improvement. In *5th Community Aeronautics Days*.

Skote, M. 2011 Turbulent boundary layer flow subject to streamwise oscillation of spanwise wall-velocity. *Phys. Fluids* **23**, 081703.

Skote, M. 2013 Comparison between spatial and temporal wall oscillations in turbulent boundary layer flows. *J. Fluid Mech.* **730**, 273.

Spinosa, E., Zhang, S. & Zhong, S. 2015 Control of near-wall structures in a turbulent boundary layer using synthetic jets. In *Proceedings European Drag Reduction & Flow Control Meeting, Cambridge, 23-26 March.*.

Stokes, G. 1851 *On the effect of the internal friction of fluids on the motion of pendulums*, , vol. 9. Pitt Press.

Szodruch, J. 1991 Viscous drag reduction on transport aircraft. *AIAA Paper* **91-0685**.

Trujillo, S., Bogard, D. & Ball, K. 1997 Turbulent boundary layer drag reduction using an oscillating wall. *AIAA Paper* **97-1870**.

Tsukahara, T., Seki, Y., Kawamura, H. & Tochio, D. 2005 Dns of turbulent channel flow at very low reynolds numbers. In *The 4th International Symposium on Turbulence and Shear Flow Phenomena*.

Viotti, C., Quadrio, M. & Luchini, P. 2009 Streamwise oscillation of spanwise velocity at the wall of a channel for turbulent drag reduction. *Phys. Fluids* **21** (115109).

Walsh, M. J. 1982 Turbulent boundary layer drag reduction using riblets. *AIAA Paper No.* **82-0169**.

Walsh, M. J. 1990 Riblets. In *Viscous Drag Reduction in Boundary Layers* (ed. D. M. Bushnell & J. N. Hefner), , vol. 123, pp. 203–261. Progress in Astronautics and Aeronautics.

Walsh, M. J. & Lindemann, A. M. 1984 Optimization and application of riblets for turbulent drag reduction. *AIAA Paper* **84-0347**.

Wang, C. 1989 Shear flow over a rotating plate. *App. Sc. Res.* **46**, 89.

Wilkinson, S. P. 1990 *Viscous Drag Reduction in Boundary Layers*, , vol. 1, chap. Interactive wall turbulence control, p. 479. AIAA.

Wise, D. J. & Ricco, P. 2014 Turbulent drag reduction through oscillating discs. *J. Fluid Mech.* **746**, 536.

Yoshino, T., Suzuki, Y. & Kasagi, N. 2008 Drag reduction of turbulence air channel flow with distributed micro-sensors and actuators. *J. Fluid Sci. Technol.* **3**, 137–148.

Zang, T. A. 1991 On the rotation and skew-symmetric forms for incompressible flow simulations. *Applied Numerical Mathematics* **7**, 27–40.

Zhang, S. & Zhong, S. 2010 Experimental investigation of flow separation control using an array of synthetic jets. *AIAA J.* **48** (3), 611–623.

Zhou, D. & Ball, K. 2008 Turbulent drag reduction by spanwise wall oscillations. *Int. J. Eng. Trans. A Basics* **21** (1), 85.